

Nonlinear Dynamics of Two-Dimensional Chaos Map and Fractal Set for Snow Crystal

Nguyen H. Tuan Anh¹, Dang Van Liet², and Shunji Kawamoto³

¹ Vietnam National University, University of Science, Ho Chi Minh City, Vietnam
(E-mail: tuananh@phys.hcmuns.edu.vn)

² Vietnam National University, University of Science, Ho Chi Minh City, Vietnam
(E-mail: dangvanliet@phys.hcmuns.edu.vn)

³ Osaka Prefecture University, Sakai, Osaka, Japan
(E-mail: kawamoto@eis.osakafu-u.ac.jp)

Abstract. In this paper, it is shown firstly that the one-dimensional (1-D) generalized logistic map obtained on the basis of a generalized logistic function for population growth has originally a discrete dynamical property. From the 1-D exact chaos solution, 2-D and 3-D chaos maps including the Mandelbrot map and the Julia map in terms of real variables are derived, and 2-D maps related to the Henon map, the Lorenz map and the Helleman map are obtained. Finally, a 2-D chaos map and the fractal set constructed from a 1-D exact chaos solution are considered for the physical analogue of snow crystal, and nonlinear dynamics on the fractal set are discussed by iterating numerically the 2-D map.

Keywords: Chaos map, Fractal set, Logistic map, Mandelbrot map, Julia map, Henon map, Lorenz map, Helleman map, Snow crystal, Nonlinear dynamics.

1 Introduction

For the study of nonlinear phenomena, it is known that simplest nonlinear difference equations have arisen in the field of biological, economic and social sciences, and possess a rich spectrum of dynamical behavior as chaos in many respects [1-3]. A population growth is modeled as a special example, and has been afforded by the nonlinear difference equation called the logistic map. Particularly, for one-dimensional (1-D) chaos maps, a bifurcation diagram of the two parameter quadratic family has been observed [4], and the self-adjusting logistic map with a slowly changing parameter in time have been considered [5]. Moreover, the logistic map with a periodically modulated parameter has been presented [6]. In the meantime, various chaotic sequences have been proposed for the generation of pseudo-random numbers, and for the application to cryptosystems [7-9].

At the same time, a family of shapes and many other irregular patterns in nature called fractals has been discussed for the geometric representation, as an irregular set consisting of parts similar to the whole [10-12]. However, since the Mandelbrot map is defined as a complex map, it has been pointed out that the

8th CHAOS Conference Proceedings, 26-29 May 2015, Henri Poincaré Institute, Paris France

© 2015 ISAST



physics of fractals is a research subject to be born [13]. In addition, chaotic and fractal dynamics have been expanded to experimental observations with the mathematical models [14], and fractal compression has been presented to compress images using fractals [15]. Recently, a construction method of 3-D chaos maps has been proposed, and the fractal sets with physical analogue have been shown numerically [16].

In this paper, we derive a generalized logistic map from a generalized logistic function for population growth, and discuss the dynamical behavior of the map in Section 2. Then, by introducing the 1-D exact chaos solution, we construct 2-D and 3-D chaos maps including the Mandelbrot map and the Julia map in terms of real variables, and 2-D maps related to the Henon map, the Lorenz map and the Helleman map are obtained in Section 3. Finally, a 2-D chaos map and the fractal set are considered for the physical analogue of snow crystal, and nonlinear dynamics on the fractal set are discussed by iterating the 2-D map in Section 4. The last Section is devoted to conclusions.

2 A Generalized Logistic Map

Firstly, we introduce a generalized logistic function $P(t)$ as

$$P(t) = \frac{a}{b + e^{-ct}} + d, \quad (1)$$

with the time $t > 0$, real constants $\{ a \neq 0, b > 0, c \neq 0, d \geq 0 \}$, and a constant population growth term d . By differentiating (1), we have the first order differential equation;

$$\frac{dP}{dt} = \left(\frac{bc}{a}\right)P \left[\left(\frac{a+2bd}{b}\right) - P \right] - \left(\frac{cd}{a}\right)(a+bd), \quad (2)$$

and by a variable transformation;

$$X(t) \equiv P(t) / \frac{(a+2bd)}{b}, \quad (3)$$

and the difference method;

$$\frac{dX}{dt} \approx \frac{X_{n+1} - X_n}{\Delta t}, \quad n = 0, 1, 2, \dots, \quad (4)$$

with $X_n \equiv X(t)$ and the time step $\Delta t > 0$, we find

$$\frac{X_{n+1} - X_n}{\Delta t} \equiv \left(\frac{bc}{d}\right)\left(\frac{a+2bd}{b}\right)X_n(1-X_n) - \left(\frac{bcd}{a}\right)\left(\frac{a+bd}{a+2bd}\right). \quad (5)$$

Then, by the variable transformation;

$$x_n \equiv (B_0 / A)X_n, \quad (6)$$

with $A \equiv 1 + \Delta t(c/a)(a+2bd)$ and $B_0 \equiv \Delta t(c/a)(a+2bd)$, we arrive at a 1-D

generalized logistic map [16];

$$x_{n+1} = Ax_n(1-x_n) + B, \quad (7)$$

here

$$A \equiv 1 + \frac{c(a+2bd)}{a}(\Delta t), \quad (8)$$

$$B \equiv \frac{-bc^2d(a+bd)(\Delta t)^2}{a[a+c(a+2bd)(\Delta t)]}, \quad (9)$$

which gives a discrete nonlinear system. If $d = 0$ in (8) and (9), then (7) yields the logistic map $x_{n+1} = Ax_n(1-x_n)$, and the map at $A = 4.0$ has an exact chaos solution $x_n = \sin^2(C2^n)$ with a real constant $C \neq \pm m\pi/2^l$ and finite positive integers $\{l, m\}$. We call the map $x_{n+1} = 4x_n(1-x_n)$ the kernel chaos map of (7). Therefore, the constant A in (7) denotes a coefficient of the nonlinear term, and B corresponds to the constant population growth term d of (1).

It is interesting to note that the logistic function has been introduced for the population growth of city in a discussion of the discrete numerical data [17], and has found an application to the field of such as biology, ecology, biomathematics, economics, probability and statistics. Therefore, the function (1) has originally a discrete property for population growth, that is, a discrete nonlinear dynamics.

3 2-D and 3-D Chaos Maps

We have the following three cases to find 2-D and 3-D chaos maps from a 1-D exact chaos solution:

Case 1

From an exact chaos solution;

$$x_n = \sin^2(C2^n) \quad (10)$$

with $C \neq \pm m\pi/2^l$ and finite positive integers $\{l, m\}$ to the logistic map $x_{n+1} = 4x_n(1-x_n)$, we have, by introducing a real parameter $\alpha \neq 0$, as

$$\begin{aligned} x_{n+1} &= 4\cos^2(C2^n)\sin^2(C2^n) \\ &= 4(1-\alpha)\cos^2(C2^n)\sin^2(C2^n) + 4\alpha\cos^2(C2^n)\sin^2(C2^n) \\ &= 4(1-\alpha)x_n(1-x_n) + 4\alpha(x_n - \sin^4(C2^n)) \\ &\equiv 4x_n - 4(1-\alpha)x_n^2 - 4\alpha y_n \end{aligned} \quad (11)$$

with

$$y_n \equiv \sin^4(C2^n). \quad (12)$$

Therefore, we get a 2-D kernel chaos map from (10)-(12);

$$x_{n+1} = 4x_n - 4(1 - \alpha)x_n^2 - 4\alpha y_n, \quad (13)$$

$$y_{n+1} = 16(1 - x_n)^2 y_n, \quad (14)$$

and a generalized 2-D chaos map, according to the construction method [16], as

$$x_{n+1} = a_1(x_n - (1 - \alpha)x_n^2 - \alpha y_n) + b_1, \quad (15)$$

$$y_{n+1} = a_2(1 - x_n)^2 y_n + b_2, \quad (16)$$

with real coefficients and constants $\{a_1, a_2, b_1, b_2\}$. Here, the first equation (15) has the same form as the Helleman map;

$$x_{n+1} = 2ax_n + 2x_n^2 - y_n, \quad (17)$$

$$y_{n+1} = x_n, \quad (18)$$

with a real coefficient a , which has been obtained from the motion of a proton in a storage ring with periodic impulses [18].

Moreover, from the exact chaos solution (10), we find the following 3-D map;

$$\begin{aligned} x_{n+1} &= (2\cos(C2^n)\sin(C2^n))^2 \\ &\equiv (2y_n z_n)^2, \end{aligned} \quad (19)$$

with

$$y_n \equiv \cos(C2^n), \quad (20)$$

$$z_n \equiv \sin(C2^n), \quad (21)$$

and have a 3-D kernel chaos map from (19)-(21) as

$$x_{n+1} = 4x_n y_n^2, \quad (22)$$

$$y_{n+1} = y_n^2 - x_n, \quad (23)$$

$$z_{n+1} = 2y_n z_n. \quad (24)$$

Therefore, we get a generalized 3-D chaos map;

$$x_{n+1} = a_1 x_n y_n^2 + b_1, \quad (25)$$

$$y_{n+1} = a_2 (y_n^2 - x_n) + b_2, \quad (26)$$

$$z_{n+1} = a_3 y_n z_n + b_3, \quad (27)$$

which has been discussed in [16], where $\{a_1, a_2, a_3, b_1, b_2, b_3\}$ are real coefficients and constants.

Case 2

For an exact chaos solution;

$$x_n = \cos(C 2^n), \quad (28)$$

we have the following derivation by introducing a real parameter $\alpha \neq 0$ as

$$\begin{aligned} x_{n+1} &= \cos^2(C 2^n) - \sin^2(C 2^n) \\ &= \cos^2(C 2^n) - (1 - \alpha) \sin^2(C 2^n) - \alpha \sin^2(C 2^n) \\ &\equiv -\alpha + (1 + \alpha) \cos^2(C 2^n) - (1 - \alpha) y_n, \end{aligned} \quad (29)$$

with

$$y_n \equiv \sin^2(C 2^n). \quad (30)$$

Then, from (28)-(30), we obtain the kernel chaos map as

$$x_{n+1} = -\alpha + (1 + \alpha) x_n^2 - (1 - \alpha) y_n, \quad (31)$$

$$y_{n+1} = 4 x_n^2 y_n, \quad (32)$$

and a generalized 2-D chaos map;

$$x_{n+1} = a_1 (-\alpha + (1 + \alpha) x_n^2 - (1 - \alpha) y_n) + b_1, \quad (33)$$

$$y_{n+1} = a_2 x_n^2 y_n + b_2, \quad (34)$$

with real coefficients and constants $\{a_1, a_2, b_1, b_2\}$, where the first equation (33) has the same form as the Henon map [19];

$$x_{n+1} = 1 - a x_n^2 + y_n, \quad (35)$$

$$y_{n+1} = b x_n, \quad (36)$$

with real coefficients $\{a, b\}$, which has been introduced as a simplified model of the Poincare section of the Lorenz model, and is known as one of the most studied maps for dynamical systems.

Here, it is interesting to note that if we define $y_n \equiv \sin(C 2^n)$ with $\alpha = 0$ in (29), we find a generalized 2-D chaos map;

$$x_{n+1} = a_1 (x_n^2 - y_n^2) + b_1, \quad (37)$$

$$y_{n+1} = a_2 x_n y_n + b_2, \quad (38)$$

where the case of $(a_1, a_2, b_1, b_2) = (1.0, 2.0, x_0, y_0)$ or $(1.0, 2.0, k_1, k_2)$ with initial values $\{x_0, y_0\}$ and real parameters $\{k_1, k_2\}$ corresponds to the Mandelbrot map or the Julia map in terms of real variables, respectively [16].

Case 3

Similarly, for another exact chaos solution;

$$x_n = \sin(C 2^n), \quad (39)$$

we have the following derivation;

$$\begin{aligned} x_{n+1} &= 2 \cos(C 2^n) \sin(C 2^n), \\ x_{n+2} &= 2(\cos^2(C 2^n) - \sin^2(C 2^n))x_{n+1} \\ &= 2x_{n+1}(1 - 2x_n^2), \end{aligned} \quad (40)$$

$$x_{n+1} \equiv 2x_n(1 - 2y_n), \quad (41)$$

with

$$y_n \equiv x_{n-1}^2. \quad (42)$$

Then, we find a 2-D kernel chaos map from (41) and (42) as

$$x_{n+1} = 2x_n(1 - 2y_n), \quad (43)$$

$$y_{n+1} = x_n^2, \quad (44)$$

and a generalized 2-D chaos map;

$$x_{n+1} = a_1(x_n - 2x_n y_n) + b_1, \quad (45)$$

$$y_{n+1} = a_2 x_n^2 + b_2, \quad (46)$$

with real coefficients and constants $\{a_1, a_2, b_1, b_2\}$. It is interesting to note that the first equation (45) has the same form as the 2-D Lorenz map [20, 21];

$$x_{n+1} = (1 + ab)x_n - bx_n y_n, \quad (47)$$

$$y_{n+1} = bx_n^2 + (1 - b)y_n, \quad (48)$$

with real coefficients $\{a, b\}$, which is known to have chaotic dynamics.

Thus, it is found that the 2-D chaos maps derived from 1-D exact chaos solutions (10), (28) and (39) include the Mandelbrot map and the Julia map, and are related to the Helleman map, the Henon map and the 2-D Lorenz map, which give chaotic behaviors and nonlinear dynamics.

4 Nonlinear Dynamics for Snow Crystal

According to the approach presented in Section 3, we introduce a 1-D exact chaos solution;

$$x_n = \cos(C6^n), \quad (49)$$

to the kernel chaos map;

$$x_{n+1} \equiv f(x_n, y_n), \quad (50)$$

with

$$y_n \equiv \sin(C6^n), \quad (51)$$

$$x_n^2 + y_n^2 = 1, \quad (52)$$

and find a generalized 2-D chaos map as

$$x_{n+1} = a_1(x_n^6 - 15x_n^4y_n^2 + 15x_n^2y_n^4 - y_n^6) + k_1, \quad (53)$$

$$y_{n+1} = a_2(6x_n^5y_n - 20x_n^3y_n^3 + 6x_ny_n^5) + k_2, \quad (54)$$

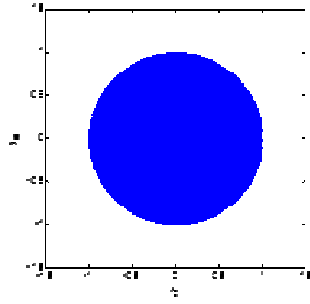
with real coefficients and constants $\{a_1, a_2, k_1, k_2\}$.

Then, the fractal set is defined by

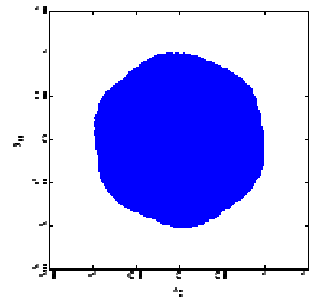
$$M = \{x_0, y_0 \in \mathbf{R} \mid \lim_{n \rightarrow \infty} x_n, y_n < \infty\}, \quad (55)$$

where $\{x_0, y_0\}$ are initial values, and the fractal sets are illustrated in Figure 1, which depend on the constant parameters $\{k_1, k_2\}$. The fractal set (a) of Figure 1 gives a circle under the condition (52), and (b)-(e) show how the fractal set (a) grows as a physical analogue toward a natural snow crystal (f), which is a six-cornered dendrite-type depending on the temperature and the saturation in environment [22, 23]. Here, for calculating the fractal set M , we introduce an iteration number $n=300$ to obtain each element of M under the convergence condition $x_n^2 + y_n^2 < 4.0$ for the map (53) and (54), and the numerical calculation software MATLAB.

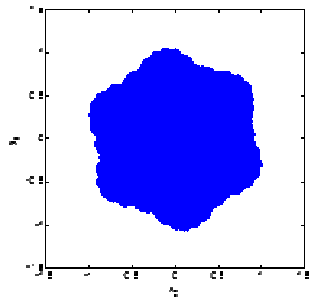
Each fractal set illustrated in Figure 1 is a set of initial value point (x_0, y_0) defined by (55) under the condition $x_n^2 + y_n^2 < 4.0$. For nonlinear dynamics of the 2-D chaos map (53) and (54), orbits of (x_n, y_n) governed by the map are calculated and shown on the fractal set of initial values in Figure 2, where (a); $n=0, 1$ illustrates orbits from each initial point (x_0, y_0) to the (x_1, y_1) , (b); $n=0, 1, 2, 3$ from (x_0, y_0) to (x_3, y_3) , and (c); $n=0, 1, \dots, 5$ from (x_0, y_0) to (x_5, y_5) , for all the initial points. It is found that the orbits are complex, and seem like colliding of water molecules. Here, the orbits show that we have (x_1, y_1) as the case of $n=0$ from (53); $x_1=f(x_0, y_0)+k_1$ and (54); $y_1=g(x_0, y_0)+k_2$, (x_2, y_2) from



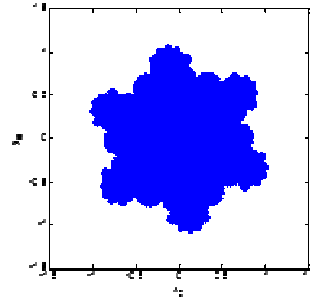
(a) $(a_1, a_2, k_1, k_2) = (1.0, 1.0, 0.0, 0.0)$



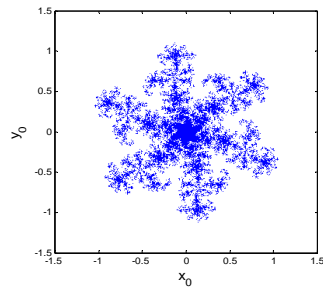
(b) $(a_1, a_2, k_1, k_2) = (1.0, 1.0, 0.1, 0.1)$



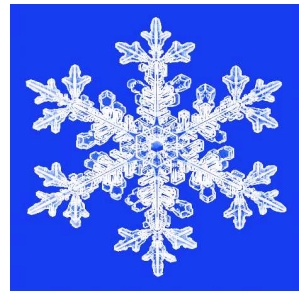
(c) $(a_1, a_2, k_1, k_2) = (1.0, 1.0, 0.3, 0.3)$



(d) $(a_1, a_2, k_1, k_2) = (1.0, 1.0, 0.5, 0.5)$

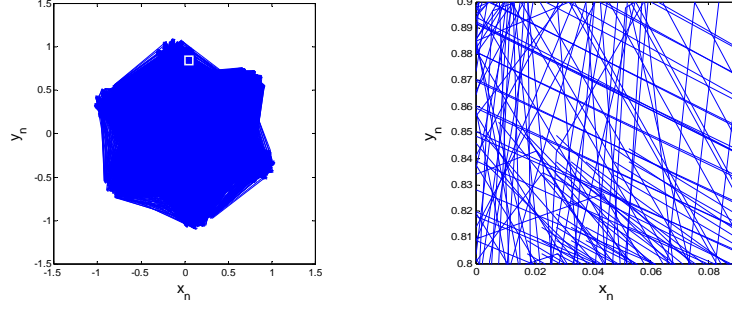


(e) $(a_1, a_2, k_1, k_2) = (1.0, 1.0, 0.58158, 0.58158)$

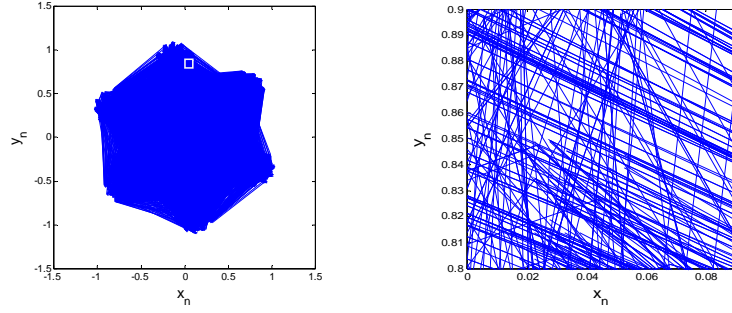


(f) natural snow crystal [23]

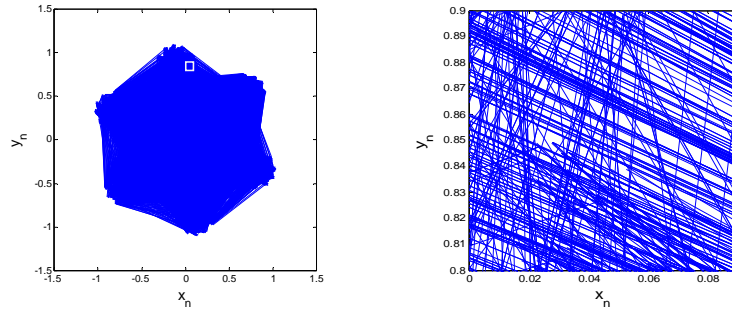
Fig. 1. Fractal sets of the map (53) and (54) for snow crystal.



(a) Orbits for $n=0, 1$ and of a small framed region.



(b) Orbits for $n=0, 1, 2, 3$ and of a small framed region.



(c) Orbits for $n=0, 1, 2, 3, 4, 5$ and of a small framed region.

Fig. 2. Orbits of (x_n, y_n) with $n=0, 1, 2, 3, 4, 5$ given by the map (53) and (54) on the fractal set (Figure 1 (e)).

$x_2=f(x_1, y_1)+k_1$ and $y_1=g(x_0, y_0)+k_2, \dots$, and (x_{300}, y_{300}) from $x_{300}=f(x_{299}, y_{299})+k_1$ and $y_{300}=g(x_{299}, y_{299})+k_2$, under the condition $x_n^2 + y_n^2 < 4.0$. Then, we get one element of the fractal set, and find that $\{(x_1, y_1), (x_2, y_2), \dots, (x_{300}, y_{300})\}$ are other initial value points satisfying the condition $x_n^2 + y_n^2 < 4.0$ for the fractal set.

Thus, if the orbits shown in Figure 2 correspond to the dynamics of water molecules colliding with other ones in natural snow crystal, the map (53) and (54) may present the discrete nonlinear dynamics.

Conclusions

We have derived firstly the 1-D generalized logistic map, and have discussed that the map has originally a discrete numerical property for population growth of city. Then, from the 1-D chaos solution, 2-D maps related to the Henon map, the 2-D Lorenz map and the Helleman map, which have chaotic dynamics, have been derived. Furthermore, the 2-D chaos map (53) and (54) gives the fractal set for snow crystal, and orbits of the map on the fractal set have been numerically calculated. As a result, it is found that the 2-D chaos maps derived from 1-D exact chaos solutions have discrete nonlinear dynamics, and may express physical analogues with chaotic property as physics.

The authors would like to thank Prof. C. V. Tao for his encouragement, and Mr. N. A. Hao for his numerical calculation at University of Science, Ho Chi Minh City.

References

1. R. M. May. Biological populations with non-overlapping generations: Stable points, stable cycles, and chaos. *Science* 15: 645-646, 1974.
2. T. Y. Li and J. A. Yorke. Period three implies chaos. *American Mathematics Monthly* 82: 985-992, 1975.
3. R. M. May. Simple mathematical models with very complicated dynamics. *Nature* 261: 459-467, 1976.
4. E. Barreto, B. R. Hunt, C. Grebogi and J. A. Yorke. From high dimensional chaos to stable periodic orbits: The structure of parameter space. *Phys. Rev. Lett.* 78 : 4561-4564, 1997.
5. P. Melby, J. Kaidel, N. Weber and A. Hubler. Adaptation to the edge of chaos in the self-adjusting logistic map. *Phys. Rev. Lett.* 84: 5991-5993, 2000.
6. T. U. Singh, A. Nandi and R. Ramaswamy. Coexisting attractors in periodically modulated logistic maps. *Phys. Rev. E* 77: 066217, 2008.
7. L. M. Pecora and T. L. Carroll. Synchronization in chaos systems. *Phys. Rev. Lett.* 64: 821-824, 1990.
8. G. Perez and H. A. Cerdeira. Extracting message masked by chaos. *Phys. Rev. Lett.* 74: 1970-1973, 1995.
9. G. D. V. Wiggeren and R. Roy. Optical communication with chaotic waveforms. *Phys. Rev. Lett.* 81: 3547-3550, 1998.
10. B. B. Mandelbrot. *The Fractal Geometry of Nature*. Freeman, San Francisco, 1982.

11. H. Peitgen and P. Richter. *The Beauty of Fractals*. Springer, New York, 1986.
12. H. Peitgen, H. Jurgens and D. Saupe. *Chaos and Fractals – New Frontiers of Science*. Springer, New York, 1992.
13. L. P. Kadanoff. Where's the physics? *Phys. Today* 39: 6-7, 1986.
14. F. C. Moon. *Chaotic and Fractal Dynamics*. Wiley, New York, 1992.
15. M. F. Barnsley. *Fractals Everywhere*. Academic Press, New York, 1993.
16. N. T. Nhien, D. V. Liet and S. Kawamoto. Three-dimensional chaos maps and fractal sets with physical analogue. *Proc. of CHAOS2014*: 337-347, Lisbon, Portugal, 2014.
17. P. F. Verhulst. Mathematical researches into the law of population growth increase. *Nouveaux Memoires de l'Academie Royale des Sciences et Belles-Lettres de Bruxelles* 18: 1-42, 1845.
18. R. H. G. Helleman. Self-generated chaotic behavior in nonlinear mechanics. *Fundamental Problems in Statistical Mechanics* 5: 165-233, North-Holland, Amsterdam, 1980.
19. M. Henon. A two-dimensional mapping with a strange attractor. *Communications in Mathematical Physics* 50: 69-77, 1976.
20. H. P. Fang and B. L. Hao. Symbolic dynamics of the Lorenz equations. *Chaos, Solitons and Fractals* 7: 217-246, 1996.
21. D. N. Deleanu. On the selective synchronization of some dynamical systems that exhibit chaos. *Proc. of CHAOS2014*: 81-90, Lisbon, Portugal, 2014.
22. C. A. Reiter. A local cellular model for snow crystal growth. *Chaos, Solitons and Fractals* 23: 1111-1119, 2005.
23. <http://www.snowcrystals.net/gallery1sm/index.htm>

Sudden cardiac death and Turbulence

Guillaume Attuel¹, Oriol Pont¹, Binbin Xu¹, and Hussein Yahia¹

GeoStat, “Geometry and Statistics in acquisition data”, Centre de recherche INRIA
Bordeaux Sud-Ouest, 200 rue de la Vieille Tour, 33405 Talence Cedex, France
(E-mail: guillaume.attuel@inria.fr)

Abstract. Data acquired from the electrical activity of human hearts during episodes of atrial fibrillation, a disordered arrhythmia that is a major cause of stroke, reveals intriguing features for an excitable media: highly skew symmetric probability distributions with heavy tails, long range correlations, and broad singularity spectra. Interestingly, the relevant exponents extracted from these empirical laws are stable over several minutes but not universal. Their stable values are distributed among patients and areas of the heart. The question of central clinical purpose is whether they might characterise locally the myocardium contingent pathology. To achieve clarification of these peculiar facts, we were led to devise a phenomenological model that departs from the conventional approach to fibrillation. Instead of a defect mediated spiral wave “turbulence” induced by front collisions, fibrillation is pictured here as a highly intermittent modulation of cardiac pulse trains. It is based on the physiology of inter-cellular ionic exchanges, which is associated with the natural degree of freedom of the inter-pulse duration. We infer an experimentally unknown slow dynamics of inter-cellular coupling, that may induce an inter-pulse effective coupling. This interaction creates a modulation that may lead to intermittency in various ways. The exchange of charges occurs at small scales in the model. They are passively advected at each interstitial junction on fast time scales and on average collectively driving the larger scales. In fact, a dimensionless number characterising the dynamics is an analogue of the Rayleigh number. Away from a rapidly beating source, random back scattering and front splitting make pulses follow random hierarchical “percolating” paths in 1D. We discuss very briefly the topological origin of these dynamics. In the light of this model, we don’t omit to mention some important physiological aspects of the pathology that are still not well understood and more possibilities for the case which comes to grip with sudden cardiac death.

Keywords: Heart dynamics, Reaction-Diffusion, Driven systems, Self organized criticality, Multiplicative noise, Random paths, Topological excitations, Singularities.

1 Introduction

Sudden cardiac death accounts for about 10% of all natural deaths in developed countries and for about 50% of the mortality from cardiovascular diseases. Meanwhile, it is not really a pathology: statistical surveys have found risk factors but which fail to be individually predictive [1]. In our present understanding, it can be considered more as an accident. One cause of sudden cardiac

8th CHAOS Conference Proceedings, 26-29 May 2015, Henri Poincaré Institute, Paris France

© 2015 ISAST



death is fibrillation of the ventricles. Experimental studies are difficult for obvious reasons. The milder case of atrial fibrillation (AF), which is however one major cause of stroke in Europe and North America, can be monitored and studied more easily. In this paper, we give the general scheme of an analysis of AF that we are developing. We will shortly discuss at the end some possible lessons we may learn from it for sudden cardiac death.

The heart muscle is an excitable tissue, long believed to be a syncytium of myocardial cells. Models of excitability for the heart are reaction-diffusion systems that describe the propagation of electrical pulses, called action potentials. They result from ionic exchange cycles between the cytoplasm of excitable cells and their extra-cellular medium. A typical example is an action potential propagating through a nerve axon [2] or throughout the myocardium [3] [4] [5] [6]. In the right atrium of a human heart, the sinus node (a pacemaker) ensures a periodic stimulation of the tissue, from where pulses propagate regularly in normal sinus rhythm. In its abnormal states, called arrhythmias, the myocardium is overwhelmed by rapid and irregular patterns of activation. In part for the reasons we are exposing in the text, we consider AF the most irregular arrhythmia, as illustrated in fig.(1).

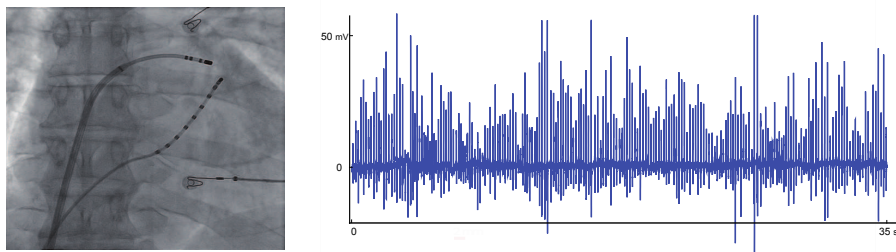


Fig. 1. 35 sec of paroxysmal AF at a sampling rate of $1kHz$ are shown recorded from a bipolar electrode, with some peaks reaching saturation level of the recording device. Electrodes are about 2 mm apart. A radiography of the left atrium is shown, where the bipolar electrode is located near the superior left pulmonary vein, held by a medical practitioner, whereas the other catheter comprising 10 electrodes runs along the coronary sinus.

Chaos has been observed in cultures of automatic cardiac cells, through their coupling to periodic stimulation, and also in the heart via the occurrence of parasytoses. This can be traced to phase locking and chaos of relaxation oscillators with periodic forcing, and could be well modelled by return maps [7] [8] [9]. Also, period doubling, called alternans in this context, arises when the adaptation of the action potential duration to an imposed rate becomes unstable [10]. For this reason, alternans are thought in one hypothesis as a route to ventricular fibrillation [11]. Moreover, fibrillation in the atria were in some instances clinically found to follow an inadaptation of the action potential duration [12]. However, an excitable limit cycle is very robust when it comes down to chaos, because its saddle fixed point does not give way to a homoclinic

tangle. This can be understood by considering the stable fixed point as an absorbing state, or a phase resetting state. Therefore, even under periodic forcing, no return map can be drawn. In other words, the regularity of the triggering sources is transferred to the limit cycle.

In contrast, as propagation becomes further involved in the arrhythmia, the usual theoretical interpretation is based on a kind of defect mediated turbulence, specific to excitable oscillators. Basically, spiral waves are often found more stable than striped or other patterns in excitable media. This stems from the important fact that an excitable pulse with a free end meets a region in a refractory state and starts wandering about it [13] [14] [15]. It is also more fundamentally related to the topological charge of the spiral core [16] and to the chiral symmetry breaking that an excitable pulse carries with itself (a Bloch wall) [17] [18] [19]. Low dimensional aperiodicity has again been observed before the onset of fibrillation for meandering spiral cores [20]. To account for spatio-temporal chaos a mechanism of front collisions is put forward. If in oscillatory media spirals may break up due to a modulational instability of the emitted pulse train from its meandering core, in excitable media the breakup seems to amount to direct fore front and back front collisions within the pulse train [21] [22] [23]. Notice that when a small diffusivity of the inhibitor is added, a curvature instability may lead to front splitting and spiral turbulence near the Ising-Bloch transition [24].

As successful as low dimensional chaos, and spatio-temporal chaos, in excitable media may look in describing these arrhythmias, we show here why this paradigm is quite inadequate to tackle an essential property of the recorded data, which hasn't been noticed so far.

A crucial aspect about the pathology is the intermittency of bursty occurrences of the arrhythmia. Intermittent alternation of sinus rhythm with fibrillation is what defines paroxysmal AF. This intermittency can be modulated by the external drive of the autonomic nervous system, as shown by P. Coumel and co-workers, see for instance [25]. Moreover, on the myocardium surface, within each episode of fibrillation, the recorded signal is found to be more or less regular: the so called "fragmentation" in clinical lingo. In fact, as we demonstrate in section 2, the locally recorded electrical potential exhibits many traits in common with hydrodynamic intermittency. Another poorly understood fact is a reversible process of deterioration of the myocardium during AF called remodelling [26]. It appears that the longer the heart remains in a fibrillatory state, the poorer its conduction properties become, and the more stable this abnormal state gets. We believe that these features are rooted in some underlying chemical modulation of the electrical synapses between the cells. Our model demonstrates this possibility.

We may look for the nucleation of metastable chaotic domains to explain such observations. This has led us to find out a physiological path to the mechanism described by Y. Pomeau [27]. As illustrated in [28], if a limit cycle is able to reach its homoclinic connection, then bistability with another fixed point, or cycle, may generate spatio-temporal intermittency. The difficulty is that an excitable limit cycle is over-damped and very robust. No such saddle fixed point connecting with another basin of attraction normally exists. Even worse would

be to try to find a crisis bifurcation to some strange attractor. Never mind, if the tissue is in fact capable of generating another limit cycle, then the route devised by Y. Pomeau might be reached. For instance a modulation of pulse trains would work. This can be indeed the case as we show. This originates in the electrical coupling between the cells, that under some circumstances which we describe, may grow collectively, versus diffusively. One can thus rephrase the previous findings for oscillatory media in terms of these collective modes, and find a variety of interesting scenarios. For simplicity, we adopt a point of view *à la* Ginzburg Landau.

We formulate therefore in section 3 a derivation from first principles of the yet unknown dynamics of ionic currents at the gap junctions. This dynamical coupling between cells is considered as a synaptic plasticity. The point is to question the importance of intrinsic fluctuations and disorder. We make sure that observing the Ginzburg region of criticality in excitable reaction-diffusion systems is classically impossible. Then, we will find out that cardiac pulses can be pinned where cycles of neighbouring cells become out of phase with one another, because of interstitial plasticity. This unfortunate plasticity may slowly contaminate the whole tissue, which is what we will relate to electrical remodelling.

In section 4, we very briefly sketch an interpretation. Due to the intrinsic noise, the critical Ginzburg domain extends widely, leading to self organised criticality (SOC). This maps to multiplicative noise, describing the singularities in the signal.

We will show throughout the text the high level of agreement between the patients data and the model data.

2 Time series, fluctuations and limitations of excitable models

Surface electrical potentials recorded as time series during AF are called electrograms (egm), such as the one shown in fig.(1). Normal frequency f , in beats per minute, is about $f \approx 60 \text{ bpm}$, whereas during AF, it is typically in the range of $200 \text{ bpm} \lesssim f \lesssim 600 \text{ bpm}$. At first sight, egms during AF contrast to normal as they seem to fluctuate randomly. Their amplitude also looks locally abnormally oscillatory, fig.(2). The auto-correlation function starts decreasing rapidly, exponentially fast during the first 60 ms or so, and goes on oscillating with a slow decrease of the envelop, asymptotically as a power law, see fig.(2), where an indicative solid line $\sim t^{-1}$ is drawn. Peaks appear naturally as multiples of the average periodicity of the arrhythmia at about 300 bpm there. The identification of the shorter time scale is expected and indicative of local incoherent oscillations, but the algebraic correlation law of the envelop is more suggestive of some collective phenomena with quasi long-range order. Thus, we are led to look for some collective modulation of the pulses.

We observe that fluctuations are large and their probability density distributions collapse as is seen in fig.(3). The high skewness and heavy tails are a

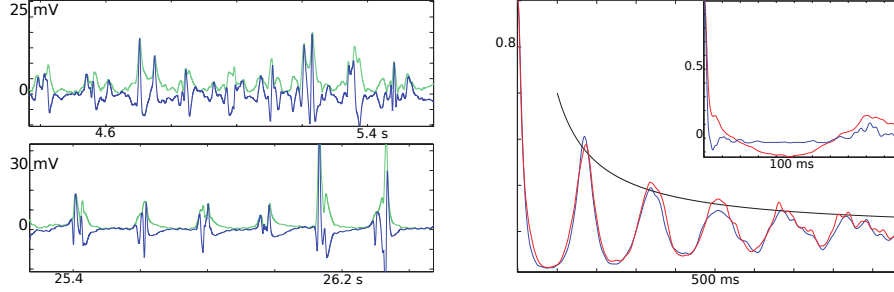


Fig. 2. Left: Two instances of one egm amplitude and its envelop at two different moments in time, where a Hilbert transform was used. Right: Two auto-correlation functions of egm envelopes, and of amplitudes in the inset, for two different locations on the heart.

hint of underlying mechanisms. They can be cast into the form

$$P(A, A_c) = A^{-\tau} G\left(\frac{A}{A_c}\right) \quad (1)$$

where A is the egm varying amplitude in mV , A_c is a cut-off, τ is a scaling exponent, and a scaling function G decreasing rapidly towards zero. Very briefly summarized, various values of τ have been found. They range roughly between $1.2 < \tau < 3$ among patients, and regions of the atria. To our knowledge, simi-

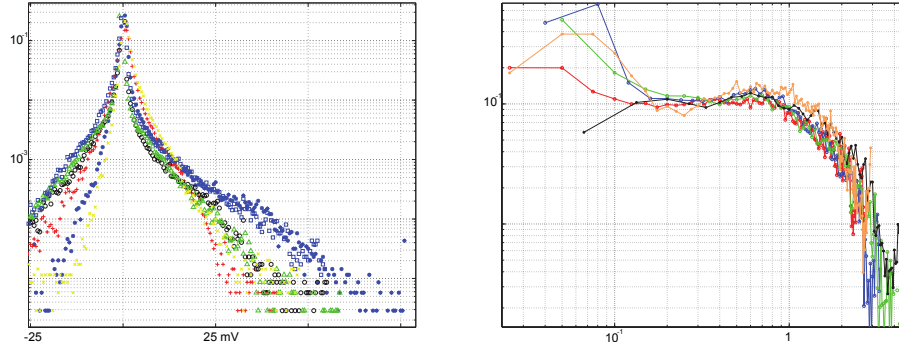


Fig. 3. Normalised probability density distributions of egm amplitudes in semilog scale, from all over the atrium of one patient (left). Shown in loglog scale is the empirical collapse, for positive values and various exponents τ , on a scaling function G of eq.(1) (right). $A_c \approx 30 - 50 mV$.

lar fluctuations were not found in excitable systems, but are rather ubiquitous in complex systems. To name a few instances, they are found in random field Ising models [29], with the Barkhausen noise as a magnetic field is applied to a dirty ferromagnet [30], for magnetic penetration in hard superconductors [31]

[32] [33], during the firing activity of some neural networks [34][35][36][37], or in the intermittent regimes of strong turbulence [38] [39].

Turning to continuous excitable media, they are modelled by reaction-diffusion systems

$$\begin{cases} \frac{\partial}{\partial t} U_m = \mathcal{R}(U_m, J_m) + D \Delta(U_m) \\ \frac{\partial}{\partial t} J_m = \mathcal{G}(U_m, J_m) \end{cases}. \quad (2)$$

Here, U_m is associated with the membrane potential of a cell, and J_m is a vector representing (non diffusing) inhibitors, associated with the many ionic currents going through channels across the otherwise impermeable membrane of a cardiac cell. In the limit of interest, time scales are well separated, that is U_m is a fast variable, while J_m is a slow variable. One usually denotes by $\mu^{-1} \approx 1 \text{ ms}$, the typical fast time scale, which corresponds to the time for the insulating membrane, of thickness $\Lambda \approx 100 \text{ nm}$, to depolarise. This is possible at such short time scales because Nernst-Planck thermal equilibrium is reached indeed thanks to facilitated diffusion and active pumping of ions [40]. The slow time scale, associated with repolarisation, is typically of the order of 100 ms or greater.

Now, to be endowed with the property of excitability, the system's null clines, $\mathcal{R} = 0$ and $\mathcal{G} = 0$, basically intersect in a way as to produce locally a kind of saddle-node configuration. Nonlinearities and dissipation (or periodic order parameters) give rise to a limit cycle once an orbit is generated away from the saddle fixed point. It is insightful to draw a straightforward analogy with a Van der Waals diagram. Roughly speaking, the analogy goes as: a cycle “nucleates” each time the “supercooled spinodal branch” is reached by a finite perturbation. The width of the nucleation region corresponds to the degree of excitability. A Ginzburg-Landau description of eq.(2) reads as $\frac{\partial}{\partial t} U_m = -\frac{\delta}{\delta U_m} \mathcal{F}_0$, with a free energy of the form

$$\mathcal{F}_0 = \frac{1}{2} \int dx^d \left\{ -\mu U_m^2 + \frac{\beta}{2} U_m^4 + D (\nabla U_m)^2 - I U_m \right\} \quad (3)$$

where all parameters are positive, $I = J_0 - J_m$ is a source term, and J_0 is an external input of current. Dimension $d = 2$ is appropriate for the atria, since the atrial myocardium is very thin, typically of order 2 mm thick, as it does not contribute much to the pump function of the heart, while $d = 3$ is more adequate for the ventricles. In fact dimension $d = 1$ is quite appropriate also for the description of fast conducting fibres in both chambers.

Since the free energy has two local minima, depending on boundary conditions, domain walls typically form. In source free conditions, their height is $U_0 = 2\sqrt{\frac{\mu}{\beta}} \approx 100 \text{ mV}$ and their thickness is the Ginzburg-Landau correlation length $l_c \propto \sqrt{\frac{D}{\mu}} \approx 1 \text{ mm}$. They propagate at constant velocity by diffusion, with a velocity $c \propto \sqrt{D\mu} \approx 1 \text{ ms}^{-1}$. The role of the recovery current J_m is to break the symmetry between the two minima of the energy manifold, by favouring the return to one of them, corresponding to the rest potential. In its most basic version, we have the Fitzhugh-Nagumo model (FhN), with

$\mathcal{G}(U_m, J_m) = \gamma U_m - \sigma J_m - \eta$, where σ controls the repolarisation time scale, and η is a leaking current. It defines a cell cycle.

For the sake of simplicity here, let us take $\eta = 0$, the condition of excitability becomes $\mu > \frac{\gamma}{\sigma}$. Let us admit that FhN may spontaneously evolve into locally aperiodic states, for instance with more complicated reactions \mathcal{G} and the spiral breakup mechanism [41]. Then, configuration averaging leads to an effective reparametrization $\mu \rightarrow \mu - \frac{\gamma}{\sigma}$, since one expects fast modes to be slaved to slow modes and average as $\langle J_m \rangle = \frac{\gamma}{\sigma} \langle U_m \rangle$. The mean field susceptibility may then increase to very high values $\chi \sim \left(\frac{\gamma}{\sigma} - \mu\right)^{-1} \rightarrow \infty$ on the verge of excitability, thereby explaining the large fluctuations and long range correlations observed.

The argument above fails firstly because it only tells us locally that cycles will be triggered almost with no threshold. Secondly, on a global scale, the narrowness of the critical Ginzburg region in parameter space prevents any wild collective effect to become observable [42]. Taking the order of magnitude of the diffusive length of about $l_c \approx 1 \text{ mm}$ and bringing it next to the microscopic cut-off length, the maximum between the gap junction wall thickness $\Lambda \approx 100 \text{ nm}$ and the Debye length, here about $\lambda_D \approx 10 \text{ nm}$, one obtains a very narrow width of the parameter range, entirely unobservable in practice $\delta\chi^{-1} \sim \Lambda^2 l_c^{-2} \lesssim 10^{-10}$.

This rules out near equilibrium critical fluctuations in ordinary excitable media. We have realized however that mean field arguments break down when the ionic exchange current at the gap junction alters the effective potential energy of the cell, in such a way as to restore a continuous symmetry, and approach an effective critical region.

3 Incorporation of cell to cell dynamical coupling

The works in [43] [44] [45] show the crucial role played by the gap junctions, since they are supposed to guarantee good coupling between the cells. However, in excitable models it is not clear how bad conduction can be modelled. According to near equilibrium thermodynamics, the exchange current may simply be written down as $J_e = -g_s \nabla U_m$, where g_s is a stationary conductance. The point is to demonstrate that the perturbation of the opening and closing of the gap junction channels induce some time lag in the activation of the cell.

Typical relaxation times of gap junctions are much larger than those of membrane polarisation, but compare well with membrane repolarisation time scales. On average they are of order $\gtrsim 100 \text{ ms}$ [46]. There is thus no alternative but to consider the full kinetics of the gap junctions, at such high frequencies as found in arrhythmias. This is a crucial aspect missing in common models for arrhythmias. Applying common wisdom on membrane physico-chemistry to the gap junctions, replacing U_m with ∇U_m , yields a kinetic relaxation equation of the form [2]

$$\frac{\partial}{\partial t} g = a(\nabla U_m) (g_0 - g) - b(\nabla U_m) g, \quad (4)$$

where the functions $a(\nabla U_m)$ and $b(\nabla U_m)$ are the respective average rates of opening and closing of the gap junction channels. The constant g_0 is a typical

maximum resting value, essentially $g_s = g_0 \frac{a}{a+b}$. The gradient is the one felt at the gap junctions. So we turn to the question of how the electrical force $-\nabla U_m$ can be strong enough as to perturb a and b in order to make the current deviate from electro-diffusion. Since a pulse front of typical width l_c encompasses many cells, the voltage difference $\sim \Lambda \nabla U_m$ at a gap junction cannot be as strong as the one felt across membranes. Nevertheless, gap junction channels have a very distinctive role in inter-cellular communication. They are open at rest state, and very long molecules permeate through. They are therefore inclined to a modulation of their permeability, depending on the concentration levels of some messenger molecules [47]. We explore here this possibility, letting some ions act on the gap junction properties. This will simply arise from their naturally slow linear response to the presence of high ionic concentration.

In that respect, there exists a point of view that allows us to characterise the ionic flow by a dimensionless number. For certain values of this dimensionless number, an instability will occur for the most unstable mode [48], which eventually will develop dissipative structures [49] [50]. Upon forcing the system to higher values, secondary instabilities may destabilise the primary structures, leading to a broad spectrum of modes [51].

To construct our model, we basically use charge conservation and a kinetic equation for the gap junction channel average opening under proper thermodynamic forcing. As is depicted in fig.(4), we consider an excess charge sitting at the gap junction, and its effect on the equilibrium dynamics. The force

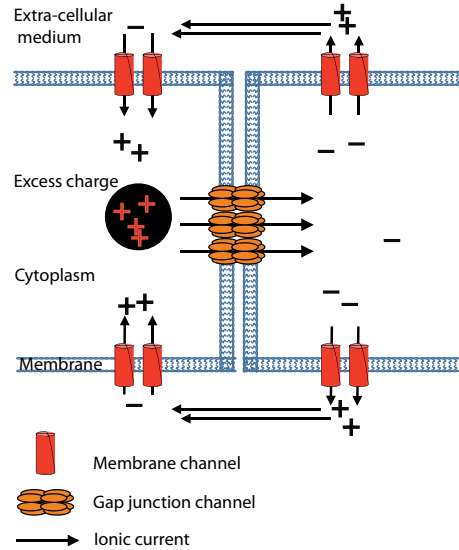


Fig. 4. Excess of positive charge (black) sitting next to the gap junction channels. Arrows indicate inter-cellular flows, which are generally supposed to be diffusive.

is simply the electro-chemical gradient. In 1D, as the sketch suggests, take a

finite volume element \mathcal{V} spanning the gap junction, incorporating the excess charge and extending to the membranes. Noting ρ the excess density, charge conservation inside this volume reads $\frac{\partial}{\partial t}\rho = -\tilde{g}\nabla U_m$, where the gradient is understood as a finite difference over the closed surface. We used a perturbed conductance \tilde{g} , which is the important assumption in our model. It states that excess charge density variations overrate the stochastic averaging of the opening and closing of the channels, that would otherwise set the conductance to its equilibrium value. Therefore, we need to consider eq.(4), which we will linearise as $a(\nabla U_m) = \alpha\rho + a_0$, with α a control parameter, and $b = b_0$ for the sake of simplicity of the demonstration. This linearisation simply stipulates that the excess charge amounts to $\mathcal{V}\rho \approx C\nabla U_m$, with a gap junction effective capacitance C . Note that the extra cellular medium is supposed to rest at a constant potential reference.

The combined equations basically say that excess charges are swept along the small scale gradients (excess charges will tend to average out over large volume elements comprising many cells), while variations of the conductance remain local. Denoting $\nu = a_0 + b_0$, dropping the tilde for clarity, we get the following system of equations

$$\begin{cases} \frac{\partial}{\partial t}U_m = \mu U_m - \beta U_m^3 - J_m + D\Delta U_m - \nabla(g\rho) \\ \frac{\partial}{\partial t}J_m = \gamma U_m - \sigma J_m \\ \frac{\partial}{\partial t}g = \alpha\rho - \nu g \\ \frac{\partial}{\partial t}\rho = -g\nabla U_m - \nu_2\rho \end{cases}, \quad (5)$$

where we have let the capacitance and volume $C \equiv 1$, $\mathcal{V} \equiv 1$ without loss of generality. The locally perturbed current is $g\rho$ by construction. The evaporation rate ν_2 is a local simplification of charge diffusion, for a fixed length scale, and is meant to be small. This set is not parity invariant, and by construction one needs to take an opposite α to change directions of front propagation from the location of a source, since the potential gradient will reverse sign.

As we described above, some important perturbations of the dynamics may emerge at slow time scales. Indeed, this simple model is in spirit quite comparable to a kind of Rayleigh instability, where α plays the role of the gravitational pull. Because the interface is fixed at the gap junction, no convective term is present. More precisely, when only two cells are coupled with one free boundary, notice indeed how the first, third and fourth equations have the same structure as the Lorenz system of ODE (where the opposite limit $\mu \rightarrow 0$ holds though). The analogue Rayleigh dimensionless number is here $\mathcal{R}_a \equiv \frac{\alpha\rho}{L\nu\nu_2}$, which controls the effect of thermodynamic forcing over dissipation, where L is an equilibrium length associated with the slow time scales. In fact, we force the system at one end with an automatic cell (a very rapid abnormal pacemaker), or similarly with an abnormal current leak J_0 . Now, since on average we will have $D\langle \frac{\rho}{L} \rangle \approx J_0$, it is possible to rewrite

$$\mathcal{R}_a \equiv \frac{\alpha J_0}{D\nu\nu_2}. \quad (6)$$

So we expect a transition point towards chaos around $\mathcal{R}_a \sim 1$, for very small arrays, of two to a very few cells, and to turbulence in longer arrays. This transition to high dimensional chaos is illustrated in fig.(5).

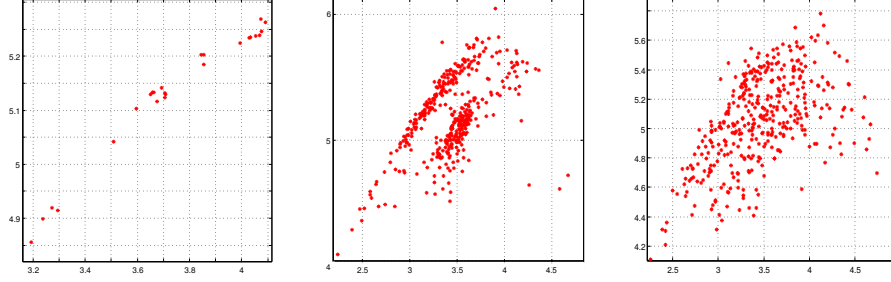


Fig. 5. Poincaré section plots (ρ, g) , from maxima of U_m , for 2, 3 and 4 cells coupled linearly, in the special case $\mu = 0$ and $\sigma \rightarrow \infty$. The section on the left is from the famous Lorenz attractor. One notes the spreading of points revealing the increase of the attractor dimension.

It is easy to quickly check the validity of this argument numerically. Starting with parameters for which we observe regularity of beats and rhythm, decreasing D , ν_2 or ν , and raising α makes it possible to reach a domain of turbulent dynamics of ρ and g , that strongly affect U_m and J_m , see fig.(6). Here, we provide an illustration of the turbulent domain with the same numer-

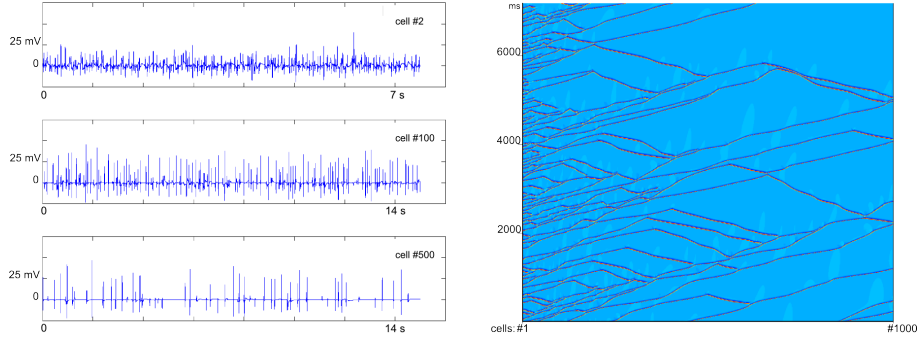


Fig. 6. Some traces of the gap current divergence, in the model in 1D, from near a source of abnormal automaticity, cell #0, to further away. Spatio-temporal map of action potentials showing many back-scattering and some front splitting in a hierarchical structure of propagation, since the ones that escape collisions rarefy. $\mu = 1$, $\beta = 1$, $\gamma = 0.008$, $\sigma = 0.02$, $\alpha = 0.01$, $\nu = 0.01$, $\nu_2 = 0.0001$

ical values of the parameters as in fig.(6). We do find similar properties for the numerical data as for the experimental data. It seems indeed that long range

auto-correlations decrease as $\sim t^{-1}$ power laws. As shown in fig.(7), probability density distributions of the current divergence scale in the same way. We find non universal exponents, which appear to decrease with distance from the source. Just as strikingly, the broad singularity spectra, with a substantial

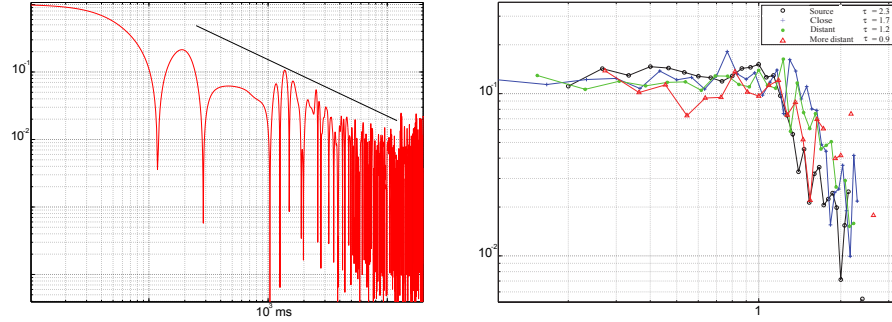


Fig. 7. Loglog plot of the auto-correlation of cell #5, with an indicative t^{-1} plot (left). Empirical collapse function G for the model (right), with non universal exponents, decreasing with distance from the source for arbitrary cells, shown #2, #20, #80, and #400.

contribution of negative exponents, can be superposed completely, see fig.(8). This tends to demonstrate the presence of an identical random cascade process underlying the dynamics.

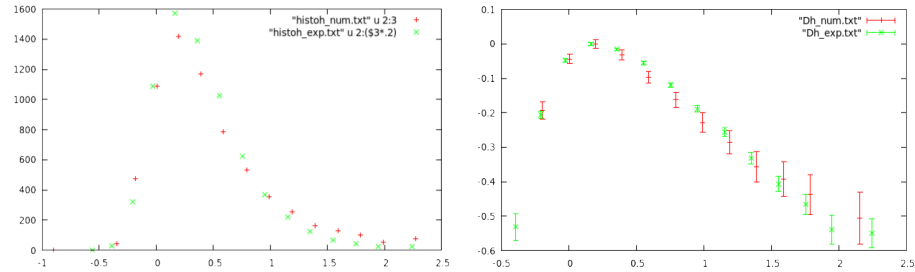


Fig. 8. Strikingly good superposition of the broad histograms (left) and fractal dimension spectra (right) of the sets of singularity exponents h defined locally, for small τ of a few ms , as $\langle \int^\tau dt \frac{\partial}{\partial t} \nabla g \rho \rangle \sim \tau^h$. They were obtained from the same experimental data as in fig.(2) and the 1D numerical data as in the previous figures for an average over 10 cells taken at random spanning the first 100 cells.

The transient time that the turbulent state takes to pervade the system could be related to the electrical remodelling. We observe a typical time scale that reads like $T \sim L^z$, with $z \approx 1$. For typical length of human atrial fibres, it happens to fall in the physiologically recorded range of about a few minutes

[52]. Finally, system size should affect the onset of turbulence as expected, and consistently distance from the source affects scaling exponents as we have found, see fig.(7). This basically marks the hierarchical propagation pattern. In practice, this could be good news for a quantitative method of finding abnormal sources of activity in the heart, a highly valued goal pursued by medical practitioners and physiologists.

This phenomenology holds in two dimensions with isotropic coupling as well. Note also that the propagation of perturbing charges is like some effective diffusion of the inhibitor. Therefore, considering the anatomical organisation of the myocardium in fibre bundles and the anisotropy of conducting properties, one expects fronts to split along their direction.

By chance, in three dimensions various topological arguments convey the idea that the ventricles are better equipped to resist such onset of very irregular patterns. Thus far, one may have in mind natural selection to understand the Aschoff-Tawara node, which function is somehow to low-pass filter the activity of the atria, before relaying it to the ventricles.

4 Discussion and conclusion

The large oscillations of pulses and the intermittency are quite intriguing at first, since μ is the dominant parameter, which guarantees the stability of U_0 against any spontaneous fluctuation. In fact, a phase approximation of the dynamics is indeed relevant in this sector. Then, what is seen might signal the restoration of a continuous symmetry for the dynamics of the phase, that finds itself effectively at criticality.

Firstly, upon appropriate rescaling, define a complex scalar $\Psi = U_m + iJ_m = Ae^{i\theta}$. The phase $\theta(\mathbf{x}, t)$ is a distribution of ticks recording the passage and shape of pulses. Since μ defines the rapid time scale, it is natural to consider a fixed amplitude of Ψ . Let us model the perturbation caused by the ionic gap currents as some local time delay φ for the onset of depolarisation. The equation for the phase then reads

$$\partial_t \theta = D\Delta\theta - H \sin(\theta + \varphi(\mathbf{x})) + F, \quad (7)$$

where H and F define characteristic scales that can be made to match that from \mathcal{R} and \mathcal{G} , such as the domain wall thickness $l_c \sim \sqrt{H^{-1}}$. Taking a random distribution of phase in the range $\varphi(\mathbf{x}) \in [0, 2\pi]$, random pinning is facilitated. This governs the behaviour of charged density waves in impure magnetic materials [53] [54] [55] [56]. Naively, an effective critical state could be reached from the average of random phases $\mu_{eff} \sim \langle H \cos(\varphi) \rangle$, though the model equation does not reduce to critical dynamics, model A in [57]. Basically, one can find in the literature the anomalous scaling of the velocity jumps of the density waves, that reads like $\delta v \propto F^\xi$ with $\xi \neq 1$, near the forcing threshold of the depinning transition (insulating to conducting). SOC is typically found in those systems [58]. Counting consecutive phase slips, one finds a distribution of avalanches that typically scales with system size, a cut-off measuring a distance to a critical point, in a form like eq.(1), where the exponent τ is related to ξ [59] [29].

Hence, one notes that avalanches of phase slips, within a surrounding closed contour, must be related to large amplitude variations of the bulk average. Heuristically, the argument is quite suggestive of multi-scaling. From the slowly varying random aspect of the noise term emerges a random cascade. It is tempting to model this dynamical effect by a mean field multiplicative noise $\mu \mapsto \tilde{\mu}(J_0, \mathbf{x}, t)$ acting on top of diffusion, leading to large deviations as captured by the observed singularity spectra [39], and percolating paths [60]. In fact, chaotic coupled map lattices are known to show desynchronisation patterns in the universality class of the KPZ equation[61][62].

In conclusion, we have presented data, from humans with a very irregular arrhythmia, that seem to exhibit patterns of hydrodynamic intermittency. We showed that such fluctuations could not emerge from purely excitable dynamics, and found out a good alternative candidate, namely intrinsic modulations. We devised a model of ionic flows through the gap junction channels of a cardiac tissue, that effectively modulate otherwise independent pulses. The observed abnormal patterns finely match the ones from the model, when the flow is intermittent. It is the first to manifest a transient related to the degradation of pulse propagation, called electrical remodelling, and to suggest a relationship between local exponents in the signal with the distance to an abnormal source.

In that respect, we would like to believe that our model may further illustrate Y. Pomeau's conjecture, relating hydrodynamic intermittency with some directed percolation of metastable orbits.

At any rate, these results are clear evidence of the role of the dynamical coupling of the network of cells, which do not form a true syncytium.

References

1. D. P. Zipes and H. J. J. Wellens. *Circulation*, 98:2334, 1998.
2. A. L. Hodgkin and A. F. Huxley. *J. Physiology*, 117(4):500, 1952.
3. B. van der Pol and J. van der Mark. *Phil. mag. series 7*, 38(6), 1928.
4. D. Noble. *J. Physiology*, 160:317, 1962.
5. R. Fitzhugh. *Mathematical models of excitation and propagation in nerve*. H.P. Schwan (Ed.), Biological Engineering, McGraw-Hill, New York, 1962.
6. J. Nagumo, S. Arimoto, and S. Yoshizawa. *Proc. IRE*, 50:2061, 1962.
7. M. R. Guevarra and L. Glass. *J. Math. Biology*, 14:1, 1982.
8. L. Glass, M. R. Guevarra, A. Shrier, and R. Perez. *Physica 7D*, page 89, 1983.
9. U. Parlitz and W. Lauterborn. *Phys. Rev. A*, (36):1428, 1987.
10. M. R. Guevarra and L. Glass. *IEEE Computers in Cardiology*, page 167, 1984.
11. A. Karma. *Chaos*, 4:461, 1994.
12. P. Attuel et al. *Int. J. Cardiol.*, 2:179, 1982.
13. M. A. Allesie, F. I. M. Bonke, and F. J. G. Schopman. *Circ Res.*, 41(1):9, 1977.
14. E. Meron and P. Pelcé. *PRL*, 60(18):1880, 1988.
15. A. Hagberg and E. Meron. *Phys. Rev. Lett.*, 72(15):2494, 1994.
16. I. S. Aranson and L. Kramer. *Rev. mod. Phys.*, 74(1):99, 2002.
17. J. Lajzerowicz and J. J. Niez. *Journal de Physique Lettres*, 40(7):165, 1979.
18. P. Coullet, J. Lega, B. Houchmanzadeh, and J. Lajzerowicz. *Phys. Rev. Lett.*, 65(11):1352, 1990.
19. T. Frisch, S. Rica, P. Coullet, and J. M. Gilli. *Phys. Rev. Lett.*, 72(10):1471, 1994.

20. A. Garfinkel et al. *J. clinical investigation*, 99(2):305, 1997.
21. A. Karma. *Phys. Rev. Lett.*, 71(7):1103, 1993.
22. A. T. Winfree. *Science*, 266(5187):1003, 1994.
23. F. H. Fenton, E. M. Cherry, H. M. Hastings, and S. J. Evans. *Chaos*, 12(3):852, 1993.
24. A. Hagberg and E. Meron. *Chaos*, 4(3):477, 1994.
25. P. Attuel, P. Coumel, and M.J. Janse. *The atrium in health and disease*. Mount Kisco, NY: Futura Publishing Co., 1st edition, 1989.
26. M. C. Wijffels, C. J. Kirchhof, R. M. Dorland, and M. Allesie. *Circulation*, 92:1954, 1995.
27. Y. Pomeau. *Physica 23D*, page 3, 1986.
28. M. Argentina and P. Coullet. *Phys. Rev. E*, 56(3):R2359, 1997.
29. K. Dahmen and J. P. Sethna. *Phys. Rev. B*, 53(22):14872, 1996.
30. J. C. McClure Jr. and K. Schroder. *C R C Critical Reviews in Solid State Sciences*, 6(1):45, 1976.
31. J. S. Urbach, R. C. Madison, and J. T. Market. *Phys. Rev. Lett.*, 75(2):276, 1995.
32. C. J. Olson, C. Reichhardt, and Franco Nori. *Phys. Rev. B*, 56(10):6175, 1997.
33. E. Altshuler et al. *Phys. Rev. B*, 70:140505, 2004.
34. J. M. Beggs and D. Plenz. *J. Neurosci.*, 23(35):11167, 2003.
35. C.-W. Shin and S. Kim. *Phys. Rev. E*, 74:045101(R), 2006.
36. L. de Arcangelis, C. Perrone-Capano, and H. J. Herrmann. *Phys. Rev. Lett.*, 96:028107, 2006.
37. J. Hesse and T. Gross. *Front. Syst. Neurosci.*, 8:166, 2014.
38. S. Ciliberto and P. Bigazzi. *Phys. Rev. Lett.*, 60(4):286, 1988.
39. U. Frisch. *Turbulence: The legacy of Kolmogorov*. Cambridge University Press, 1995.
40. B. Hille. *Ion channels of excitable membranes, 3d edition*. Sinauer associates, Inc., 2001.
41. A. Panfilov and P. Hogeweg. *Phys. Lett. A*, 176:295, 1993.
42. L. Landau and E. M. Lifchitz. *Physique statistique*. édition MIR Ellipses, 4th edition, 1994.
43. Y. J. Chen, S. A. Chen, M. S. Chang, and C. I. Lin. *Cardiovascular Res.*, 48:265, 2000.
44. G. Bub, A. Shriner, and L. Glass. *Phys. Rev. Lett.*, 88(5):058101, 2002.
45. G. Bub, A. Shriner, and L. Glass. *Phys. Rev. Lett.*, 94:028105, 2005.
46. H.-Z. Wang, J. L. Jian, F. L. Lemanski, and R. D. Veenstra. *Biophys. J.*, 63:39, 1992.
47. J. Neyton and A. Trautmann. *J. Exp. Biol.*, 124:93, 1986.
48. M. C. Cross and P. C. Hohenberg. *Rev. Mod. Phys.*, 65(3):851, 1993.
49. P. Glansdorff and I. Prigogine. *Thermodynamic Theory of structure, stability and fluctuations*. Wiley-Interscience, John Wiley & Sons Ltd., 1971.
50. I. Prigogine and G. Nicolis. *Quarterly Reviews of Biophysics*, 4(2 & 3):107, 1971.
51. P. Bergé and M. Dubois. *Le journal de physique-Lettres*, (10).
52. E. G. Daoud et. al. *Circulation*, 94:1600, 1996.
53. H. Fukuyama and P. A. Lee. *Phys. Rev. B*, 17(2):535, 1978.
54. P. A. Lee and T. M. Rice. *Phys. Rev. B*, 19(8):3970, 1979.
55. M. J. Rice. *Phys. Rev. Lett.*, 36(8):432, 1976.
56. G. Grüner. *Rev. Mod. Phys.*, 60(4):3970, 1979.
57. P. C. Hohenberg and P. C. Hohenberg. *Rev. Mod. Phys.*, 49(3):435, 1977.
58. C. R. Myers and J. P. Sethna. *Phys. Rev. B*, 47(17):11171, 1993.
59. D. S. Fisher. *Phys. Rev. Lett.*, 50(19):1486, 1983.
60. H. Hinrichsen. *Advances in Phys.*, 49(7), 2000.

- 61. G. Grinstein, David Mukamel, R. Seidin, and Charles H. Bennett. *Phys. Rev. Lett.*, 70(23):3607, 1993.
- 62. P. Grassberger. *Phys. Rev. E*, 59(3):R2520, 1999.

Localized patterns of sand ripples generated by steady flows: experimental and theoretical study

Anthony Auzerais¹, Armelle Jarno¹, Alexander Ezersky², and François Marin¹

¹ LOMC, UMR 6294 CNRS, University of Le Havre, Le Havre, France

(E-mail: anthony.auzerais@univ-lehavre.fr)

(E-mail: armelle.jarno-druaux@univ-lehavre.fr)

(E-mail: francois.marin@univ-lehavre.fr)

² M2C, UMR 6143 CNRS University of Caen, Caen, France

(E-mail: alexander.ezersky@unicaen.fr)

Abstract. In recent decades, the study of mechanisms of localized structures formation in non-equilibrium media attracted attention of researchers. Such structures were found in chemically active media, in granular materials, and in many numerical experiments with model equations. In this paper we investigate theoretically and experimentally localized patterns on sandy bottoms arising under the influence of steady flows in the vicinity of vertical obstacle. Present experiments performed in a hydrodynamic channel show that spatially periodic quasi-stationary patterns whose width increases downstream in the wake of an obstacle arise from a sub-critical instability of the water-sandy bottom interface. We study the dependence of the topology of the area occupied by patterns on the flow velocity. It is shown that the characteristics of pattern on the bottom can be explained using the Swift-Hohenberg equation. Experiments show that for a correct description of structures, supplemented terms which take into account the impact of the vortices arising in the wake of an obstacle must be added into the Swift-Hohenberg equation.

Keywords: Sand ripples, pattern formation, steady currents, vortices, Swift-Hohenberg equation.

1 Introduction

The interface between water flow and sand bottom is unstable to perturbations with zero phase velocity. This instability is studied in detail for over a hundred years (Dey 2014 [2]). It was found that the development of this instability may lead to the generation of different stationary patterns at the bottom: roller structures, modulated rollers, cellular structures consisting of rhombus or squares. These structures were studied in detail for the case of super critical instability when spatially periodic pattern arose from infinitesimal perturbations and occupied the area substantially greater than the period of the pattern. In

8th CHAOS Conference Proceedings, 26-29 May 2015, Henri Poincaré Institute, Paris France

© 2014 ISAST



this paper, we investigate the localized patterns. These patterns appear on the sandy bottom as a result of sub critical instability under the influence of finite-amplitude perturbations. Finite amplitude perturbations can be caused by an obstacle in the flow. It should be noted that around an obstacle, under the influence of vortices in the sandy bottom there appears a deepening - a localized structure, the so-called scour (Breusers *et al.* 1977 [1], Hoffmans and Verheij 1997 [5], Niedorada 1982 [8], etc.). Features of the scour have been investigated in detail, as they are essential for the design of hydraulic structures (Qi and Gao 2014 [9], Melville and Coleman 2000 [7], Sumer and Fredsøe 2002 [10], Whitehouse 1998 [12], Ettema 2011 [3], etc.). Our research concerns sand structures appearing under the influence of vortices in the wake at some distance from the obstacle. In our experimental conditions in the absence of vortex, the boundary water - sand is stable with respect to small perturbations. Vortices contribute to finite perturbations and initiate development patterns on the sandy bottom. Such a mechanism of occurrence of localized patterns is investigated in this paper. Paper is organized as follows. First of all, we present the hydrodynamic channel where experiments are performed, followed by results we obtained. After this, we present a theoretical model and a comparison of these experimental and theoretical results is exposed to finally conclude.

2 Methods and materials

The experiments were carried out in a 0.5 m wide, 10 m long flume in 0.2 cm water depth. This hydrodynamic channel is able to generate a current as illustrated in Figure 1:

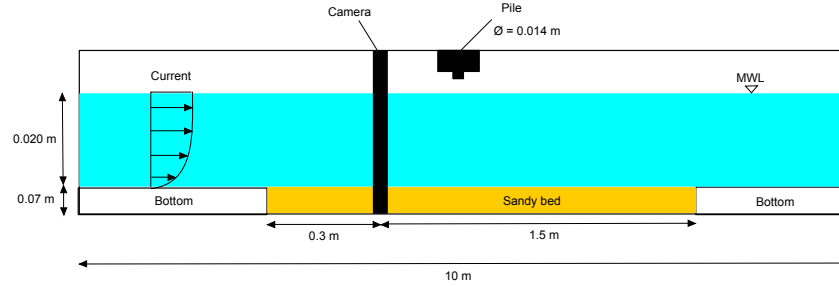


Fig. 1. Sketch of the experimental setup

We adopted a bed consisting of a 0.07 m sand layer where a cylindrical cylinder with diameter $D=0.014\text{m}$ is embedded. The sediments have a relative density $s = 2.7$ and a median size $D_{50} = 340\mu\text{m}$. The experiments were performed under current without waves in subcritical regime ($\theta < \theta_c$), where θ is the Shields number:

$$\theta = \frac{\tau_0}{(\rho s - \rho) \cdot g \cdot D_{50}} \quad (1)$$

τ_0 the bed shear stress, ρ_s the density of the sediment, ρ the density of the fluid and g the acceleration due to gravity. Shields number is a dimensionless number that represents the ratio between the forces which tend to move the sediments and those which stabilize the sediments and above a critical threshold (θ_c), the live-bed regime is reached. All our experiments were carried out in the clear-water regime ($\theta < \theta_c$), thus, the sediment transport is only due to the presence of the cylinder, generating vortices responsible of particles motion. To characterize the flow, we use the Reynolds number defined as follows:

$$Re = \frac{V.H}{\nu} \quad (2)$$

where V is the mean velocity of the flow, H the water depth and ν the kinematic viscosity of the fluid. To characterize regime in Karman street, another Reynolds number is used:

$$Re_d = \frac{V.d}{\nu} \quad (3)$$

with d the diameter of cylinder.

In order to estimate the pressure forces acting at the soil-water interface, we used an optical method, namely the particle image velocimetry (PIV) as shown in Figure 2, without sediment:

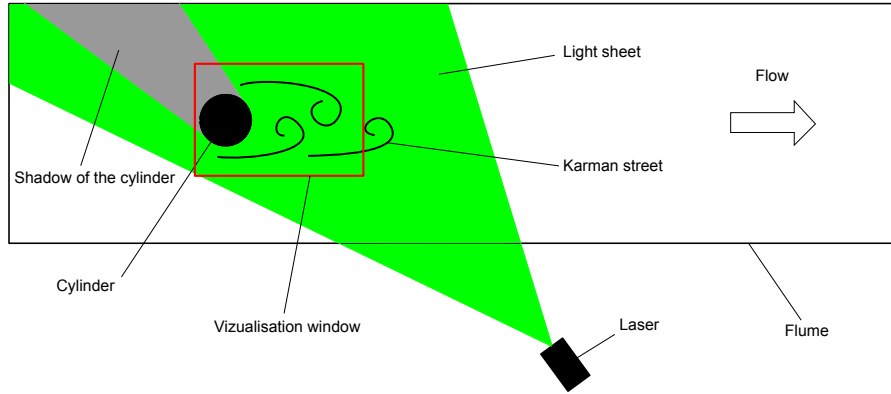


Fig. 2. Sketch of the PIV

This method allows to obtain the velocity field near the bottom and to deduce the hydrodynamics forces acting on the sand bed, using a horizontal laser plane. The acquisition frequency is 15 Hz, the visualisation window side is 12 x 8 cm and the resolution of the camera is 4 Mega pixels.

3 Experimental results

In the experiments, we observed sediment structures formed downstream the cylinder. The experiments were performed during 50 hours at least to be sure to reach the quasi-equilibrium state of formed patterns. Patterns are shown below in Figures 3, 4 and 5 for a Reynolds number Re of 38000, 42000 and 43000, respectively:

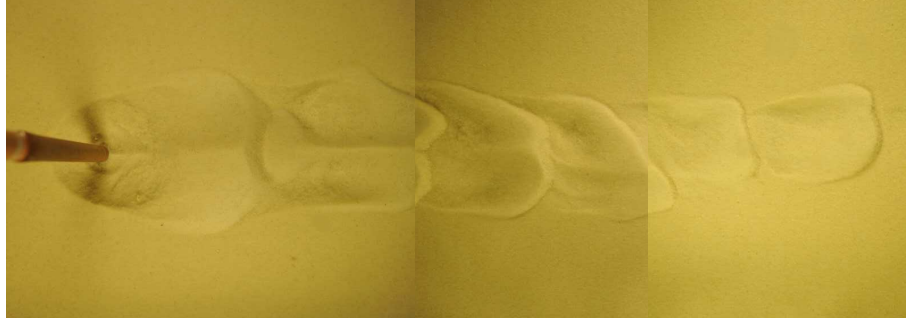


Fig. 3. Sedimentary structures downstream the cylinder; $Re=38000$ (Test 1)

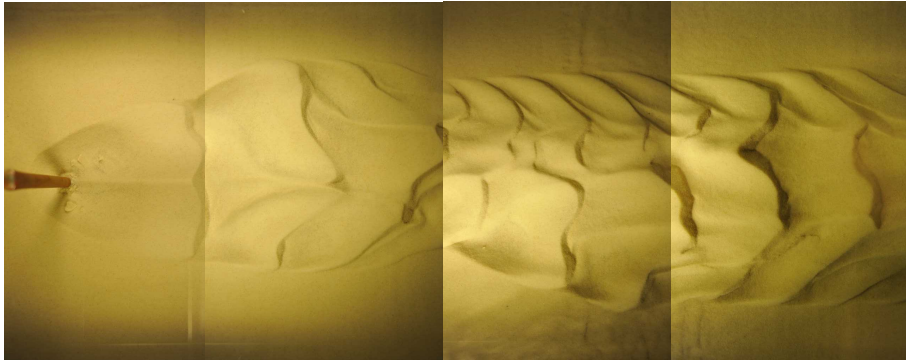


Fig. 4. Sedimentary structures downstream the cylinder; $Re=42000$ (Test 2)

A significant change between the patterns is the lateral extension of sediment structures (transversal width) which is function of the velocity flow. Indeed, this lateral extension increases with the velocity flow. It can be observed that a slight variation of the Reynolds number Re leads to an important difference of width for the transversal and longitudinal extension.

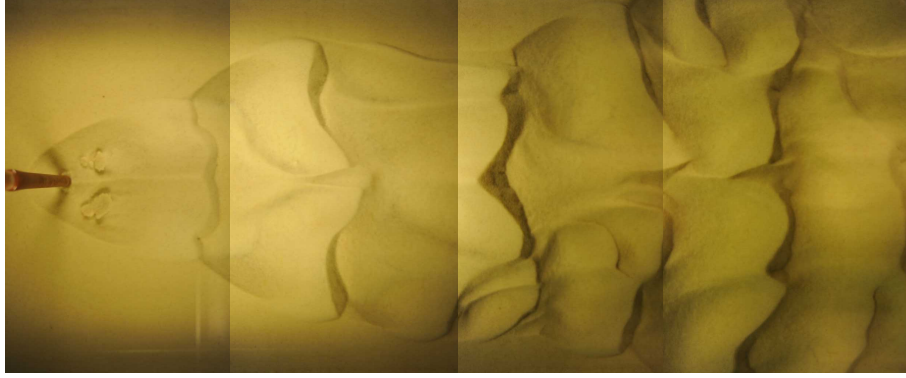


Fig. 5. Sedimentary structures downstream the cylinder; $Re=43000$ (Test 3)

Let us consider the velocity fluctuations field, shown in Figure 6 for $Re=42000$:

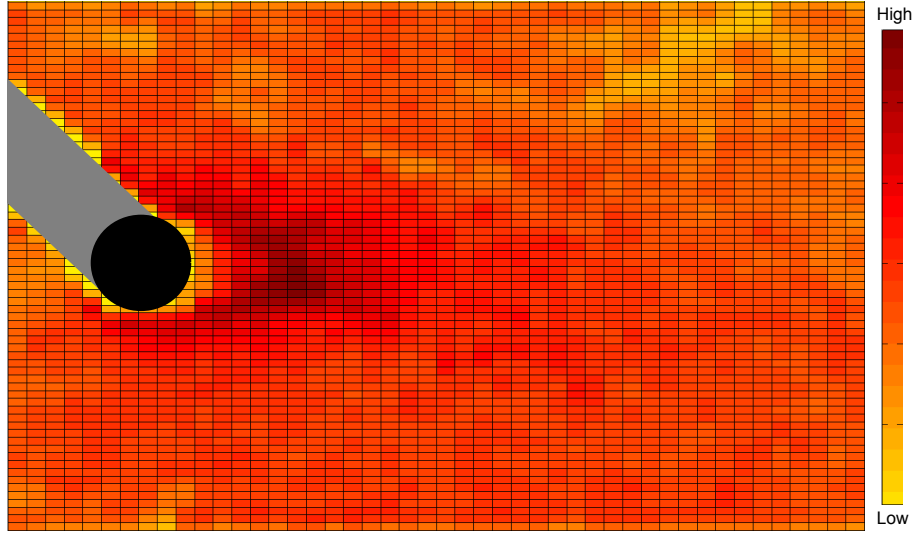


Fig. 6. Amplitude of velocity fluctuations in an horizontal plane 2 cm above the bed ($Re=42000$)

We observe that the amplitude of velocity fluctuations is very important right behind the cylinder; this amplitude decreases for increasing values of the distance to the cylinder, and increases for increasing values of Re_d . However, the size of the area with a high amplitude is the same regardless the value of Re_d .

4 Theoretical model

In order to modelize the observed patterns, we use the Swift-Hohenberg equation (Swift and Hohenberg [11]), a phenomenological equation:

$$\frac{\partial u}{\partial t} = \varepsilon u - (1 + \nabla^2)^2 u + qu^2 - u^3 \quad (4)$$

where:

$$\nabla = \vec{x}_0 \frac{\partial}{\partial x} + \vec{y}_0 \frac{\partial}{\partial y} \quad (5)$$

ε corresponds to the linear instability of the system. In this equation, instability to infinitesimal perturbations occurs if $\varepsilon > 0$. If $\varepsilon < 0$, linear instability is absent. q corresponds to quadratic instability.

Swift-Hohenberg equation is widely used to describe pattern formation (Lloyd and Sandstede [6], Hilali *et al.* [4], etc.). With a flow in one direction, this equation becomes:

$$\frac{\partial u}{\partial t} = \varepsilon u - \left(1 + \frac{\partial^2}{\partial x^2}\right)^2 u + \frac{\partial^2}{\partial y^2} u + qu^2 - u^3 \quad (6)$$

In our case, $\varepsilon < 0$ because our experiments were carried out in subcritical regime ($\theta < \theta_c$), therefore patterns forms only in the wake of the cylinder where velocity and pressure perturbations are important.

This equation can be modified as follows:

$$\frac{\partial u}{\partial t} = -Eu - \left(1 + \frac{\partial^2}{\partial x^2}\right)^2 u + \frac{\partial^2}{\partial y^2} u + qu^2 - u^3 + f(x, y, t) \quad (7)$$

E is proportional to $V - V_c$ where V is velocity of flow in our experiments. It means that if $V > V_c$ (V_c is critical velocity), $E < 0$ instability occurs everywhere, and if $V < V_c$, $E > 0$ instability occurs in the wake of the cylinder, where perturbations with final amplitudes exist. We take into account the influence of these perturbations adding force $f(x, y, t)$ into Swift-Hohenberg equation. We suppose that this force is proportional to V^2 , where V^2 is spatially modulated random field, because for Reynolds numbers Re_d of several thousand in our experiment turbulent Karman street is observed. Amplitude of velocity fluctuations is approximated using experimental data presented in Figure 6. The shape of this force can be qualitatively explained as follows.

According to Bernoulli's equation, we can write along a streamline:

$$P + \rho \frac{V^2}{2} = \text{constant} \quad (=) \quad P = \text{constant} - \rho \frac{V^2}{2} \quad (8)$$

a decrease of pressure inducing an increase of velocity, low pressure corresponds to positive forces acting at the sand-water interface. This force introduces perturbations on water-sand bottom interface.

5 Comparison theory-experiments

The theoretical model allows to reproduce qualitatively the patterns observed experimentally, test parameters are listed in Table 1. Figures 7,8 and 9 show the superposition of theoretical and experimental results. At the bottom of Figure 7, the perturbation (due to the cylinder) resulting in patterns formation has a limited size, in particular with a weak lateral extension of sediments downstream the cylinder. The corresponding theoretical result at the top of Figure 7 displays patterns which are qualitatively in good agreement with those observed for present experiments.

Experimental tests				Theoretical tests			
Test number	1	2	3	Test number	1	2	3
Test duration (h)	70	68	65	Integrations numbers	30	30	30
Re	38000	42000	43000	E	0.23	0.14	0.07
Re_d	2660	2940	3010	q	1.6	1.6	1.6

Table 1. Tests parameters

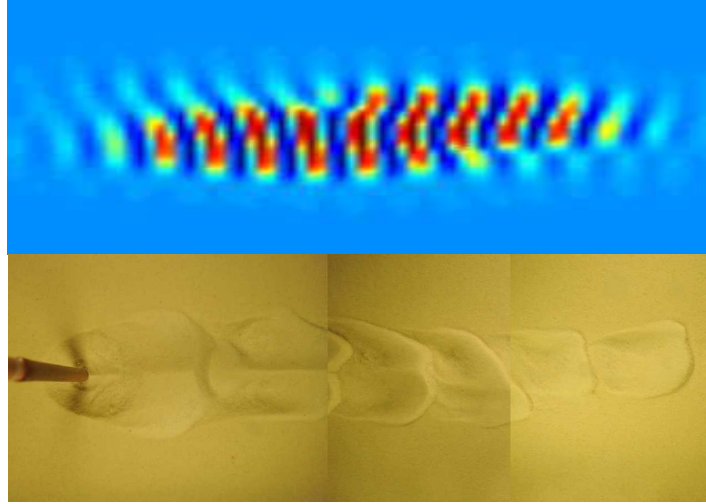


Fig. 7. Top: theory; Bottom: experiment (Test 1)

As far as the other tests are concerned, Figures 8 and 9 show that the pattern width increases for increasing values of the Reynolds number Re . This leads to a decrease of the value of the parameter E in the Swift-Hohenberg equation to obtain a similar description of experimental patterns. Thereby, the patterns simulated with the present theoretical model are consistent with our experimental results.

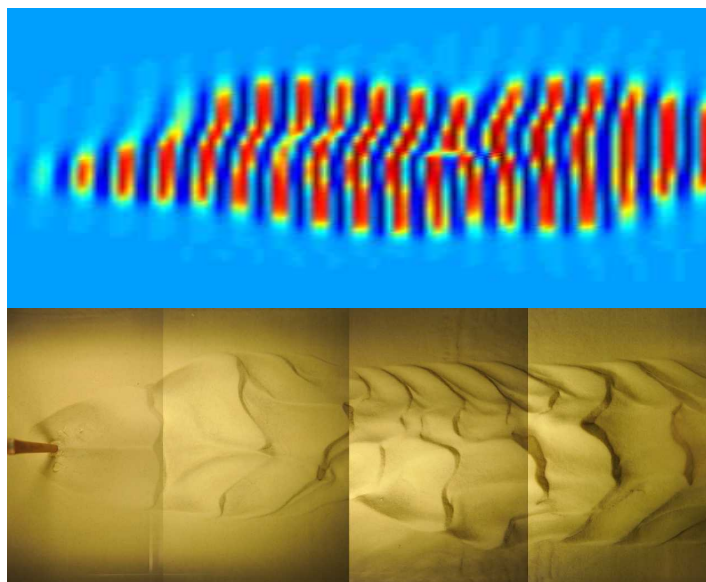


Fig. 8. Top: theory; Bottom: experiment (Test 2)

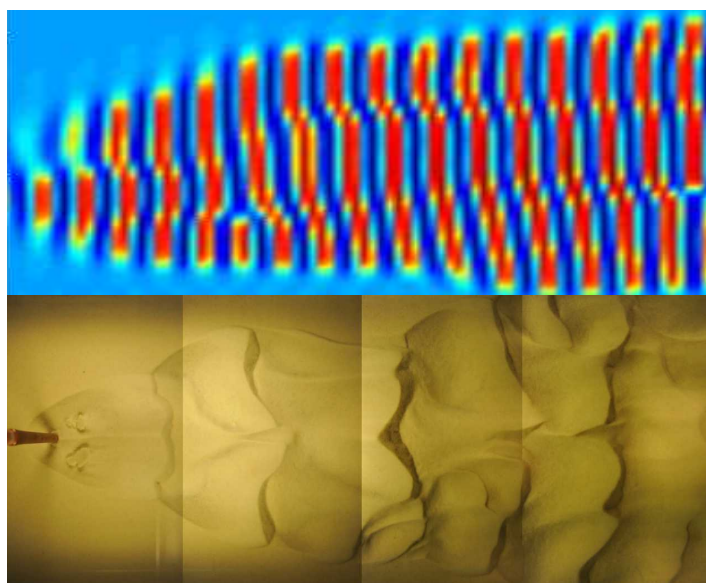


Fig. 9. Top: theory; Bottom: experiment (Test 3)

Conclusions

In this paper, we investigate theoretically and experimentally localized patterns on sandy bottoms arising under the influence of steady flows downstream of a vertical obstacle simulating a pile. Experiments carried out in a hydrodynamic channel show that spatially periodic quasi-stationary patterns whose width increases downstream in the wake of a vertical cylinder arise from a sub-critical instability of the water-sandy bottom interface. The width of these spatially periodic quasi-stationary patterns increases for increasing values of the flow velocity. It is shown that the characteristics of patterns on the bottom can be explained using the Swift-Hohenberg equation. Experiments show that for a correct description of sand structures, the variation of the parameter corresponding to linear instability is sufficient.

References

- [1] Nicollett G. Shen H. Breusers, H. Local scour around cylindrical piers. *J. Hydraul. Res.*, 15:211–252, 1977.
- [2] S. Dey. *Fluvial Hydrodynamics: Sediment Transport and Scour Phenomena*. Springer, 2014.
- [3] Constantinescu G. Melville B. Ettema, R. *Evaluation of Bridge Scour Research: Pier Scour Processes and Predictions*. Washington, DC, 2011.
- [4] Métens S. Borckmans P. Dewel G. Hilali, M’F. Localized hexagon patterns of the planar swift–shohenberg equation. *Physical review E*, 51(3):2046–2052, March 1995.
- [5] Verheij H.J. Hoffmans, G.J.C.M. *Scour Manual*. Rotterdam, Netherlands, 1997.
- [6] Sandstede B. Lloyd, D. J. B. Localized hexagon patterns of the planar swift–shohenberg equation. *J. Appl. Dynam. Syst.*, (7):1049–1100, June 2008.
- [7] Coleman S.E. Melville, B.W. *Bridge Scour*. LLC, CO, USA, 2000.
- [8] Dalton C. Niedorada, A. W. A review of the fluid mechanics of ocean scour. *Ocean Engng*, 9(2):159–170, 1982.
- [9] Gao F. Qi, W. Equilibrium scour depth at offshore monopile foundation in combined waves and current. *Sci China Tech Sci*, 57(5):1030–1039, May 2014.
- [10] Fredsøe J. Sumer, B.M. *The Mechanics of Scour in the Marine Environment*. Singapore, 2002.
- [11] Hohenberg P.C. Swift, J. Hydrodynamic fluctuations at the convective instability. *Physical Review A*, 15(1):319–328, January 1977.
- [12] R. Whitehouse. *Scour at Marine Structures: a Manual for Practical Applications*. London, 1998.

Acknowledgments

The authors express their sincere thanks to the High Normandy region (Scale Research Network) for funding this work.

Conductivity in Helicoidal DNA Wires

Sohrab Behnia¹ and Samira Fathizadeh²

¹ Department of Physics, Urmia University of Technology, Orumieh, Iran
(E-mail: s.behnia@sci.uut.ac.ir)

² Department of Physics, Urmia University of Technology, Orumieh, Iran
(E-mail: s.fathizadeh@sci.uut.ac.ir)

Abstract. Double helix structure of DNA is modeled by a steric oscillator network in a cylindrical reference system. The nonlinear nature of system allows to use of nonlinear dynamics and chaos theory tools. By using the mean Lyapunov exponent is chosen the best range of external parameters such as temperature and applied electrical field. The electrical current is obtained directly via the motion equations and then the current-voltage diagram achieved. As a result, we could report the emerging of quasi-Ohmic and negative differential resistance (NDR) phenomena in DNA. NDR devices are applicable in the switching circuits and electronic oscillators.

Keywords: DNA conductivity, Landauer resistance, Negative differential resistance, Chaos theory, Lyapunov exponent.

1 Introduction

DNA has always attracted much attention from different perspectives due to its main role in biological processes. Nevertheless in the last decade its electronic properties turned out to be a new promising field of study due to the search of new materials for nanotechnological aims such wires, transistors, diodes and molecular electronics [1]. Furthermore DNA assembling spontaneously has also revealed itself as a very useful building material to organize other higher conductive nanomaterials [2]. It is a great opportunity as well as a challenge to exploit DNA molecule as a programmable material for nanotechnology applications. A central problem of nanobioelectronics [3,4] is construction of molecular wires. During the past two decades a DNA molecule which was demonstrated to possess conductivity in many experiments [5,6] has been considered a promising candidate for this role. But, the DNA conductivity measurements performed by different research group show insulating to superconducting behavior [7–10]. Therefore, depending how the conductivity measurements are done, different conductivity results are obtained. So, understanding the charge transport mechanisms in nanoscale structures is essential for the development of molecular electronic devices. A number of theoretical explanations for DNA charge transfer phenomenon have been suggested on the basis of standard solid-state-physical approaches, like electrons or holes, polarons, solitons [11–14] but the

8th CHAOS Conference Proceedings, 26-29 May 2015, Henri Poincaré Institute, Paris France

© 2014 ISAST



situation is still far from working out a unique, non-contradictory theoretical scheme. In this work, the double helix structure of DNA is modeled by a steric oscillator network. In the context of the base-pair picture two different kinds of modes representing twist motions of the base pairs and H-bond distortions are coupled to the electron amplitude. Through the nonlinear interaction between the electronic and the vibrational degrees of freedom localized stationary states in the form of standing electron-vibron breathers are produced which we derive with a stationary map method.

2 Model and Methods

The helicoidal structure of DNA is conveniently described in a cylindrical reference system where each base pair possesses two degrees of freedom, namely a radial variable measuring the transversal displacements of the base pair (that is, deformations of the H-bond) and the angle with a reference axis in a plane perpendicular to the helix backbone which defines the twist of the helix [13]. The electron motion is described by a tight-binding system. The nonlinear interaction between the electron and the vibrational modes cause the formation of polarons and electron-vibron breathers. We pay special attention to the influence of an external field on the charge transfer in DNA. The external field control of rate processes and biochemical reactions has become of considerable interest recently [14]. Let us consider the DNA model Hamiltonian under the influence of an external electric field whose comprises four parts as follows [15,16]:

$$H = H_{el} + H_{rad} + H_{twist} + H_{field} \quad (1)$$

The electronic part is given by

$$H_{el} = \sum_n E_n |c_n|^2 - V_{n,n-1} (c_n^* c_{n-1} + c_n c_{n-1}^*) \quad (2)$$

where n denotes the site index of DNA and c_n determines the probability that the electron occupies this site. The on-site energies E_n being given by

$$E_n = E_n^0 + k r_n \quad (3)$$

Radial part of Hamiltonian (1) is modeled by

$$H_{rad} = \frac{1}{2} \sum_n M_n (\dot{r}_n^2 + \Omega_r^2 r_n^2) \quad (4)$$

where M_n is the reduced mass of the base pair and Ω_r stands for the frequency of the stretching vibrations. The transfer matrix elements $V_{n,n-1}$ are depend on the three dimensional distance between two consecutive bases in the following fashion

$$V_{n,n-1} = V_0 (1 - \alpha d_{n,n-1}) \quad (5)$$

The parameters k and α describe the strength of the interaction between the electronic and vibrational variables. $d_{n,n-1}$ is determined by

$$d_{n,n-1} = [a^2 + (R_0 + r_n)^2 + (R_0 + r_{n-1})^2 - 2(R_0 + r_n)(R_0 + r_{n-1}) \cos(\theta_0 + \theta_{n,n-1})]^{1/2} - l_0 \quad (6)$$

with

$$l_0 = \sqrt{a^2 + 4R_0^2 \sin^2(\theta_0/2)} \quad (7)$$

a is the distance between two neighboring base pair planes. $\theta_{n,n-1}$ is the relative angle between two adjacent base pairs measuring the displacement from the equilibrium twist angle θ_0 and R_0 denotes the radius between two adjacent base pairs at an equilibrium state. For simplicity, we expand the distance Eq. (6) up to the first order to get

$$d_{n,n-1} \approx \frac{R_0}{l_0} [(1 - \cos(\theta_0))(r_n + r_{n-1}) + \sin(\theta_0)R_0\theta_{n,n-1}] \quad (8)$$

The Hamiltonian for the twist motion is given by

$$H_{twist} = \frac{1}{2} \sum_n J_n (\dot{\theta}_{n,n-1}^2 + \Omega_\theta^2 \theta_{n,n-1}^2) \quad (9)$$

where J_n is the reduced moment of inertia.

The effect of an external electric field on the charge transfer in DNA is described by

$$H_{field} = -eE \sum_n na|c_n|^2 \quad (10)$$

where E is the electric field directed along the strands and e is the electron charge.

Realistic parameters for DNA molecules given by Barbi et al. [17] and Stryer [18] are following: $M_n = 4.982 \times 10^{-25} \text{ kg}$, $a = 3.4 \text{ \AA}$, $\theta_0 = 36^\circ$, $J = 4.982 \times 10^{-45} \text{ kgm}^2$, $\Omega_r = 6.252 \times 10^{12} \text{ s}^{-1}$, $\Omega_\theta = [0.526 - 0.744] \times 10^{12} \text{ s}^{-1}$, $V_0 = 0.1 \text{ eV}$.

Also, the strengths of interaction between the electronic and vibrational variables are $k_{AT} = 0.778917 \text{ eV/\AA}$, $k_{GC} = -0.090325 \text{ eV/\AA}$, $\alpha_{AT} = 0.053835 \text{ \AA}^{-1}$, $\alpha_{GC} = 0.383333 \text{ \AA}^{-1}$ [19] where the subscripts AT and GC denote the ones of the poly(dA)-poly(dT) polymers, respectively.

The dynamics of the N base pairs are investigated by molecular dynamics simulation using Nosé-Hoover method. The Hoover motion equations are [20,21]

$$\begin{aligned} \ddot{r}_n = & -\Omega_r^2 r_n - \frac{k}{M_n} |c_n|^2 - \frac{V_0}{M_n} \alpha \frac{R_0}{l_0} (1 - \cos(\theta_0)) \\ & \times [c_n^* c_{n-1} + c_{n-1}^* c_n + c_n^* c_{n+1} + c_{n+1}^* c_n] - \xi \dot{r}_n \end{aligned} \quad (11)$$

$$\ddot{\theta}_{n,n-1} = -\Omega_\theta^2 \theta_{n,n-1} - \frac{V_0}{J_n} \alpha \frac{R_0^2}{l_0} \sin(\theta_0) [c_n^* c_{n-1} + c_{n-1}^* c_n] \quad (12)$$

$$\begin{aligned} \dot{c}_n = & -\frac{i}{\hbar} \{ (E_n^0 + kr_n - eEna) c_n \\ & - V_0 \{ 1 - \alpha \frac{R_0}{l_0} [(1 - \cos(\theta_0))(r_n + r_{n-1}) + \sin(\theta_0)R_0\theta_{n,n-1}] \} c_{n-1} \\ & - V_0 \{ 1 - \alpha \frac{R_0}{l_0} [(1 - \cos(\theta_0))(r_{n+1} + r_n) + \sin(\theta_0)R_0\theta_{n+1,n}] \} c_{n+1} \} \end{aligned} \quad (13)$$

$$\dot{\xi} = \frac{1}{M} [\sum_n M_n \dot{r}_n^2 - N k_B T] \quad (14)$$

ξ is the thermodynamics friction coefficient which interacting with the particles in the stretching direction, T is the temperature maintained by heat bath and M is the constant of Nosé-Hoover thermostat that has been set to $M = 1000$.

2.1 Mean Lyapunove Exponent

The highly nonlinear nature of the present model implies the possibility of applying the nonlinear dynamics concepts and chaos theory. The Lyapunov exponent is one of the most popular concepts of the nonlinear dynamics which describes the growth and shrinkage rates of small perturbations in different directions of the state space. On the other hand, mean Lyapunove exponent (MLE) could characterize the chaos in the systems described by coupled maps [22].

In this work, the MLE theory is used to determine the effect of parameters on the charge transfer mechanism and stability analysis of system. Therefore, the autonomous system of first-order differential equation should be calculated as the following form:

$$\dot{r}_n = u_n \quad (15)$$

$$\begin{aligned} \dot{u}_n = & -\Omega_r^2 r_n - \frac{k}{M_n} |c_n|^2 - \frac{V_0}{M_n} \alpha \frac{R_0}{l_0} (1 - \cos(\theta_0)) \\ & \times [c_n^* c_{n-1} + c_{n-1}^* c_n + c_n^* c_{n+1} + c_{n+1}^* c_n] - \xi u_n \end{aligned} \quad (16)$$

$$\dot{\theta}_{n,n-1} = v_n \quad (17)$$

$$\dot{v}_n = -\Omega_\theta^2 \theta_{n,n-1} - \frac{V_0}{J_n} \alpha \frac{R_0^2}{l_0} \sin(\theta_0) \quad (18)$$

$$\begin{aligned} \dot{c}_n = & -\frac{i}{\hbar} \{ (E_n^0 + k r_n - e E n a) c_n \\ & - V_0 \{ 1 - \alpha \frac{R_0}{l_0} [(1 - \cos(\theta_0))(r_n + r_{n-1}) + \sin(\theta_0) R_0 \theta_{n,n-1}] \} c_{n-1} \\ & - V_0 \{ 1 - \alpha \frac{R_0}{l_0} [(1 - \cos(\theta_0))(r_{n+1} + r_n) + \sin(\theta_0) R_0 \theta_{n+1,n}] \} c_{n+1} \} \end{aligned} \quad (19)$$

$$\dot{\xi} = \frac{1}{M} [\sum_n M_n u_n^2 - N k_B T] \quad (20)$$

where u_n and v_n are the the radial and angular velocity of base pairs, respectively.

Then, we could consider the linear stability of the $5N + 1 \times 5N + 1$ Jacobian matrix written as:

$$B_{k,N} = \begin{pmatrix} R_R & R_U & R_\theta & R_V & R_C & R_\xi \\ U_R & U_U & U_\theta & U_V & U_C & U_\xi \\ \theta_R & \theta_U & \theta_\theta & \theta_V & \theta_C & \theta_\xi \\ V_R & V_U & V_\theta & V_V & V_C & V_\xi \\ C_R & C_U & C_\theta & C_V & C_C & C_\xi \\ \xi_R & \xi_U & \xi_\theta & \xi_V & \xi_C & \xi_\xi \end{pmatrix} \quad (21)$$

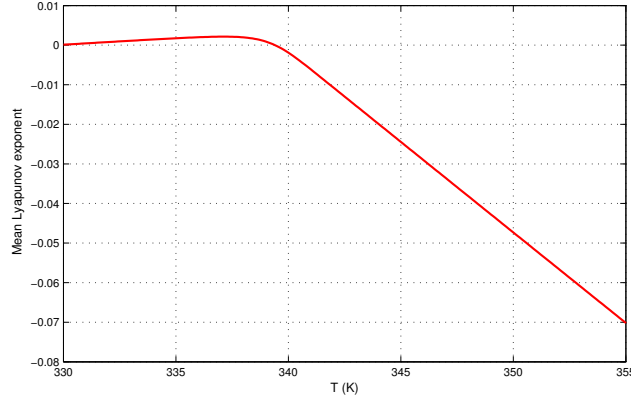


Fig. 1. Mean Lyapunov exponent with respect to the temperature ($E=0.1$ V/A).

The full matrix $B_{k,N}$ may be considered as an 6×6 matrix each element of which is itself a block R_R, R_U, \dots that are the derivatives with respect to the elements. As example, R_R could be written as

$$R_R = \begin{pmatrix} \frac{\partial r_1^{k+1}}{\partial r_1^k} & \dots & \frac{\partial r_1^{k+1}}{\partial r_N^k} \\ \vdots & \ddots & \vdots \\ \frac{\partial r_N^{k+1}}{\partial r_1^k} & \dots & \frac{\partial r_N^{k+1}}{\partial r_N^k} \end{pmatrix}_{N \times N} = I_{N \times N} \quad (22)$$

which is a $N \times N$ unit matrix.

The eigenvalues of jacobian matrix (E_i^k) give the Lyapunov exponents. The Lyapunov exponents are given by

$$\lambda_i^k = \ln |E_i^k| \quad (i = 1, \dots, 5N + 1) \quad (23)$$

where $|E_i^k|$ means the absolute value of E_i^k . Then MLE is written as

$$\lambda_k = \frac{1}{5N + 1} \sum_{i=1}^{5N+1} \lambda_i^k \quad (24)$$

The spatio-temporal pattern of system is order when the MLE is negative, the more negative the exponent, the greater the stability.

Figure 1 shows the MLE with respect to the bath temperature. It is clear that increasing the temperature corresponds to increasing of the MLE but it is different when we are getting close to the denaturation temperature. Then, it is interesting that the MLE changes its nature in about denaturation temperatures (Fig. 1). It means that the transition point in MLE versus temperature diagram could be considered as the signature of the change in DNA nature or denaturation.

On the other hand, we have examined the effect of external electrical field on the DNA charge transfer stability. Figure 2 determined the MLE behavior

in the presence of electrical field. MIE takes the small values in small field intensity and increases by increasing the field. But, there is a critical field E_c in which MLE changes its sign. It may indicate a transition point. It would determine a metal-insulator transition if we consider the zero point of Lyapunov exponent as infinite localization length. On the other hand, one the concepts

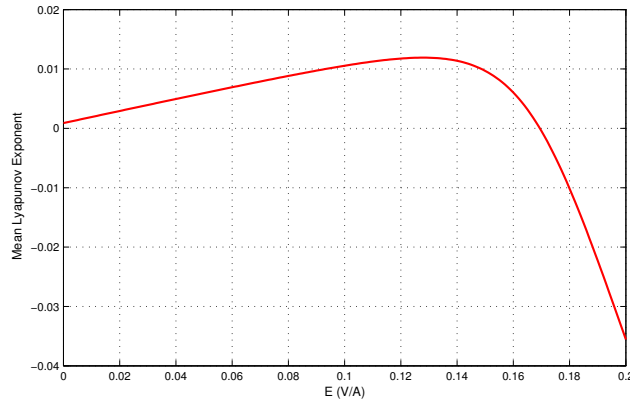


Fig. 2. Mean Lyapunov exponent with respect to the electrical field intensity (T=300 K).

that could be the interface between the chaos theory and electronic is Landauer resistance. The Landauer resistance in zero temperature is expressed as follows:

$$\rho = \frac{1 - T}{T} \quad (25)$$

in units of the quantum resistance $h/2e^2 (\simeq 13k\Omega)$ [23] and T is the transmission coefficient of the system related to Lyapunov exponent via

$$T = \exp(-2\lambda_k N) \quad (26)$$

where N is the number of base pairs in DNA lattice. The variation of Landauer resistance with respect to the electrical field in zero temperature has characterized in Fig. 3. As it is clear, Landauer resistance takes ascending behavior via the growth the electrical field intensity.

2.2 Current Operator

Electrical current flowing through DNA is another quantity to investigate the conductivity of DNA. We could use the definition of the particle density operator in Heisenberg picture:

$$n_i(t) = e^{iHt} n_i e^{-iHt} \quad (27)$$

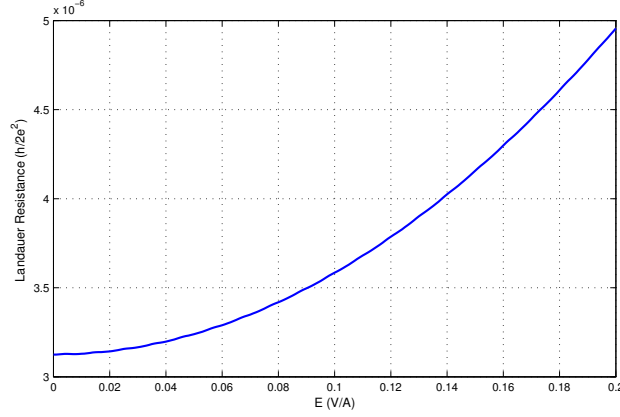


Fig. 3. Landauer resistance with respect to the electrical field intensity (T=0 K).

where $n_i = c_i^+ c_i$ is the charge density. Then, we calculate the time dependent current operator as follows:

$$I(t) = \frac{d(en_i(t))}{dt} = \frac{ie}{\hbar} \sum_n V_{n,n-1} (c_n^* c_{n-1} - c_{n-1}^* c_n). \quad (28)$$

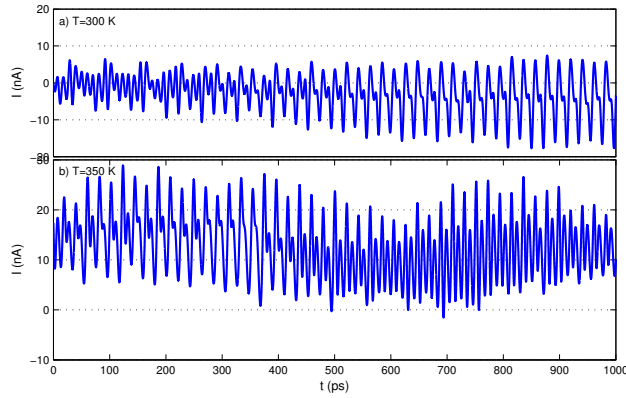


Fig. 4. The electrical current time series in a) room temperature b) threshold of denaturation temperature.

According to the obtained relation, the electrical current is dependent on the relative position of the base pairs and probability amplitude for the charge carriers in every time. So, the electrical current shows the oscillatory behavior over the time and oscillates with the irregular periods (Fig. 4). For studying the temperature effect on flowing current through DNA, specially denaturation

temperature, we have obtained the current time series in two temperatures: a) room temperatures, b) threshold of denaturation temperature. In both them, the current shows the similar behavior but the current amplitude increases in $T = 350\text{ K}$.

2.3 I-V Characteristic diagram

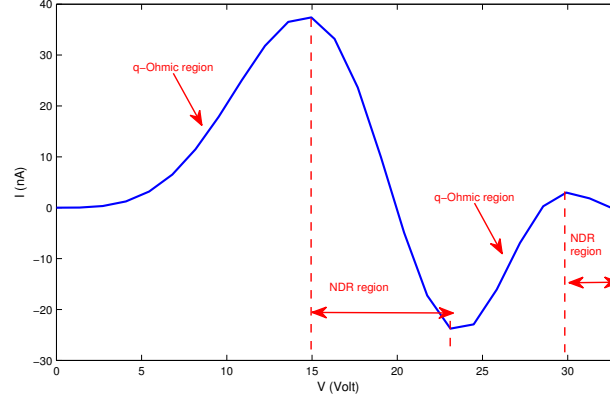


Fig. 5. I-V characteristic diagram ($T=300\text{ K}$).

Measurements of electrical current as a function of the potential applied across single DNA could indicate metallic-like behaviors and efficient conduction and conversely insulator-like behaviors [24]. For a more detailed study of DNA conductivity, we could investigate the current-voltage characteristic of DNA in the present model, (see Fig. 5). The obtained results based on I-V characteristic diagram characterizes the regions with quasi-linear behavior together with negative slope properties (Fig. 5). It is worth mentioning that the quasi-linear behavior could indicate the quasi-Ohmic properties that represents deviation from linear behavior. On the other hand, negative slope properties could express the negative differential resistance (NDR) phenomenon. It could be said when the voltage continuously increases, the current through DNA increases at the beginning and then decreases, resulting in a negative differential resistance (NDR) peak. In electronic, negative differential resistance devices are used to make bistable switching circuits and electronic oscillators [25]. Also, it opens the possibility to develop molecular electronic switches and memory devices [26]. Figure 6 exhibits a three-dimensional schema of I-V characteristic at different times. It is clear that the general shape of electrical current with respect to the applied potential do not change in time.

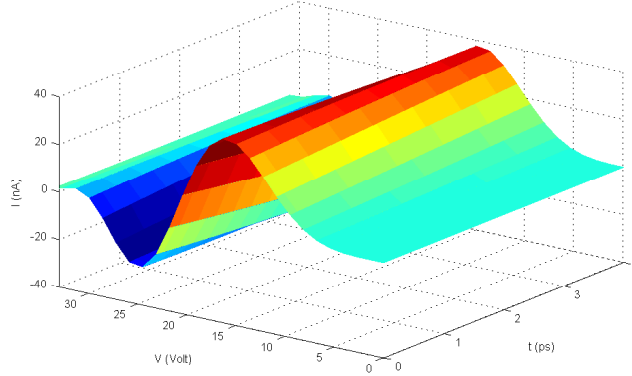


Fig. 6. 3-D current-voltage diagram over the time ($T=300 \text{ K}$).

3 Conclusion

We have studied the charge transfer mechanism in DNA molecule in a cylindrical reference system. Using the MLE theory, we could determine the ranges in applied electrical field and temperature parameter in which DNA shows the stable behavior. On the other hand, we have indicated the critical points in parameter regions that changes the nature of DNA. Also, we could obtained the electrical current operator directly from the evolution equations of system. The study of the current time series expresses its unstable behavior over the time. For a more detailed study of DNA conductivity, we have investigated the current-voltage characteristic of DNA. The I-V diagram represent regions with q-Ohmic behavior together with NDR phenomenon. NDR behavior has been observed in DNA, experimentally. NDR devices are used to make bistable switching circuits and electronic oscillators.

References

1. D. Porath, G. Cuniberti and R. Di Felice. *Topics in Current Chemistry*, 237, 183,2004.
2. H. Yan, S. H. Park, G. Finkelstein, J. H. Reif and T. H. LaBean. *Science*, 301, 1882, 2003.
3. V. D. Lakhno. *Int. J. Quant. Chem.* 108, 1970, 2008.
4. A. Offenhussner and R. Rinald (Eds.) *Nanobioelectronics for Electronics, Biology and Medicine*, Springer, New York, 2009.
5. M. W. Shinwari, M. J. Deen, E. B. Starikov and G. Cuniberti, *Adv. Funct. Mater.*, 20, 1865, 2010.
6. G. B. Schuster (Ed.), *Long-Range Charge Transfer in DNA*, Springer, Heidelberg, 2004.
7. P.J. De Pablo, F. Moreno-Herrero, J. Colchero, J. Gomez Herrero, P. Herrero, A.M. Bar, P.N. Ordej, J.M. Soler and E. Artacho. *Phys. Rev. Lett.*, 85, 49924995, 2000.
8. K.-H. Yoo, D.H. Ha, J.-O. Lee, J.W. Park, J. Kim, J.J. Kim, H.-Y. Lee, T. Kawai and H.Y. Choi. *Phys. Rev. Lett.*, 87, 198102, 2001.

9. A.Yu. Kasumov, M. Kociak, S. Guron, B. Reulet, V.T. Volkov, D.V. Klinov and H. Bouchiat. *Science*, 291, 5502, 280282, 2001.
10. A.J. Storm, J. van Noort, S. de Vries and C. Dekker. *Appl. Phys. Lett.*, 79, 3881, 2001.
11. Z. Hermon, S. Caspi and E. Ben-Jacob. *Europhys. Lett.*, 43, 482, 1998.
12. J. P. Lewis, T. E. Cheatham, E. B. Starikov, H.Wang and O. F. Sankey. *J. Chem. B*, 107, 2581, 2003.
13. M. Barbi, S. Cocco and M. Peyrard. *Phys. Lett. A*, 253, 358, 1999.
14. I. A. Goychuk, E. G. Petrov and V. May. *J. Chem. Phys.* 106, 4522, 1997.
15. F. Palmero, J. F. R. Archilla, D. Hennig and F. R. Romero. *New J. Phys.*, 6, 13, 2004.
16. A. Dang Koko, C. B. Tabi, H. P. Ekobena Fouda, A. Mohamadou and T. C. Kofané. *Chaos* 22, 043110, 2012.
17. M. Barbi, S. Cocco and M. Peyrard. *Phys. Lett. A*, 253, 358, 1999.
18. L. Stryer. *Biochemistry*, Freeman, New York, 1995.
19. H. Yamada and K. Iguchi. *Hindawi Publishing Corporation, Advances in Condensed Matter Physics*, 380710, 2010.
20. T. Dauxois, M. Peyrard and A.R. Bishop. *Phys. Rev. E* 47, 684, 1993.
21. T. Lipniacki. *Phys. Rev. E*, 64, 051919/1, 2001.
22. H. Shibata. *Physica A*, 264, 266, 1999.
23. L. M. Lifshits, S. A. Gredeskul and L. A. Pastur. *Introduction to the Theory of Disordered Systems*, Wiley, New York, 1988.
24. L. M. Bezerril, D. A. Moreiraa, E. L. Albuquerque, U. L. Fulcob, E. L. de Oliveira and J. S. de Sousa. *Phys. Lett. A*, 373, 3381, 2009.
25. T. C. L. G. Sollner, W. D. Goodhue, P. E. Tannenwald, C. D. Parker and D. D. Peck. *Appl. Phys. Lett.*, 43, 588, 1983.
26. J. Chen, M. A. Reed, A. M. Rawlett and J. M. Tour. *Science*, 286, 1550, 1999.

A New Dynamical Control Scheme to Control of Abnormal Synthetic ECG Signals

S. Behnia and J. Ziaei

Department of Physics, Urmia University of Technology, Urmia, Iran
(E-mail: s.behnia@sci.uut.ac.ir)

Abstract. Spurious coupling between pacemaker components may turn normal ECG signals into chaotic ones. Present study introduces a new chaos control approach known as dynamical control to retain normal signals. To this end, phase space diagram method is used for comparing between before and after of control. The obtained results confirm that the proposed method is effective in enforcing the heart to re-assume a limit cycle.

Keywords: Chaos, Dynamical Feedback Control, Electrocardiogram (ECG).

1 Introduction

The study of cardiac system dynamics within the framework of Chaos Theory has found significant progress in developing new methods to overcome the real-world challenges of heart failure [1–5]. The interest of the approach lies in the fact that the electrical behavior of the heart may be chaotic due to the abnormal functioning of cardiac pacemakers [3,6]. On the other hand, the regularity of cardiac signals as a result of normal functioning of the cardiac pacemakers [3,7] demands new approaches to enforce the heart to reassume a stable limit cycle.

The stabilization of unstable desired orbits can be performed by various methods such as discrete OGY method [8], time-delayed feedback approach (TDF) [9] and extended time-delayed feedback (ETDF) control technique [10]. However, observer dependence is one of the main challenges of methods mentioned in feasible implementations. So, present study introduces *dynamical control* as a new control scheme for stabilization of cardiac signals [11].

Here, a system of three coupled modified delayed van der Pol oscillators [14] is used as a mathematical model to describe heart rhythms dynamics. The dynamical structure of the model is investigated through phase space diagrams and then based on dynamical control approach a controller is proposed for controlling chaos in the system.

The rest of the paper was organized as follows. In Sect. 2 the mathematical model used in this study is described. The proposed dynamical control approach and one-parameter families of chaotic maps which are cornerstone

8th CHAOS Conference Proceedings, 26-29 May 2015, Henri Poincaré Institute, Paris France



of the proposed dynamical control method are explained in Sect. 3. Results are discussed in Sect. 4. Finally, summary and outline are presented in Sect. 5. Furthermore, Sect. A includes a brief introduction on the heart and its electrical activity.

2 Model Description

The model used here for simulating ECG signals is an extending of the model proposed in Ref. [13]. First, each of the natural pacemakers of the cardiac system (AV node, His-Purkinje fibers and SA node) is modeled by a unique modified delayed van der Pol oscillator. Then, by suitable coupling of them, dynamical behavior of an electrocardiogram signal is simulated. Electrocardiogram is a procedure for quantifying the electrical potential and so the electrical activity of the heart and ECG recording is one of the simple clinical approaches for investigation of the heart health and its proper functioning [15].

The proposed model is as follow [14]

$$\begin{cases} \dot{x}_1 = x_2, \\ \dot{x}_2 = -a_{SA}x_2(x_1 - w_{SA_1})(x_1 - w_{SA_2}) - x_1(x_1 + d_{SA})(x_1 + e_{SA}) \\ \quad + k_{SA-AV}(x_1 - x_3^{\tau_{SA-AV}}) + k_{SA-HP}(x_1 - x_5^{\tau_{SA-HP}}), \\ \dot{x}_3 = x_4, \\ \dot{x}_4 = -a_{AV}x_4(x_3 - w_{AV_1})(x_3 - w_{AV_2}) - x_3(x_3 + d_{AV})(x_3 + e_{AV}) \\ \quad + k_{AV-SA}(x_3 - x_1^{\tau_{AV-SA}}) + k_{AV-HP}(x_3 - x_5^{\tau_{AV-HP}}), \\ \dot{x}_5 = x_6, \\ \dot{x}_6 = -a_{HP}x_6(x_5 - w_{HP_1})(x_5 - w_{HP_2}) - x_5(x_5 + d_{HP})(x_5 + e_{HP}) \\ \quad + k_{HP-SA}(x_5 - x_1^{\tau_{HP-SA}}) + k_{HP-AV}(x_5 - x_3^{\tau_{HP-AV}}). \end{cases} \quad (1)$$

where $x_i^\tau = x_i(t - \tau)$, $i = 1, \dots, 6$, τ represents time delay and k_o symbolizes coupling terms. Then, the ECG signal is built from the composition of these signals as follows:

$$ECG = \alpha_0 + \alpha_1 x_1 + \alpha_3 x_3 + \alpha_5 x_5. \quad (2)$$

In present study, k_{SA-AV} was taken as a control parameter. The remaining parameters were fixed at the values suggested by the original paper [14] as $a_{SA} = 3$, $a_{AV} = 3$, $a_{HP} = 5$, $w_{SA_1} = 0.2$, $w_{SA_2} = -1.9$, $w_{AV_1} = 0.1$, $w_{AV_2} = -0.1$, $w_{HP_1} = 1$, $w_{HP_2} = -1$, $d_{SA} = 3$, $d_{AV} = 3$, $d_{HP} = 3$, $e_{SA} = 4.9$, $e_{AV} = 3$, $e_{HP} = 7$, $k_{SA-AV} = 5$, $k_{AV-HP} = 20$, $\alpha_0 = 1$, $\alpha_1 = 0.1$, $\alpha_3 = 0.05$, $\alpha_5 = 0.4$, $\tau_{SA-AV} = 0.8$, $\tau_{AV-HP} = 0.1$ and all other parameters vanish.

3 Control Scheme

Our idea for control is based on the fact that the control parameter can be a variable in time through a chaotic map. In this section, first we try to explain mathematical description of the chaotic map which we used in this paper. Then, we expand our idea of control.

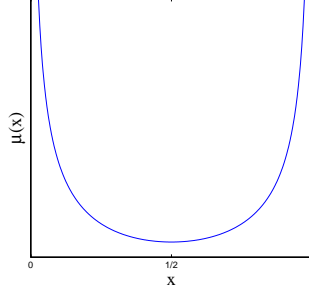


Fig. 1. Invariant measure of Logistic map.

3.1 One-parameter families of chaotic maps

The Logistic map is one of the most familiar maps in unit interval which serves as a prototype of chaos in classical nonlinear maps. One of the exciting features of the Logistic map is that it has an invariant measure which provides frequency of visits to any given interval in $[0, 1]$.

$$\mu(x) = \frac{1}{\pi \sqrt{x(1-x)}}. \quad (3)$$

This density function is graphed in Fig. 1 and ensures the ergodicity of the Logistic map.

In previous work [16] we generalized the Logistic map to a Hierarchy of one parameter families of maps with some special properties in unit interval $[0, 1]$:

- They map the interval $[0, 1]$ into itself,
- They have $(N - 1)$ critical points,
- They have $(N - 1)$ real roots,
- They have at most $(N + 1)$ attracting periodic orbits [18].

The mathematical form of the proposed Hierarchy one parameter families of maps is as follows

$$\Phi_N(k, \alpha) = \frac{\alpha^2 (T_N(\sqrt{k}))^2}{1 + (\alpha^2 - 1)(T_N(\sqrt{k}))^2}. \quad (4)$$

where $N > 1$ is an integer and T_N s are Chebyshev polynomials of type 1 [17]. Invariant measure of the $\Phi_N(k, \alpha)$ is defined as follows

$$\mu(k, \beta) = \frac{1}{\pi} \frac{\sqrt{\beta}}{\sqrt{k(1-k)}(\beta + (1-\beta)k)}. \quad (5)$$

provided that $\beta > 0$ and

$$\left\{ \begin{array}{ll} \alpha = \frac{\sum_{k=0}^{\lfloor \frac{(N-1)}{2} \rfloor} C_{2k+1}^N \beta^{-k}}{\sum_{k=0}^{\lfloor \frac{N}{2} \rfloor} C_{2k}^N \beta^{-k}} & \text{N: odd,} \\ \alpha = \frac{\beta \sum_{k=0}^{\lfloor \frac{(N)}{2} \rfloor} C_{2k}^N \beta^{-k}}{\sum_{k=0}^{\lfloor \frac{(N-1)}{2} \rfloor} C_{2k+1}^N \beta^{-k}} & \text{N: even.} \end{array} \right. \quad (6)$$

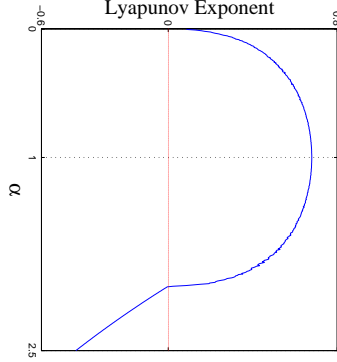


Fig. 2. Illustration of the effect of the α variation on the Lyapunov exponent of the Eq. 10. The positive value of the Lyapunov exponent proves the chaotic nature of the generalized Logistic map (Eq. 10). Furthermore, the maximum value of the Lyapunov exponent is occurred at $\alpha = 1$ which was used to generate dynamical map (Eq. 11) for control of chaos.

As an example

$$\Phi_2(k, \alpha) = \frac{\alpha^2(2k-1)^2}{4k(1-k) + \alpha^2(2k-1)^2}, \quad \alpha = \frac{2\beta}{(1+\beta)}. \quad (7)$$

By the aid of the invertible map $h(k) = \frac{1-k}{k}$ which maps $[0, 1]$ into $[0, \infty)$ one can transform $\Phi_N(k, \alpha)$ into $\Psi_N(k, \alpha)$ as

$$\Psi_N(k, \alpha) = h \circ \Phi_N(k, \alpha) \circ h^{(-1)} = \frac{1}{\alpha^2} \tan^2 (N \arctan \sqrt{k_m}) \quad (8)$$

which in terms of k_{m+1} can be written as

$$k_{m+1} \equiv \Psi_2(k, \alpha) = \frac{1}{\alpha^2} \tan^2 (2 \arctan \sqrt{k_m}) = \frac{4}{\alpha^2} \frac{\tan^2 (\arctan \sqrt{k_m})}{(1 - \tan^2 (\arctan \sqrt{k_m}))^2}. \quad (9)$$

Finally, it can be simplified as

$$k_{m+1} = \frac{4k_m}{\alpha^2(1-k_m)^2}. \quad (10)$$

The Lyapunov exponent diagram for this map is shown in Fig. 2. Obviously, maximum value has been reached at $\alpha = 1$. So, in the following we set $\alpha = 1$. $\Phi_2(k)$ and $\Psi_2(k)$ for $\alpha = 1$ are shown in Fig. 3 and Fig. 4, respectively.

3.2 Controlling Procedure

The observer dependence of previous methods [8–10] for control of chaos is a high risk for heart health. Our previous work [11] allows one to overcome

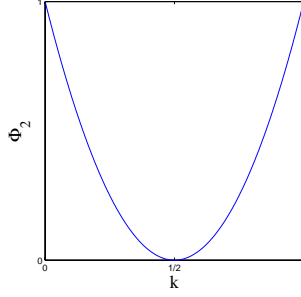


Fig. 3. Illustration of the $\Phi_2(k)$ for $\alpha = 1$.

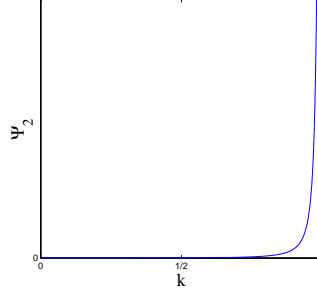


Fig. 4. Illustration of the $\Psi_2(k)$ for $\alpha = 1$.

the risk. Flexibility and observer independence are the main features of the method. The proposed method is based on the fact that the control parameter as a variable in time is changeable by another chaotic map. We improve the method by considering the hierarchy of one parameter families of ergodic solvable chaotic maps with invariant measure [16]. So, the behavior of original system may be replaced by

$$\begin{cases} \dot{\mathbf{x}} = \mathbf{F}(\mathbf{x}, k_m), \\ k_{m+1} = \frac{4k_m}{(1-k_m)^2}. \end{cases} \quad (11)$$

where $\mathbf{x} \in \mathbb{R}^n$, $k \in \mathbb{R}^1$ denotes k_{HP-SA} and \mathbf{F} is the dynamical model (Eq. 1).

4 Results and Discussion

4.1 Introducing the dynamics of the master ECG

Fig. 5 depicts the phase space of the system under different situations. $k_{SA-AV} = 6.42$, $k_{SA-AV} = 7.57$, $k_{SA-AV} = 7.64$ and $k_{SA-AV} = 10$ have been chosen as samples to reveal diverse configurations. As is evident, the system includes a wide range of behaviors. Due to the variation of k_{SA-AV} its response may

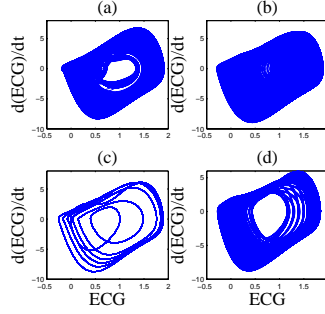


Fig. 5. Phase space of ECG without applying the control process. (a) $k_{SA-AV} = 6.42$, (b) $k_{SA-AV} = 7.57$, (c) $k_{SA-AV} = 7.64$, (d) $k_{SA-AV} = 10$. (a), (b) and (d) demonstrate non-periodic and unstable responses, and (c) represents periodic and stable response.

be periodic and stable (see Fig. 5(c)) or non-periodic and unstable (see Fig. 5(a)-(b)-(d)).

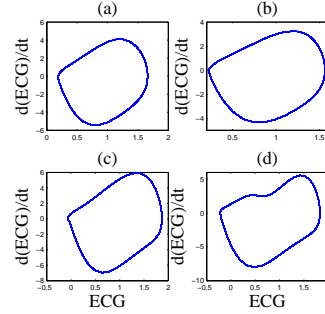


Fig. 6. Phase space of ECG after applying the control process. (a) $k_{SA-AV} = 6.42$, (b) $k_{SA-AV} = 7.57$, (c) $k_{SA-AV} = 7.64$, (d) $k_{SA-AV} = 10$. In comparison with Fig. 5 it is seen that all of the responses have suppressed to 2-period orbits.

4.2 Applying the chaos control method

The results of control method have been shown in Fig. 6. In order to reveal the control method efficiency, $k_{SA-AV} = 6.42$, $k_{SA-AV} = 7.57$, $k_{SA-AV} = 7.64$ and $k_{SA-AV} = 10$ were chosen as samples to be subjected to the control method. Pertinent phase spaces have been plotted in Fig. 6. Obviously, the chaotic motion has suppressed to a 2-period orbit. The results have confirmed the efficiency of proposed control method.

5 Summary

The development of control methods that accurately modulate the undesirable behavior of cardiac system is a fast growing research in interdisciplinary sciences. In present study based on phase space diagrams, nonlinear behavior and the unstable signals suppression problem were studied in an electrocardiogram model. Here, based on one-parameter families of chaotic maps a new controller was introduced for controlling chaos. Moreover, it was shown that the proposed technique can modulate underlying dynamics.

A Heart and Electrical Activity

The heart is a four-chambered organ which pumping blood for circulation is its basic function. The heart is divided into right and left parts, each part with its own atrium and ventricle. Receiving deoxygenated blood from the rest of the body and propelling oxygenated received blood from lungs to other organs of the body are fulfilled through the coordinate contractions of the heart organs. For contractions to be occurred, the conducting cells of heart must be excited by impulses initiated at a network of pacemaker cells. There are three types of pacemaking cells.

- The sinoatrial (SA) node which contains main pacemaking cells.
- The atrioventricular (AV) node which serves as a pacemaker should the SA node fail.
- The bundle of His-Purkinje (HP) fibers, responsible for contracting the ventricles, which may initiate impulses at low rates compared to the SA and AV nodes [15].

In resting state cardiac cells are polarized electrically, i.e., the outside of the cell membrane has a positive charge and the inside of the cell has a negative charge instead. Depolarization is the fundamental electrical event of the heart within it positive ions flow across the cell membrane into the cell and negative ions to the outside of the cell membrane. Through a process namely repolarization, polarity returns and the relaxation or resting state occurs. The waves of depolarization and repolarization represent electrical activity of the heart known as ECG [15]. A schematic illustration of the heart organ has been shown in Fig. 7.

References

1. Z. Qu, Chaos in the genesis and maintenance of cardiac arrhythmias, *Prog. Biophys. Mol. Biol.* 105 (3) (2011) 247.
2. S. Behnia, A. Akhshani, H. Mahmodi, H. Hobbenagi, On the calculation of chaotic features for nonlinear time series, *Chin. J. Phys.* 46 (4) (2008) 394.
3. S. Behnia, J. Ziaei, M. Ghiassi, A new approach to the study of heartbeat dynamics based on mathematical model, in: *Electrical Engineering (ICEE), 2013 21st Iranian Conference on, IEEE, (2013), 1.*

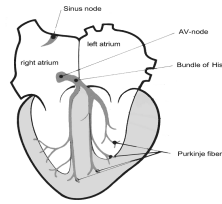


Fig. 7. Schematic picture of the heart. The heart is a four-chambered organ which is divided into right and left parts, each part with its own atrium and ventricle. For contractions to be occurred, the conducting cells of heart must be excited by impulses initiated at a network of pacemaker cells. There are three types of pacemaking cells. The sinoatrial (SA) node which contains main pacemaking cells, the atrioventricular (AV) node which serves as a pacemaker when the SA node fails and the bundle of His-Purkinje (HP) fibers (responsible for contracting the ventricles), may initiate impulses at low rates compared to the SA and AV nodes [15].

4. R. B. Govindan, A. N. Massaro, N. Niforatos, A. Du Plessis, Mitigating the effect of non-stationarity in spectral analysis an application to neonate heart rate analysis, *Comput. Biol. Med.* 43 (12) (2013) 2001.
5. R. J. Martis, U. R. Acharya, H. Adeli, Current methods in electrocardiogram characterization, *Comput. Biol. Med.* 48 (2014) 133.
6. B. B. Ferreira, A. S. de Paula, M. A. Savi, Chaos control applied to heart rhythm dynamics, *Chaos, Solitons Fractals* 44 (2011) 587.
7. R. T. Baillie, A. A. Cecen, C. Erkal, Normal heartbeat series are nonchaotic, nonlinear, and multifractal: New evidence from semiparametric and parametric tests, *Chaos* 19 (2) (2009) 028503.
8. E. Ott, C. Grebogi, J. A. Yorke, Controlling chaos, *Phys. Rev. Lett.* 64 (11) (1990) 1196.
9. K. Pyragas, Continuous control of chaos by self-controlling feedback, *Phys. Lett. A* 170 (6) (1992) 421.
10. K. Pyragas, Delayed feedback control of chaos, *Philos. Trans. R. Soc. London, Ser. A* 364 (1846) (2006) 2309.
11. S. Behnia, A. Akhshani, Dynamical control of chaos by slavemaster feedback, *Chaos, Solitons Fractals* 42 (4) (2009) 2105.
12. A. M. dos Santos, S. R. Lopes, R. L. R. L. Viana, Rhythm synchronization and chaotic modulation of coupled van der pol oscillators in a model for the heartbeat, *Physica A* 338 (34) (2004) 335.
13. K. Grudziński, J. J. Żebrowski, Modeling cardiac pacemakers with relaxation oscillators, *Physica A* 336 (1–2) (2004) 153.
14. S. R. Gois, M. A. Savi, An analysis of heart rhythm dynamics using a three-coupled oscillator model, *Chaos, Solitons Fractals* 41 (5) (2009) 2553.
15. K. Brisendine, *Multiskilling: Electrocardiography for the Health Care Provider*, Delmar Publishers, 1998.
16. M. Jafarizadeh, S. Behnia, S. Khorram, H. Nagshara, Hierarchy of chaotic maps with an invariant measure, *J. Stat. Phys.* 104 (5-6) (2001) 1013.
17. Z. Wang, D. Guo, *Special functions*, New York, 1989.
18. R. L. Devaney, L. Devaney, *An introduction to chaotic dynamical systems*, Vol. 6, Addison-Wesley Reading, 1989.

Periodic solutions, indeterminacy and chaotic dynamics in a model of sustainable tourism^{*}

Giovanni Bella[†]

Abstract

The impact of tourism on economic growth and environmental degradation is one of the most relevant debated issues. Despite the huge strand of empirical literature on the topic, a formalized theoretical investigation of the link between tourism and sustainable economic growth is unfortunately still lacking.

To this end, and in line with the literature on the tourist life-cycle hypothesis, we present an edogenous growth model to study the impact of tourism activities and natural resource use on the long run steady state. The aim is to use the principles of bifurcation theory to gain hints on the global properties of the equilibrium, and show the existence of irregular patterns, either indeterminate or chaotic, which possibly suggest the emergence of a (low growth) poverty-environment trapping region.

Keywords: Sustainable tourism; Indeterminacy; Chaotic dynamics; Poverty trap.

JEL Classification: C61, L83, Q01

^{*}I would like to thank professors and colleagues of my department at the University of Cagliari for their support and discussions we had on the issues regarding environmental economics. Obviously, I take responsibility for all errors.

[†]Address for correspondence: Department of Economics and Business, University of Cagliari, Viale Sant'Ignazio, 17 - 09123 Cagliari (Italy). E-mail: bella@unica.it. Tel. +390706753340.



1 Introduction

Tourism economics is characterized by an explosive growing interest. Unfortunately, formalized theoretical studies are still lacking in this field to explore the complex relationship existing between tourism and a sustainable economic growth (see, Sachs and Warner, 2001).

Nowadays economies basically share the common view that productions of goods and services, especially for firms operating in the tourist sector, highly depend on natural resource overuse, and no growth is therefore possible without this input. Therefore, trying to understand the way an economy can grow along an optimal equilibrium path, without sacrificing the available natural resources, is one of the most debated and intriguing social claims, and is in line with the so-called tourism-led-growth hypothesis (Brau et al., 2007; Nowak et al., 2007; Baggio, 2008; Brida et al., 2008; Katircioglu, 2009; Bornhost et al., 2010; Schubert et al., 2010).

Interestingly, once natural resource exploitation is taken into account, attention can be immediately devoted to understand whether tourism might affect the long run dynamics towards a stable equilibrium, or if undesired indeterminacy problems may eventually arise. Moreover, the rise of indeterminacy in presence of an overuse of natural resources could be the major cause for the emergence of a vicious poverty-environment trap, where public policies might not be able to avoid a non sustainable use of natural resources (see, for example, Finco, 2009).

A wide strand of literature has focused on the conditions for the emergence of multiple equilibrium trajectories in the vicinity of the steady state, but only very few attempts have been made to study the conditions for *global* indeterminacy and possible chaotic solutions to occur outside such small neighborhood of the steady state, so that the perfect foresight equilibrium may not be unique. In this case, despite the initial conditions or other economic fundamentals, the agents' decisions could locate the economy in a path which is not corresponding to the lowest exploitation level of natural resources (see, for example, Mattana and Venturi, 1999; Benhabib et al., 2001; Bella and Mattana, 2014).

In line with this strand of literature, we propose an endogenous growth model to study the impact of tourism activities and natural resource use on the long run steady state. The aim is to use the principles of bifurcation theory to gain hints on the global properties of the equilibrium, and show the existence of irregular patterns due to a sensitive dependence of our economy on the initial conditions. In particular, we study the presence of closed orbits, to detect the rise of economic fluctuations and periodic



solutions around the steady state, which are empirically confirmed by the literature on the tourist life-cycle hypothesis (Butler, 1980). The problem is to understand the conditions under which these orbits are attracting, with equilibrium trajectories being “captured” by the orbit itself, that finally becomes a (indeterminate or maybe chaotic) limit set, which possibly suggests the emergence of a (low growth) poverty-environment trapping region.

The rest of the paper is organized as follows. In section 2, we present the model, derive the steady state conditions, and study the local dynamics. In section 3, we characterize the parametric space where periodic solutions emerge, and the equilibrium becomes indeterminate, and use the Andronov-Hopf bifurcation theorem to study the global properties of the steady state. Conditions for chaotic dynamics are also derived. A final section concludes, and a subsequent Appendix provides all the necessary proofs.

2 The Model

We consider an optimal control problem where a representative agents aims at maximizing the lifetime utility, U , subject to the constraints on the accumulation of both physical capital, k , and the stock of available natural resources, E , given their positive initial values $k(0) = k_0 > 0$ and $E(0) = E_0 > 0$.

Let assume a standard *CES* utility function, i.e. $U = \frac{c^{1-\sigma}-1}{1-\sigma}$, where c is per capita consumption, and σ is the inverse of the intertemporal elasticity of substitution. Assume also that the level of investment in physical capital is given by the usual functional form $\dot{k} = y - c$, where output y is produced according to the function

$$y = Ak^\alpha Q^{1-\alpha} \quad (1)$$

where $\alpha \in [0, 1]$ is the share of physical capital, A measures the stock of existing technology, with physical capital, k , entering as an input along with the total amount of tourism services, Q . The latter is additionally specified, as depending on the amount of public spending used to promote the tourism sector, g , and the available amount of natural resources, E , in a Cobb-Douglas evolutionary law

$$Q = g^\beta E^{1-\beta} \quad (2)$$

being β a standard elasticity parameter (see Brida and Pulina, 2010).

Additionally, we set the dynamic evolution of the environmental sector as represented by $\dot{E} = N(E) - Z(Q)$, which is negatively affected by the



extractive use of natural resources employed in the production of tourism services, Z , whereas $N(E)$ determines the speed at which nature regenerates. To simplify the analysis, we propose a linear representation of these functions, namely: $N(E) = \delta E$ and $Z(Q) = \theta Q$, where δ and θ denote constant parameters of scale (see also, Musu, 1995; Rosendahl, 1996; Cole, 2009).

Hence, under a constant time preference rate, ρ , the maximization problem explicitly becomes

$$\begin{aligned} & \underset{c(t)}{Max} \int_0^\infty \frac{c^{1-\sigma} - 1}{1 - \sigma} e^{-\rho t} dt & (\mathcal{P}) \\ & s.t. \\ & \dot{k} = Ak^\alpha Q^{1-\alpha} - c \\ & \dot{E} = \delta(E - g^\beta E^{1-\beta}) \end{aligned}$$

with an associated current value Hamiltonian given by

$$H_C = \frac{c^{1-\sigma} - 1}{1 - \sigma} + \lambda \left[Ak^\alpha g^{\beta(1-\alpha)} E^{(1-\beta)(1-\alpha)} - c \right] + \mu \delta(E - g^\beta E^{1-\beta})$$

where λ and μ represent the shadow prices of physical capital and natural resources, respectively.

Solution to this optimal control problem implies the following first order necessary conditions:

$$c^{-\sigma} = \lambda \quad (3.1)$$

$$\lambda(1 - \alpha)Ak^\alpha = \mu \delta g^{\beta\alpha} E^{(1-\beta)\alpha} \quad (3.2)$$

accompanied by the equation of motion for each costate variable, that can be derived with a bit of mathematical manipulation as

$$\frac{\dot{\lambda}}{\lambda} = \rho - \alpha Ak^{\alpha-1} g^{\beta(1-\alpha)} E^{(1-\beta)(1-\alpha)} \quad (4.1)$$

$$\frac{\dot{\mu}}{\mu} = \rho - (1 - \beta) \frac{\lambda}{\mu} (1 - \alpha) Ak^\alpha g^{\beta(1-\alpha)} E^{(1-\beta)(1-\alpha)-1} - \delta \left[1 - (1 - \beta) g^\beta E^{-\beta} \right] \quad (4.2)$$

and the transversality condition

$$\lim_{t \rightarrow \infty} e^{-\rho t} [\lambda_t k_t + \mu_t E_t] = 0 \quad (5)$$

that jointly constitute the canonical system. Since both Arrow's sufficiency theorem and the transversality condition hold, the problem is therefore bounded and concave.



2.1 The reduced model

The standard procedure is conducted in this section to study the transitional dynamics of Problem \mathcal{P} .

Proposition 1 *The maximum principle associated with the decentralized optimization problem \mathcal{P} implies the following four-dimensional system of first order differential equations*

$$\begin{aligned}\frac{\dot{k}}{k} &= Ak^{\alpha-1}g^{\beta(1-\alpha)}E^{(1-\beta)(1-\alpha)} - \frac{c}{k} \\ \frac{\dot{E}}{E} &= \delta - \theta g^{\beta}E^{-\beta} \\ \frac{\dot{c}}{c} &= -\frac{\rho}{\sigma} + \frac{\alpha}{\sigma}Ak^{\alpha-1}g^{\beta(1-\alpha)}E^{(1-\beta)(1-\alpha)} \\ \frac{\dot{g}}{g} &= -\frac{x}{\beta} + \frac{\delta(1-\alpha+\alpha\beta)}{\beta\alpha} + \frac{\delta}{\beta}(1-\beta)g^{\beta}E^{-\beta}\end{aligned}\tag{S}$$

Proof. See the Appendix A. ■

Lemma 1 *System S can be easily reduced to*

$$\begin{aligned}\dot{x} &= \left\{ -\frac{\rho}{\sigma} + \left(\frac{\alpha-\sigma}{\sigma} \right) Aq^{\alpha-1}z^{(1-\alpha)} + x \right\} x \\ \dot{q} &= \left\{ -\delta + Aq^{\alpha-1}z^{(1-\alpha)} - x + \theta z \right\} q \\ \dot{z} &= \left\{ \frac{\delta(1-\alpha)}{\alpha} - x + \theta z \right\} z\end{aligned}\tag{R}$$

by means of the convenient variable substitutions: $x = \frac{c}{k}$, $q = \frac{k}{E}$, and $z = \left(\frac{g}{E} \right)^{\beta}$.

Proof. See the Appendix A. ■

Remark 1 *The steady state is a triplet (x^*, q^*, z^*) which solves the reduced system R*

$$x^* = \frac{\delta(\sigma - \alpha) + \alpha\rho}{\alpha\sigma}\tag{6.1}$$

$$Aq^{*(\alpha-1)}z^{*(1-\alpha)} = \frac{\delta}{\alpha}\tag{6.2}$$

$$z^* = \frac{\rho - \delta(1-\sigma)}{\theta\sigma}\tag{6.3}$$



Since the Jacobian matrix associated with (R) is

$$\mathbf{J} = \begin{bmatrix} x^* & \frac{\delta(\alpha-1)}{\alpha} \left(\frac{\alpha-\sigma}{\sigma} \right) \frac{x^*}{q^*} & \frac{\delta(1-\alpha)}{\alpha} \left(\frac{\alpha-\sigma}{\sigma} \right) \frac{x^*}{z^*} \\ q^* & \frac{\delta}{\alpha} (\alpha-1) & \theta q^* + \frac{\delta(1-\alpha)}{\alpha} \frac{q^*}{z^*} \\ -z^* & 0 & \theta z^* \end{bmatrix}$$

let

$$\det(\lambda \mathbf{I} - \mathbf{J}) = \lambda^3 - \text{tr}(\mathbf{J})\lambda^2 + B(\mathbf{J})\lambda - \text{Det}(\mathbf{J})$$

be the characteristic polynomial of \mathbf{J} , where \mathbf{I} is the identity matrix and $\text{tr}(\mathbf{J})$, $B(\mathbf{J})$, and $\text{Det}(\mathbf{J})$, are Trace, Sum of Principal Minors of order two, and Determinant associated with \mathbf{J} , respectively. Algebraic computation gives

$$\text{tr}(\mathbf{J}) = 2\theta z^* \quad (7.1)$$

$$\text{Det}(\mathbf{J}) = \frac{\delta\theta(1-\alpha)(2\alpha-3\sigma)}{\alpha\sigma} x^* z^* \quad (7.2)$$

$$B(\mathbf{J}) = \theta z^* x^* - (1-\alpha) \frac{\delta}{\alpha} [x^* + \theta z^*] \quad (7.3)$$

Conditions (7.i) may serve us to characterize the behavior of the equilibrium trajectories wondering around the steady state. Unfortunately, this is not an easy task, when dealing with complicate nonlinear functions. To this end, we provide a set of theorems necessary to facilitate the study of both local and global dynamics.

2.2 Periodic solutions

Let us first study the possibility that periodic solutions do emerge, which is a first way to signal that the interior steady state can be indeterminate.

In detail, we apply the neat Andronov-Hopf bifurcation theorem to verify that there exists a parameter value at which a structure of closed orbits exist around the steady state solution. We choose σ as the appropriate bifurcation parameter. To prove this, we need to check the following expression

$$G(\sigma) = \frac{\rho - \delta(1-\sigma)}{\sigma^2} [\delta(1-\sigma) - \rho] + (1-\alpha) \delta \frac{\delta(\sigma-\alpha) + \alpha\rho}{2\alpha^2\sigma^2} (2\alpha - \sigma) \quad (8)$$

where $G(\sigma) = -B(\mathbf{J}) \cdot \text{tr}(\mathbf{J}) + \text{Det}(\mathbf{J})$, which vanishes at different solutions of σ (see, Fig. 1).



Example 1 Let $(\rho, \alpha, \delta) = (0.05, 0.33, 0.25)$ which are standard values in the literature. Therefore, $G(\sigma) = 0$ when $\bar{\sigma}_1 = 0.4538$ and $\bar{\sigma}_2 = 0.6368$.

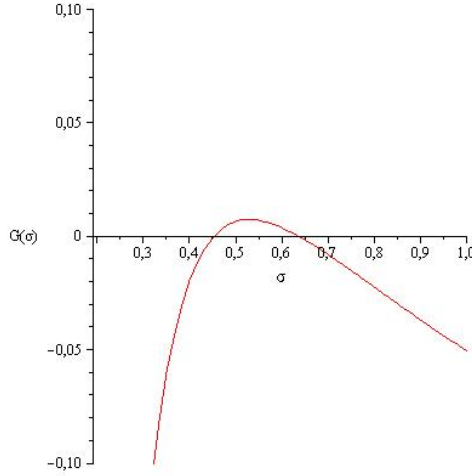


Fig. 1: The Hopf bifurcation curve

Multiple values of σ are thus able to annihilate $G(\sigma)$. If this happens, we will show that any variation of σ around $\bar{\sigma}_i$, $i \in [1, 2]$ can force the variables associated to the complex conjugate eigenvalues to oscillate around a common constant value. This means also that, an invariant cycle (a closed orbit) may emerge around the steady state, or collapses onto it. We want to show that parameter σ plays a crucial role in the characterization of an optimal solution to our maximization problem, and thus matters in the process of a long run sustainable growth, giving rise to a boom and bust sustained cycle, where tourism services lead growth but start exploiting natural resources until economic indicators start a sharp and rapid contraction when resources are depleted and mass tourism moves to different places, thus lowering human impact on the environment, which starts restoring natural capital and thus enters a new phase of tourism attracting place, which pushes up again the economic activities in a periodic evolution consistent with the life-cycle hypothesis.

Unfortunately, this analysis may not be sufficient to provide a complete picture of the stability properties of the economy, for more complicated outcomes can emerge if we move slightly off the vicinity of the steady state, and may thus complicate the adequate policy actions to be implemented. A deep investigation of this issue is provided in the next section.



3 Periodic orbits and global indeterminacy

Studying the properties of an equilibrium outside the small neighborhood of the steady state is not an easy task, especially when dealing with non-linear functions that complicate the algebraic calculations behind it.

Firstly, we need to put the system (R) in an appropriate canonical form to work with. To do this, we translate the equilibrium fixed point to the origin, by assuming

$$\begin{aligned}\tilde{x} &= x - \bar{x}^*, \\ \tilde{q} &= q - \bar{q}^* \\ \tilde{z} &= z - \bar{z}^*\end{aligned}$$

which implies

$$\begin{aligned}\dot{\tilde{x}} &= \left\{ -\frac{\rho}{\sigma} + \left(\frac{\alpha - \sigma}{\sigma} \right) A(\bar{q}^* + \tilde{q})^{\alpha-1} (\bar{z}^* + \tilde{z})^{(1-\alpha)} + (\bar{x}^* + \tilde{x}) \right\} (\bar{x}^* + \tilde{x}) \\ \dot{\tilde{q}} &= \left\{ -\delta + A(\bar{q}^* + \tilde{q})^{\alpha-1} (\bar{z}^* + \tilde{z})^{(1-\alpha)} - (\bar{x}^* + \tilde{x}) + \delta(\bar{z}^* + \tilde{z}) \right\} (\bar{q}^* + \tilde{q}) \\ \dot{\tilde{z}} &= \left\{ \delta \frac{1-\alpha}{\alpha} - (\bar{x}^* + \tilde{x}) + \delta(\bar{z}^* + \tilde{z}) \right\} (\bar{z}^* + \tilde{z})\end{aligned}\tag{Q}$$

A second order Taylor expansion of this vector field allows us to put (Q) in the form

$$\begin{pmatrix} \dot{\tilde{x}} \\ \dot{\tilde{q}} \\ \dot{\tilde{z}} \end{pmatrix} = \mathbf{J} \begin{pmatrix} \tilde{x} \\ \tilde{q} \\ \tilde{z} \end{pmatrix} + \begin{pmatrix} \tilde{f}_1(\tilde{x}, \tilde{q}, \tilde{z}) \\ \tilde{f}_2(\tilde{x}, \tilde{q}, \tilde{z}) \\ \tilde{f}_3(\tilde{x}, \tilde{q}, \tilde{z}) \end{pmatrix}$$

where the \tilde{f}_i terms represent the non linear terms (of order 2).

Proposition 2 *Let \mathbf{T} be a matrix of the eigenvectors associated with the structure of eigenvalues of \mathbf{J} at the bifurcation point. Then, it is possible to put the system (Q) in the following Jordan normal form:*

$$\dot{\mathbf{w}} = \mathbf{T}^{-1} \mathbf{J}(0) \mathbf{T} \mathbf{w} + F_i$$

where $F_i = \mathbf{T}^{-1} \tilde{f}_i(\mathbf{T} \mathbf{w})$, given the associated change in coordinates

$$\begin{pmatrix} \tilde{x} \\ \tilde{q} \\ \tilde{z} \end{pmatrix} = \mathbf{T} \begin{pmatrix} w_1 \\ w_2 \\ w_3 \end{pmatrix}$$



which transforms system (Q) into

$$\begin{pmatrix} \dot{w}_1 \\ \dot{w}_2 \\ \dot{w}_3 \end{pmatrix} = \begin{bmatrix} 0 & 1 & 0 \\ 0 & 0 & 1 \\ \varepsilon_1 & \varepsilon_2 & \varepsilon_3 \end{bmatrix} \begin{pmatrix} w_1 \\ w_2 \\ w_3 \end{pmatrix} + \begin{pmatrix} F_1(w_1, w_2, w_3) \\ F_2(w_1, w_2, w_3) \\ F_3(w_1, w_2, w_3) \end{pmatrix} \quad (10)$$

where $\varepsilon_1 = \text{Det}(\mathbf{J})$, $\varepsilon_2 = -B(\mathbf{J})$, $\varepsilon_3 = \text{tr}(\mathbf{J})$, and F_i are the transformed second order non linear terms.

Proof. See the procedure detailed in Algaba et al. (1999) and Gamero et al. (1991). ■

We are thus able at this step to restrict the vector field in (10) to the plane (w_1, w_2) whose eigenspace, at the bifurcation value $\sigma = \bar{\sigma}$, corresponds to the complex pair of eigenvalues, $\lambda_{1,2} = \pm\omega i$, which is topologically invariant with respect to the original system (S).¹ A center manifold reduction of the linearized vector field allows us to investigate this case.

Proposition 3 *A second order approximation of the center manifold which reduces the vector field in (10) is given by the following equation*

$$w_3 = h(w_1, w_2) = \frac{1}{2}[\tau_1 w_1^2 + \tau_2 w_1 w_2 + \tau_3 w_2^2]$$

where τ_i are coefficients that satisfy the stability condition $\dot{w}_3 = 0$.

Proof. See Appendix. ■

The vector field at the center manifold therefore reduces to

$$\begin{pmatrix} \dot{w}_1 \\ \dot{w}_2 \end{pmatrix} = \begin{bmatrix} 0 & -\omega \\ \omega & 0 \end{bmatrix} \begin{pmatrix} w_1 \\ w_2 \end{pmatrix} + \begin{pmatrix} \bar{F}^1(w_1, w_2, h(w_1, w_2)) \\ \bar{F}^2(w_1, w_2, h(w_1, w_2)) \end{pmatrix} \quad (11)$$

where \bar{F}^i represent the second order non linear terms of the vector field at the center manifold.

The restricted vector field (11) allows us to properly investigate the presence of periodic solutions in the two-dimensional phase space (w_1, w_2) , by computing the standard first Lyapunov coefficient

$$q = \frac{1}{16\omega} [\bar{F}_{w_1 w_2}^1 (\bar{F}_{w_2 w_2}^1 + \bar{F}_{w_1 w_1}^1) - \bar{F}_{w_1 w_2}^2 (\bar{F}_{w_2 w_2}^2 + \bar{F}_{w_1 w_1}^2) - \bar{F}_{w_1 w_1}^1 \bar{F}_{w_1 w_1}^2 + \bar{F}_{w_2 w_2}^1 \bar{F}_{w_2 w_2}^2]$$

¹If we substitute $B\mathbf{J} \cdot \text{tr}\mathbf{J} = \text{Det}\mathbf{J}$ in the characteristic equation at the bifurcation point, one eigenvalue is real and positive, and equal to the trace, $\lambda_r = \text{tr}\mathbf{J}$, whilst the other two eigenvalues are complex conjugate, $\lambda_c = \pm\omega i$, assuming $\omega = \sqrt{B\mathbf{J}}$.



Remark 2 *If $q < 0$ the emerging cycle around the steady state is attracting, i.e. a supercritical Hopf bifurcation occurs. (The statement is reversed for $q > 0$.)*

The value of q , at the two bifurcation points, can be either positive or negative. Both bifurcations can therefore be supercritical or subcritical. The fixed points are thus unstable and the orbits are attracting on the center manifold. This is shown by means of the following numerical example.

Example 2 *Assume $\rho = 0.05$, $\alpha = 0.33$, $\delta = 0.25$. If $\sigma = \bar{\sigma}_1$, then $q = -8.8 \cdot 10^{-10} < 0$, that is to say the bifurcation is supercritical, the steady state is unstable and the periodic orbits are attracting on the center manifold. On the contrary, in correspondence of $\sigma = \bar{\sigma}_2$, we have $q = 2.54 \cdot 10^{14} > 0$, that is to say the bifurcation is subcritical, and the periodic orbits start repelling (see, Fig. 2).*

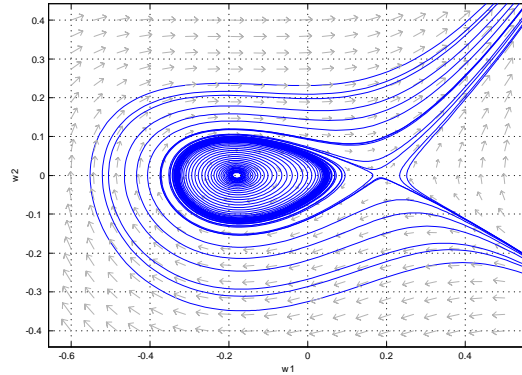


Fig. 2. Periodic orbits near the equilibrium.

We are thus able to conclude that different periodic solutions may emerge in presence of resource depletion for tourism services, which leads consequently to the rise of some indeterminacy problems, which might be able to explain the rise and fall of different nowadays tourism-based economies that, even though endowed with the same initial conditions, may at some point start to perform differently in growth rate terms and thus follow different long run equilibrium paths.

4 Chaotic dynamics

As previously anticipated, the ability of intertemporal equilibrium theory to provide indications about future economic conditions, given the initial state



of the economy, has been questioned in several studies, and prediction of future economic conditions can be completely undermined. In this case, a chaotic regime may emerge as the model parameters are adequately set to determine the existence of a family of homoclinic orbits doubly asymptotic to a saddle-focus, which is commonly known as the Shilnikov homoclinic bifurcation.

Our aim is to characterize the region of the parameters space where the Shilnikov (1965) theorem is satisfied. An example of chaotic dynamics is also presented, and the economic implications of our results are discussed.

Proposition 4 *Let $\Omega = (\alpha, \delta, \rho, \sigma)$ be the set of parameters. Choose $\sigma = \bar{\sigma}$. If $\bar{\Omega} \equiv \{\bar{\sigma} \in \Omega : \mathbf{J} \text{ has one real and two complex conjugate eigenvalues}\}$, then system \mathcal{Q} exhibits a saddle-focus dynamics.*

Proof. For the equilibrium to be a saddle-focus, we require a pair of eigenvalues with non-zero imaginary part. Solving the characteristic equation by Cardano's formula, provides the following three roots $\lambda_1 = \eta$ and $\lambda_{2,3} = \tau \pm \omega i$, with $\eta = \frac{\text{Tr}(\mathbf{J})}{3} + v + z$, $\tau = \frac{\text{Tr}(\mathbf{J})}{3} - \frac{v+z}{2}$, and $\omega = \sqrt{3} \frac{v-z}{2}$, given $v = \sqrt[3]{-\frac{q}{2} + \sqrt{\Delta}}$, $z = \sqrt[3]{-\frac{q}{2} - \sqrt{\Delta}}$, and being $\Delta = \left(\frac{p}{3}\right)^3 + \left(\frac{q}{2}\right)^2$ the discriminant. Moreover, $p = \frac{3B(\mathbf{J}) - \text{Tr}(\mathbf{J})^2}{3}$, $q = -\text{Det}(\mathbf{J}) + 2\frac{\text{Tr}(\mathbf{J})^3}{27} + \frac{\text{Tr}(\mathbf{J})B(\mathbf{J})}{3}$, and $i = \sqrt{-1}$ is standard notation for imaginary unit. Therefore, for λ_1 to be a real negative root, and $\lambda_{2,3}$ to be complex conjugate, we need $\Delta > 0$. ■

We can thus move to the main point of the paper.

Theorem 3 *Consider the dynamical system*

$$\frac{dY}{dt} = f(Y, \alpha), \quad Y \in R^3, \quad \alpha \in R^1$$

with f sufficiently smooth. Assume f has a hyperbolic saddle-focus equilibrium point $Y_0 = 0$ at $\alpha = 0$ implying that eigenvalues of the Jacobian $\mathbf{J} = Df$ are of the form η and $\tau \pm \omega i$ where η , τ and ω are real constants with $\eta\tau < 0$. If a homoclinic orbit Γ_0 based at Y_0 exists, then the map, defined in the neighborhood of the homoclinic orbit of the system, possesses an infinite number of Smale horseshoes in its discrete dynamics.

We can prove the existence of a family of homoclinic orbits doubly asymptotic to the fixed point P^* , through the method of the undetermined



coefficients (cf., *inter al.*, Shang et Han, 2005). This implies that the transformed variables w_1 , w_2 and w_3 evolve according to the following expressions

$$\begin{aligned} w_1 &= \left\{ \begin{array}{ll} \xi e^{-\bar{\eta}t} + e^{-2\bar{\eta}t} & t \leq 0 \\ e^{\bar{\tau}t} [\varsigma \cos(\bar{\omega}t) + \psi \sin(\bar{\omega}t)] + e^{2\bar{\omega}t} [\cos(2\bar{\omega}t) - \sin(2\bar{\omega}t)] & t \geq 0 \end{array} \right\} \\ w_2 &= \left\{ \begin{array}{ll} e^{-2\bar{\eta}t} & t \leq 0 \\ e^{\bar{\tau}t} [\varsigma \cos(\bar{\omega}t) - \psi \sin(\bar{\omega}t)] + e^{2\bar{\omega}t} [\cos(2\bar{\omega}t) - \sin(2\bar{\omega}t)] & t \geq 0 \end{array} \right\} \\ w_3 &= \left\{ \begin{array}{ll} e^{-2\bar{\eta}t} & t \leq 0 \\ e^{2\bar{\omega}t} [\cos(2\bar{\omega}t) - \sin(2\bar{\omega}t)] & t \geq 0 \end{array} \right\} \end{aligned}$$

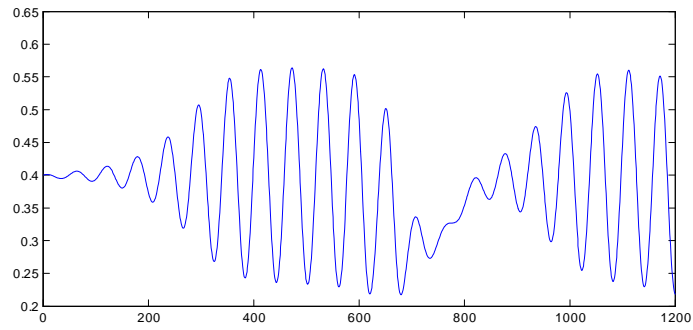
where (ξ, ψ, ς) are arbitrary parameters for convergence of the series at $t = 0$.

We discuss here below an example of chaotic trajectories arising from system \mathcal{Q} .

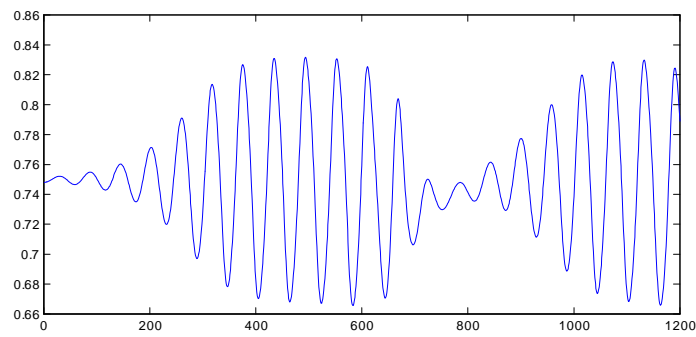
Example 4 Recall Example 2. Set $(\alpha, \delta, \rho, \sigma) = (0.33, 0.25, 0.05, 0.61)$, with $\sigma \in [\bar{\sigma}_1, \bar{\sigma}_2]$, then $\lambda_1 \simeq -7.4821$ and $\lambda_{2,3} \simeq 2.7259 \pm 1.864i$. Let also $(\xi, \psi, \varsigma) \simeq (\frac{1}{2}, \frac{1}{2}, \frac{1}{5})$. Then our economy presents Shilnikov chaos, inducing volatility bursts and large amplitude oscillations in the variables of the model,



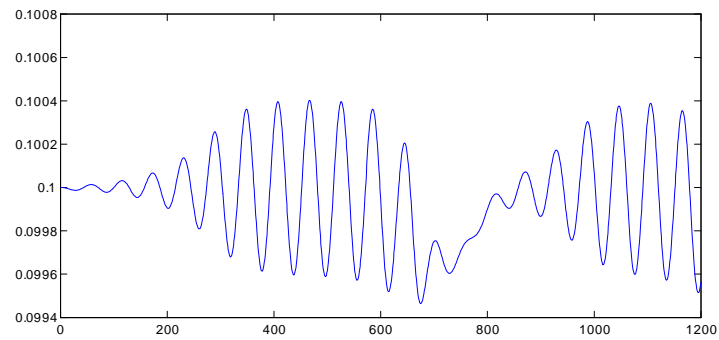
as clearly depicted in the following diagrams:



$w_1(t)$



$w_2(t)$



$w_3(t)$



5 Concluding Remarks

The raise of multiple equilibria and indeterminacy of the steady state solution has been commonly investigated in the literature to explain the diversity of growth rates across countries. However, when the system is characterized by highly nonlinear relationships the resulting dynamics around the steady state can be even more complex.

To shed some light in this field, we presented a model, arguing that a crucial aspect for the occurrence of both indeterminacy and cyclical adjustment towards the steady state might be the presence of particular bifurcation values of the inverse of the intertemporal elasticity of substitution. Conclusions to our analysis confirm that such parameter matters in the transition towards a long-run sustainable equilibrium, thus leaving space to other more complicated dynamic phenomena characterized by periodic solutions and chaotic dynamics to stuck the economy in a low level equilibrium trap.

References

- [1] Algaba, A.; Freire, E.; Gamero, E. (1999). Hypernormal forms for equilibria of vector fields. Codimension one linear degeneracies, *Rocky Mountain Journal of Mathematics*, 29, 13–45.
- [2] Baggio, R. (2008). Symptoms of complexity in a tourism system. *Tourism Analysis*, 13(1), 1–20.
- [3] Bella, G.; Mattana, P. (2014). Global indeterminacy of the equilibrium in the Chamley model of endogenous growth in the vicinity of a Bogdanov-Takens bifurcation. *Mathematical Social Sciences*, 71, 69–79.
- [4] Benhabib, J.; Schmitt-Grohé, S.; Uribe, M. (2001). The perils of Taylor rules. *Journal of Economic Theory*, 96, 40–69.
- [5] Bornhorst, T.; Ritchie, J.; Sheehan, L. (2010). Determinants of Tourism Success for DMOs & destinations: An Empirical Examination of Stakeholders' Perspectives. *Tourism Management*, 31, 572–589.
- [6] Brau, R.; Lanza, A.; Pigliaru, F. (2007). How fast are small tourism countries growing? Evidence from the data for 1980-2003. *Tourism Economics*, 13(4), 603–613.



- [7] Brida, J.G.; Sanchez Carrera, E.J.; Risso, W.A. (2008). Tourism's Impact on Long-Run Mexican Economic Growth. *Economics Bulletin*, 3(21), 1–8.
- [8] Brida, J.G.; Pulina, M. (2010). A literature review on the tourism-led-growth hypothesis. Working Paper CRENoS 2010.17.
- [9] Butler, R. (1980). The concept of a tourist area cycle of evolution. *Canadian Geographer*, 24, 5–12.
- [10] Cole, S. (2009). A logistic tourism model: Resort Cycles, Globalization and Chaos. *Annals of Tourism Research*, 36(4), 689–714.
- [11] Finco, M.V.A. (2009). Poverty-Environment Trap: A non linear probit model applied to rural areas in the North of Brazil. *American-Eurasian J. Agric. & Environ. Sci.*, 5(4), 533–539.
- [12] Gamero, E.; Freire, E.; Ponce, E. (1991). Normal forms for planar systems with nilpotent linear part. In: Seydel, R.; Schneider, F.W.; Küpper, T.; Troger, H. (Eds.), *Bifurcation and Chaos: Analysis, Algorithms, Applications*. International Series of Numerical Mathematics, 97, Birkhäuser, Basel, 123–127.
- [13] Katircioglu, S.T. (2009). Testing the tourism-led growth hypothesis: The case of Malta. *Acta Oeconomica*, 59(3), 331–343.
- [14] Mattana, P.; Venturi, B. (1999). Existence and stability of periodic solutions in the dynamics of endogenous growth. *International Review of Economics and Business*, 46, 259–284.
- [15] Musu, I. (1995). Transitional Dynamics to Optimal Sustainable Growth. FEEM Working Paper 50.95.
- [16] Nowak, J.-J.; Sahli, M.; Cortés-Jiménez, I. (2007). Tourism, capital good imports and economic growth: theory and evidence for Spain. *Tourism Economics*, 13(4), 515–536.
- [17] Rosendahl, K.E. (1996). Does improved environmental policy enhance economic growth?. *Environmental and Resource Economics*, 9, 341–364.
- [18] Sachs, J.D.; Warner, A.M. (2001). Natural resources and economic development: The curse of natural resources. *European Economic Review*, 45, 827–838.



- [19] Schubert, F.S.; Brida, J.G.; Risso, W.A. (2010). The impacts of international Tourism demand on economic growth of small economies dependent of tourism. *Tourism Management*, 32(2), 377–385.
- [20] Shang, D.; Han, M. (2005). The existence of homoclinic orbits to saddle-focus. *Applied Mathematics and Computation*, 163, 621–631.
- [21] Shilnikov, L.P. (1965). A case of the existence of a denumerate set of periodic motions. *Sov. Math. Docl.*, 6, 163–166.

A Appendix

The Current value Hamiltonian associated with system \mathcal{P} is given by:

$$H_C = \frac{c^{1-\sigma} - 1}{1-\sigma} + \lambda \left[Ak^\alpha g^{\beta(1-\alpha)} E^{(1-\beta)(1-\alpha)} - c \right] + \mu \left[\delta(E - g^\beta E^{1-\beta}) \right]$$

where λ and μ represent the shadow prices of physical and natural capital, respectively. The first order condition for a maximum requires that the discounted Hamiltonian be maximized with respect to its control variables, which implies

$$c^{-\sigma} = \lambda \tag{A.1}$$

$$\lambda(1-\alpha)Ak^\alpha = \mu\delta g^{\beta\alpha} E^{(1-\beta)\alpha} \tag{A.2}$$

accompanied by the law of motion of each costate variable

$$\frac{\dot{\lambda}}{\lambda} = \rho - \alpha Ak^{\alpha-1} g^{\beta(1-\alpha)} E^{(1-\beta)(1-\alpha)} \tag{A.3}$$

$$\frac{\dot{\mu}}{\mu} = \rho - (1-\beta)\frac{\lambda}{\mu}(1-\alpha)Ak^\alpha g^{\beta(1-\alpha)} E^{(1-\beta)(1-\alpha)-1} - \delta \left[1 - (1-\beta)g^\beta E^{-\beta} \right] \tag{A.4}$$

Taking log-derivatives of (A.1) and (A.2), we derive:

$$-\sigma \frac{\dot{c}}{c} = \frac{\dot{\lambda}}{\lambda} \tag{A.5}$$

$$\frac{\dot{\lambda}}{\lambda} + \alpha \frac{\dot{k}}{k} - \beta \alpha \frac{\dot{g}}{g} - (1-\beta)\alpha \frac{\dot{E}}{E} = \frac{\dot{\mu}}{\mu} \tag{A.6}$$



Therefore, problem \mathcal{P} can be defined by the following system of four first order differential equations:

$$\begin{aligned}
\frac{\dot{k}}{k} &= Ak^{\alpha-1}g^{\beta(1-\alpha)}E^{(1-\beta)(1-\alpha)} - \frac{c}{k} \\
\frac{\dot{c}}{c} &= -\frac{\rho}{\sigma} + \frac{\alpha}{\sigma}Ak^{\alpha-1}g^{\beta(1-\alpha)}E^{(1-\beta)(1-\alpha)} \\
\frac{\dot{E}}{E} &= \delta(1 - g^{\beta}E^{-\beta}) \\
\frac{\dot{g}}{g} &= -\frac{1}{\beta}\frac{c}{k} + \frac{\delta(1 - \alpha + \alpha\beta)}{\beta\alpha} + \frac{\delta}{\beta}(1 - \beta)g^{\beta}E^{-\beta}
\end{aligned} \tag{A.7}$$

To ease the analysis, system (A.7) can be further reduced, by the following convenient variable substitution, $x = \frac{c}{k}$, $q = \frac{k}{E}$, and $z = \left(\frac{g}{E}\right)^{\beta}$. That is to say,

$$\begin{aligned}
\frac{\dot{x}}{x} &= -\frac{\rho}{\sigma} + \left(\frac{\alpha - \sigma}{\sigma}\right)Aq^{\alpha-1}z^{(1-\alpha)} + x \\
\frac{\dot{q}}{q} &= \left(\frac{\dot{k}}{k} - \frac{\dot{E}}{E}\right) = -\delta + Aq^{\alpha-1}z^{(1-\alpha)} - x + \delta z \\
\frac{\dot{z}}{z} &= \beta\left(\frac{\dot{g}}{g} - \frac{\dot{E}}{E}\right) = \delta\frac{1 - \alpha}{\alpha} - x + \delta z
\end{aligned} \tag{A.8}$$

with the associated steady state values

$$\begin{aligned}
x^* &= \frac{\delta(\sigma - \alpha) + \alpha\rho}{\alpha\sigma} \\
q^* &= \left[\frac{\rho - \delta(1 - \sigma)}{\delta\sigma}\right] \left(\frac{A\alpha}{\delta}\right)^{1-\alpha} \\
z^* &= \frac{\rho - \delta(1 - \sigma)}{\delta\sigma}
\end{aligned} \tag{A.9}$$

The Jacobian matrix of the reduced system (A.9) is then

$$\mathbf{J} = \begin{bmatrix} x^* & \frac{\delta(\alpha-1)}{\alpha} \left(\frac{\alpha-\sigma}{\sigma}\right) \frac{x^*}{q^*} & \frac{\delta(1-\alpha)}{\alpha} \left(\frac{\alpha-\sigma}{\sigma}\right) \frac{x^*}{z^*} \\ q^* & \frac{\delta}{\alpha}(\alpha - 1) & \delta q^* + \frac{\delta(1-\alpha)}{\alpha} \frac{q^*}{z^*} \\ -z^* & 0 & \delta z^* \end{bmatrix}$$

with the associated Trace, Determinant and Sum of Principal Minors, respectively given by:

$$tr J = 2\delta z^* \tag{A.10}$$



$$DetJ = \frac{\delta^2(1-\alpha)(2\alpha-3\sigma)}{\alpha\sigma} x^* z^* \quad (A.11)$$

$$BJ = \delta z^* x^* - (1-\alpha) \frac{\delta}{\alpha} [x^* + \delta z^*] \quad (A.12)$$

Translation to the origin.

Substitute $\tilde{x} \equiv x - \bar{x}^*$, $\tilde{q} \equiv q - \bar{q}^*$, $\tilde{z} = z - \bar{z}^*$ in the reduced system (A.8).

$$\begin{aligned} \dot{\tilde{x}} &= \left\{ -\frac{\rho}{\sigma} + \left(\frac{\alpha-\sigma}{\sigma} \right) A(\bar{q}^* + \tilde{q})^{\alpha-1} (\bar{z}^* + \tilde{z})^{(1-\alpha)} + (\bar{x}^* + \tilde{x}) \right\} (\bar{x}^* + \tilde{x}) \\ \dot{\tilde{q}} &= \left\{ -\delta + A(\bar{q}^* + \tilde{q})^{\alpha-1} (\bar{z}^* + \tilde{z})^{(1-\alpha)} - (\bar{x}^* + \tilde{x}) + \delta(\bar{z}^* + \tilde{z}) \right\} (\bar{q}^* + \tilde{q}) \\ \dot{\tilde{z}} &= \left\{ \delta \frac{1-\alpha}{\alpha} - (\bar{x}^* + \tilde{x}) + \delta(\bar{z}^* + \tilde{z}) \right\} (\bar{z}^* + \tilde{z}) \end{aligned} \quad (A.13)$$

A second order Taylor expansion of (A.13) can be computed:

$$\begin{pmatrix} \dot{\tilde{x}} \\ \dot{\tilde{q}} \\ \dot{\tilde{z}} \end{pmatrix} = \mathbf{J} \begin{pmatrix} \tilde{x} \\ \tilde{q} \\ \tilde{z} \end{pmatrix} + \begin{pmatrix} \tilde{f}_1(\tilde{x}, \tilde{q}, \tilde{z}) \\ \tilde{f}_2(\tilde{x}, \tilde{q}, \tilde{z}) \\ \tilde{f}_3(\tilde{x}, \tilde{q}, \tilde{z}) \end{pmatrix} \quad (A.14)$$

being \tilde{f}_i the nonlinear terms of the expanded vector field:

$$\begin{aligned} \tilde{f}_1(\tilde{x}, \tilde{q}, \tilde{z}) &= \tilde{x}^2 + \frac{(\alpha-1)(\alpha-2)(\alpha-\sigma)A\bar{q}^{*\alpha-3}\bar{z}^{*(1-\alpha)}\bar{x}^*}{\sigma} \tilde{q}^2 - \frac{\alpha(1-\alpha)(\alpha-\sigma)A\bar{q}^{*\alpha-1}\bar{z}^{*- \alpha-1}\bar{x}^*}{\sigma} \tilde{z}^2 - \\ &\quad - \frac{(1-\alpha)^2(\alpha-\sigma)A\bar{q}^{*\alpha-2}\bar{z}^{*- \alpha}\bar{x}^*}{\sigma} \tilde{q} - \mu\tilde{x} + \left[\frac{\rho}{\sigma^2} - \frac{\alpha A\bar{q}^{*\alpha-1}\bar{z}^{*(1-\alpha)}}{\sigma^2} \right] v\tilde{x} + \\ &\quad + \left[-\frac{2\rho}{\sigma^3} + \frac{2\alpha A(\bar{q}^* + \tilde{q})^{\alpha-1}(\bar{z}^* + \tilde{z})^{(1-\alpha)}}{\sigma^3} \right] v^2 - \frac{\alpha(\alpha-1)A\bar{q}^{*\alpha-2}\bar{z}^{*(1-\alpha)}\bar{x}^*}{\sigma^2} v\tilde{q} - \frac{\alpha(1-\alpha)A\bar{q}^{*\alpha-1}\bar{z}^{*1-\alpha}\bar{x}^*}{\sigma^2} v\tilde{z} \\ \tilde{f}_2(\tilde{x}, \tilde{q}, \tilde{z}) &= (\alpha-1)^2 A\bar{q}^{*\alpha-2}\bar{z}^{*(1-\alpha)} \tilde{q}^2 - \alpha(1-\alpha)A\bar{q}^{*\alpha-1}\bar{z}^{*- \alpha-1} \tilde{q}^* \tilde{z}^2 - \tilde{x}\tilde{q} - \\ &\quad - (1-\alpha)^2 A\bar{q}^{*\alpha-1}\bar{z}^{*- \alpha} \tilde{q}\tilde{z} \\ \tilde{f}_3(\tilde{x}, \tilde{q}, \tilde{z}) &= \delta\tilde{z}^2 - \tilde{x}\tilde{z} \end{aligned}$$

Following the detailed procedure in Algaba et al. (2003), system (A.14) can be put in a more convenient Jordan normal form,

$$\begin{pmatrix} \dot{w}_1 \\ \dot{w}_2 \\ \dot{w}_3 \end{pmatrix} = \begin{bmatrix} 0 & 1 & 0 \\ 0 & 0 & 1 \\ \varepsilon_1 & \varepsilon_2 & \varepsilon_3 \end{bmatrix} \begin{pmatrix} w_1 \\ w_2 \\ w_3 \end{pmatrix} + \begin{pmatrix} F_1(w_1, w_2, w_3) \\ F_2(w_1, w_2, w_3) \\ F_3(w_1, w_2, w_3) \end{pmatrix} \quad (A.15)$$

via the change of coordinates

$$\begin{pmatrix} \tilde{x} \\ \tilde{q} \\ \tilde{z} \end{pmatrix} = \mathbf{T} \begin{pmatrix} w_1 \\ w_2 \\ w_3 \end{pmatrix}$$



made by the transformation matrix $\mathbf{T} = [\mathbf{u}, \mathbf{v}, \mathbf{z}]^T$ with

$$\mathbf{u} = \begin{bmatrix} -\frac{j_{23}^*}{j_{31}^*} \\ \frac{j_{11}^* j_{23}^* - j_{13}^* j_{31}^*}{j_{12}^* j_{31}^*} \\ 1 \end{bmatrix}$$

$$\mathbf{v} = \begin{bmatrix} -\frac{1}{z} \\ \frac{x + \delta q + (1 - \alpha) A q^\alpha z^{-\alpha}}{q z} \\ 0 \end{bmatrix}$$

$$\mathbf{z} = \begin{bmatrix} -\frac{j_{33}^*}{j_{31}^*} \\ 0 \\ 1 \end{bmatrix}$$

and where $\varepsilon_1 = \text{Det}J$, $\varepsilon_2 = -BJ$, $\varepsilon_3 = \text{Tr}J$, being $F_i = \mathbf{T}^{-1} \tilde{f}_i(\mathbf{T}\mathbf{w})$ the transformed second order non linear terms

To study the stability of periodic orbits around the steady state, we consider the Andronov-Hopf bifurcation coefficient:

$$q = \frac{1}{16\omega} [\bar{F}_{w_1 w_2}^1 (\bar{F}_{w_2 w_2}^1 + \bar{F}_{w_1 w_1}^1) - \bar{F}_{w_1 w_2}^2 (\bar{F}_{w_2 w_2}^2 + \bar{F}_{w_1 w_1}^2) - \bar{F}_{w_1 w_1}^1 \bar{F}_{w_1 w_1}^2 + \bar{F}_{w_2 w_2}^1 \bar{F}_{w_2 w_2}^2]$$

where

$$\begin{aligned} \bar{F}_{w_1 w_2}^1 &= 2u_1 v_1 + 2(\alpha - 1)(\alpha - 2) \left(\frac{\alpha - \sigma}{\sigma} \right) A \bar{q}^{*\alpha-3} \bar{z}^{*(1-\alpha)} \bar{x}^* u_2 v_2 - \\ &\quad - \frac{(1 - \alpha)^2 (\alpha - \sigma)}{\sigma} A \bar{q}^{*\alpha-2} \bar{z}^{*- \alpha} \bar{x}^* v_2 \\ \bar{F}_{w_2 w_2}^1 &= (\alpha - 1)^2 A \bar{q}^{*\alpha-2} \bar{z}^{*(1-\alpha)} v_2^2 - v_1 v_2 \\ \bar{F}_{w_1 w_1}^1 &= 2u_1^2 + 2(\alpha - 1)(\alpha - 2) \left(\frac{\alpha - \sigma}{\sigma} \right) A \bar{q}^{*\alpha-3} \bar{z}^{*(1-\alpha)} \bar{x}^* u_2^2 - \\ &\quad - 2\alpha(1 - \alpha) \left(\frac{\alpha - \sigma}{\sigma} \right) A \bar{q}^{*\alpha-1} \bar{z}^{*- \alpha-1} \bar{x}^* - 2(1 - \alpha)^2 \left(\frac{\alpha - \sigma}{\sigma} \right) A \bar{q}^{*\alpha-2} \bar{z}^{*- \alpha} \bar{x}^* u_2 \end{aligned}$$

and

$$\begin{aligned} \bar{F}_{w_1 w_2}^2 &= (\alpha - 1)^2 A \bar{q}^{*\alpha-2} \bar{z}^{*(1-\alpha)} u_2 v_2 - (u_1 v_2 + v_1 u_2) - (1 - \alpha)^2 A \bar{q}^{*\alpha-1} \bar{z}^{*- \alpha} v_2 \\ \bar{F}_{w_2 w_2}^2 &= 2(\alpha - 1)^2 A \bar{q}^{*\alpha-2} \bar{z}^{*(1-\alpha)} v_2 - 2v_1 v_2 \\ \bar{F}_{w_1 w_1}^2 &= 2(\alpha - 1)^2 A \bar{q}^{*\alpha-2} \bar{z}^{*(1-\alpha)} u_2 - 2\alpha(1 - \alpha) A \bar{q}^{*\alpha-1} \bar{z}^{*- \alpha-1} \bar{q}^* - \\ &\quad - 2u_1 u_2 - 2(1 - \alpha)^2 A \bar{q}^{*\alpha-1} \bar{z}^{*- \alpha} u_2 \end{aligned}$$



Computation of the center manifold.

Assume $w_3 = h(w_1, w_2)$ with h smooth function. The properties of the center manifold imply

$$\dot{w}_3 - \frac{\partial h}{\partial w_1} \dot{w}_1 - \frac{\partial h}{\partial w_2} \dot{w}_2 = 0 \quad (\text{A.16})$$

Suppose now

$$w_3 = h(w_1, w_2) = \frac{1}{2}[\tau_1 w_1^2 + \tau_2 w_1 w_2 + \tau_3 w_2^2] \quad (\text{A.17})$$

where τ_1 , τ_2 and τ_3 are unknown coefficients. Time-differentiating (A.17), and substituting into (A.16), we obtain the following relation

$$w_1^2 + \frac{\Phi Tr J \tau_2 + 2v_2 A'_3 - 2v_1 B'_3 + 2\chi C'_3 - 2\Phi \tau_1}{\Phi Tr J \tau_1 + 2v_2 A'_1 - 2v_1 B'_1 + 2\chi C'_1} w_1 w_2 + \frac{\Phi Tr J \tau_3 + 2v_2 A'_2 - 2v_1 B'_2 + 2\chi C'_2 - \Phi \tau_2}{\Phi Tr J \tau_1 + 2v_2 A'_1 - 2v_1 B'_1 + 2\chi C'_1} w_2^2 = 0$$

Finally, equating coefficients to zero, we find

$$\begin{aligned} \tau_1 &= \frac{2[-v_2 A'_1 + v_1 B'_1 - \chi C'_1]}{\Phi Tr J}, \quad \tau_2 = \frac{2Tr J[-v_2 A'_3 + v_1 B'_3 - \chi C'_3] + 4[-v_2 A'_1 + v_1 B'_1 - \chi C'_1]}{\Phi Tr J^2} \\ \tau_3 &= \frac{2[-v_2 A'_2 + v_1 B'_2 - \chi C'_2] Tr J^2 + 2Tr J v + 4[-v_2 A'_1 + v_1 B'_1 - \chi C'_1]}{\Phi Tr J^3} \end{aligned}$$

where all other coefficients are intricate combinations of the nonlinear terms \bar{F}_i , which are not reported for the sake of simplicity, but remain available upon request.



Absolute Negative Mobility in a Ratchet Flow

Philippe Beltrame¹

UMR1114 EMMAH, Dept. of physics, Université d'Avignon – INRA, F-84914
Avignon, France
(E-mail: philippe.beltrame@univ-avignon.fr)

Abstract. This paper is motivated by the transport of suspended particles pumped periodically through a modulated channel filled of water. The resulting flow behaves as a ratchet potential, called ratchet flow, i.e. the particle may drift to a preferential direction without bias. In order to find out the parameter range of the particle transport and to understand it, we study the deterministic particle dynamics using continuation of periodic orbits and of periodic transport solutions. We identify the onset of transport as a widening crisis. We show that for slightly asymmetric problem, the particle may drift in the opposite direction of the bias. By adding a small noise the onset of transport may be trigger leading to an Absolute Negative Mobility (ANM).

Keywords: Ratchet, Absolute Negative Mobility, synchronization, Chaos, Noise, Continuation.

1 Introduction

The transport of micro-particles through pores in a viscous fluid in absence of mean force gradient finds its motivation in many biological applications as the molecular motor or molecular pump. In the last decade, the literature shows that a periodical pore lattice without the symmetry $x \rightarrow -x$ can lead to the so-called ratchet effect allowing an transport in one direction x or $-x$. A review can be found in Hänggi and Marchesoni[12]. We focus on the set-up presented in Matthias and Müller[22] and Mathwig *et al.*[21] consisting in a macroporous silicon wafer which is connected at both ends to basins. The basins and the pore are filled with liquid with suspended particles ($1 - 10\mu m$). The experiment shows the existence of an effective transport in a certain range of parameter values. By tuning them, the direction of the effective transport may change and in particular the transport direction is opposite to the particle weight. These results may be interpreted as a ratchet effect by Kettner *et al.*[14] and Hänggi *et al.*[13] where "ratchet" refers to the noisy transport of particle without bias (zero-bias). When the transport direction is opposite to the bias, then it is called Absolute Negative Mobility (ANM), see e.g. Du and Mei[9] or Spiechowicz *et al.*[27]. Recently, we show that inertia may induce a directed transport Beltrame *et al.*[4]. In this deterministic approach where thermal fluctuations are negligible and a small inertia is taken in to account,

¹*8th CHAOS Conference Proceedings, 26-29 May 2015, Henri Poincaré Institute, Paris France*



the transport results from non-linear phenomena. Because of the existence of transport without bias, we called the fluid flow in the micro-pump: ratchet flow. Since the results of the experiment of Mathwig *et al.*[21] question the relevance of small fluctuations in the transport, in this paper, we propose to better understand the role of noise in this non-linear dynamics. And especially to focus to a possible Absolute Negative Mobility.

We consider a one-dimensional system where the Stokes force and a small random force due to fluctuations are the only forces acting on the particle. It results a ODE system which is similar to inertia ratchet as found in the literature: Barbi and Salerno[3], Mateos[18,19] and Speer *et al.*[26]. In these latter papers, transport solutions synchronized with the periodic forcing are found for the deterministic case. They show that this dynamics results from a synchronization transition as it occurs for periodically forced oscillator Pitkovsky *et al.*[24]. This regime can be destroyed via a crisis which appears after a period-doubling cascade. The synchronized transport regime may exist in the symmetric case (parity symmetry $x \rightarrow -x$), see Speer *et al.*[26] or Cubero *et al.*[6]. Obviously, it implies the existence of an opposite transport solution and then there is no transport in statistical sense. Now, if a small bias is applied, the domain of existence of opposite transport solutions do not match anymore. As consequence by varying the tuning parameter the transport direction may change and in particular the transport opposed to the bias may exist Wickenbrock *et al.*[30]. The deterministic dynamics may help to understand ANM too. For instance, in Machura *et al.*[16], the nonlinear analysis showed that stable periodic solution and unstable periodic transport solution coexist. By adding a small noise, the trajectory may escape from the bounded periodic solution and may follow during few periods the periodic transport solution. As consequence, a drift opposed to the bias is triggered by the noise.

Despite a plethora of study in this topic, there is still open issues as the transition from unbounded dynamics to transport dynamics which seems no to be clearly identified. Moreover, most of study assumed the inertia large or, in contrary, the limit case of overdamped dynamics (Kettner *et al.*[14] and Lee[15]). Here we consider moderate drag coefficient of the particle. We aim at finding transport transition and possible ANM. In order to tackle this problem we propose to study the deterministic case with inertia particle and then apply a small Gaussian noise. In addition to the time integration, the deterministic case is analyzed with the help of continuation method (Beltrame *et al.*[5] and Dijkstra *et al.*[7]). This method appears seldom in the literature dealing with ratchet (see e.g. Pototsky *et al.*[25]). However, we can follow periodic orbit (or relative periodic orbit for the transport solution) and determine their stability and bifurcation point. Thus, it is powerful to determine onsets and the kind of bifurcation.

In the present work, we consider the physical parameters: particle drag (inverse of the inertia), the mean flow of the fluid, the velocity contrast, the asymmetry of the flow and the bias (resulting from the particle weight). We analyze firstly the bounded periodic solution (symmetric and asymmetric cases), Secondly, the onset of transport is determined. Finally, we treat the case of the small perturbation due to a Gaussian noise.

2 Modeling

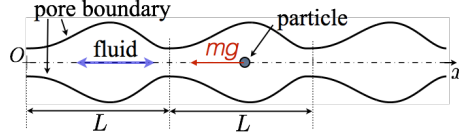


Fig. 1. Sketch of the problem: the particle translates along the x -axis of a periodic distribution of pores. It is dragged by a periodic motion of a viscous fluid. The particle weight is oriented to the negative x direction.

Let us consider a L -periodic varying channel along the line (Ox) (Figure 2) through which a viscous fluid containing suspended particles is periodically pumped. We assume that the period of the pumping period is small enough to consider a creeping flow. Such an assumption is relevant for periodicity for $L \simeq 10\mu m$ and $T \geq 1ms$ (Kettner *et al.*[14]). The particle is centered on the x -axis then the moment of the particle is neglected and the particle does not rotate. This creeping flow exerts a F_d drag force on the particle along the x axis. The set-up is vertical so that the particle weight, F_w , is oriented to the x negative and the buoyancy force, F_b , to the positive direction. Thus the particle position $x(t)$ is governed by the equation

$$m\ddot{x}(t) = F_d + F_w + F_b \quad (1)$$

To simplify, we assume that F_d is approximatively given by the Stokes drag: $F_d = -\gamma(v(x, t) - v_f(x, t))$, where γ is the drag coefficient and v and v_f are the particle velocity and the fluid velocity without particle, respectively. This expression of the drag force requires that the particle is small comparing to the channel radius. Because, it is quasi-static problem, the fluid velocity distribution without particle is proportional to the amplitude pumping so that we may write: $v(x, t) = u_0(x) \sin(2\pi t)$ for a sinusoidal pumping, where $u_0(x)$ depends on the pore profile. We obtain the adimensional governing equation

$$\ddot{x}(t) = \gamma(u_0(x(t)) \sin(2\pi t) - \dot{x}(t)) + g \quad (2)$$

where the length is scaled by the pore length L , the time by the pumping period T and the drag by m/T and $g = (F_w + F_b)/(mL/T^2)$. This equation admits an unique solution C^2 for a given position and velocity (x_i, v_i, t_i) at a time t_i . In particular, two different solutions cannot have at a given time the same position and velocity. Another straightforward result shows that particle acceleration \ddot{x} and its velocity \dot{x} remain bounded.

The velocity profile $u_0(x)$ gets the periodicity of the geometry. If the pore geometry is symmetric, we consider a sinusoidal velocity profile:

$$u_0(x) = u_m(1 + a \cos(2\pi x)) \quad (3)$$

where u_m is the mean velocity and a the velocity contrast. Otherwise for asymmetric geometry, we consider an additional parameter d related to the

asymmetry and then the pore profile is given by:

$$u_0(x) = u_m + au_m \cos\left(\pi \frac{\bar{x}}{\frac{1}{2} + d}\right) \mathbb{1}_{[0; \frac{1}{2} + d]}(\bar{x}) + au_m \cos\left(\pi \frac{\bar{x} - 1}{\frac{1}{2} - d}\right) \mathbb{1}_{[\frac{1}{2} + d; 1]}(\bar{x}) \quad (4)$$

d is the algebraic shift which ranges from $-\frac{1}{2}$ to $\frac{1}{2}$, $\bar{x} = x \bmod 1$ and $\mathbb{1}_I$ is the indicator function of the interval I ($\mathbb{1}_I(\bar{x}) = 1$ if $\bar{x} \in I$, otherwise $\mathbb{1}_I(\bar{x}) = 0$). Examples of the velocity profiles are shown in Figure 2. Note that, it is possible

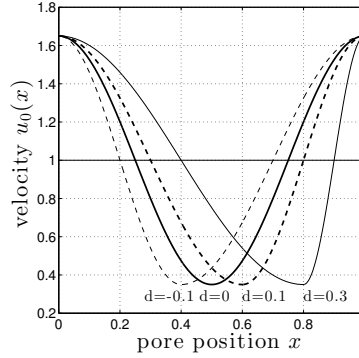


Fig. 2. Analytical velocity profiles of the flow $u_0(x)$ for $u_m = 1$, $a = 0.65$ and different values of d .

to find out pore profiles corresponding to such analytical profiles, see Beltrame *et al.*[4] and Makhoul *et al.*[17]. The asymmetry parameter d does not add a bias: if $g = 0$, the bias remains zero even if $d \neq 0$.

As explained in the introduction, we employ continuation method in order to track the periodic orbits of the Eq. (2) in the parameter space. We use the software AUTO (Doedel *et al.*[8]). This latter requires an autonomous system. In order to obtain an autonomous system and still periodic orbits, we added an oscillator which converges asymptotically to the sinusoidal functions called φ and ϕ :

$$\dot{x} = v \quad (5a)$$

$$\dot{v} = \gamma(u_0(x)\phi - v) + g \quad (5b)$$

$$\dot{\phi} = 2\pi\varphi + \phi(1 - \varphi^2 - \phi^2) \quad (5c)$$

$$\dot{\varphi} = -2\pi\phi + \varphi(1 - \varphi^2 - \phi^2) \quad (5d)$$

where the sinusoidal forcing is the asymptotical stable solution of Eqs. (5c) and (5d), i.e. $\phi \rightarrow \sin 2\pi t$ and $\varphi \rightarrow \cos(2\pi t)$ [2]. The system (5) has the same periodic solution as Eq. (2). This four-dimensional problem can be written

$$\dot{s} = (\dot{x}, \dot{v}, \dot{\varphi}, \dot{\phi}) = F(x, v, \varphi, \phi) = F(s) \quad (6)$$

The deterministic transport is only possible if u_0 is not constant, then the velocity field $u_0(x)$ constitutes the ratchet flow. Considering a symmetric problem, i.e. $u_0(-x) = u_0(x)$ and $g = 0$, the function F is equivariant by the central symmetry $F(-s) = -F(s)$. As consequence, s is solution implies $-s$ is solution too. We called symmetric orbit, solution which are invariant by the central symmetry. There is two symmetric solutions: one centered the pore middle ($x = 1/2$), noted s_m and at the second one, centered at the pore inlet ($x = 0$), noted s_0 .

For the asymmetric case, it is no longer true. However, for small oscillation amplitude u_m , the problem is similar to charged particles in a non-uniform oscillating electromagnetic force McNeil and Thompson[23], it is possible to prove that there exists periodic solution centered at the extrema of $u_0(x)$. At the maximum it is unstable while it is stable at the minimum and it constitutes the only attractor.

Therefore, the analytical results do not show existence of transport solution. In the following we propose to track the periodic solutions in the parameter space.

3 Transitions to transport solutions

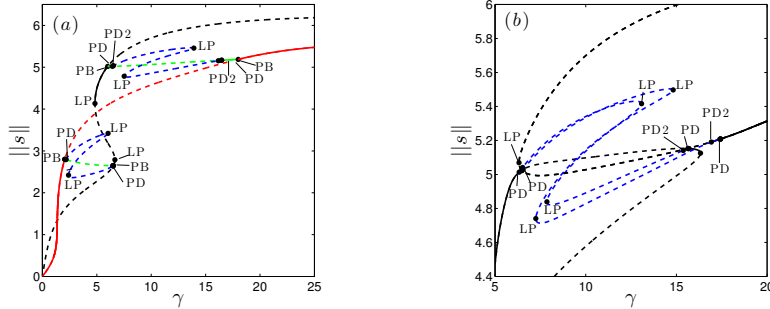


Fig. 3. (a) Bifurcation diagrams showing the periodic branches as a function of the drag γ for $a = 0.65$, $u_m = 9$ in the symmetric case. The black color indicates the s_0 branch, red the s_m branch, green the s_a branch and blue the 2-periodic branch. Dots indicate the different bifurcations: Pitchfork bifurcation (PB), Period-Doubling (PD) and (PD2) for the second period-doubling, fold bifurcation (LP). (b) Bifurcation diagram for the parameter but in the asymmetric case: $d = 0.1$ and $g = -0.1$. Black indicate 1-periodic branch and blue 2-periodic branch. In both diagrams, plain lines indicate stable orbits while dashed line correspond to unstable orbits.

We study the periodic branches for the symmetric case, i.e., the velocity profile u_0 is symmetric ($d = 0$) and there is no bias ($g = 0$). Besides the solutions s_0 and s_m , we find an asymmetric branch (Figure 3(a)). This branch is not invariant by the central symmetry and there is two branches s_a^+ and s_a^- copies by the central symmetry. Then, they have the same norm and they

do not appear in the bifurcation diagram, we note them s_a to simplify. The s_a branch results from a pitchfork bifurcation either from s_0 and s_m and thus connect both branches (Figure 3a). This arises in the intervals $[2.05, 6.52]$ and $[6, 18]$. At each end of the intervals, the same scenario, described below, occurs by varying γ away from the pitchfork bifurcation:

1. The s_a branch is stable in the vicinity of the pitchfork bifurcation but it is destabilized in the via a period doubling. We plotted the bifurcated 2-periodic branch which displays two folds. It becomes unstable via period doubling too. Note that the period-doubling cannot arise on a symmetric branch according to Swift and Wiesenfeld[28].
2. A period doubling cascade follows the first period-doubling and leads to a strange attractor. The present cascade has a behavior similar to one-dimensional map whose the distance between two consecutive bifurcations is divided by the universal Feigenbaum constant [10] $\delta \simeq 4.669$.
3. The strange attractor is bounded till an widening crisis Grebogi et al.[11]. As consequence contiguous attractors (shifted by one spatial period) are connected. Because of the spatial shift symmetry, the dynamics is no longer bounded. Of course for the symmetric case no preferential direction of the particle trajectory is observed. It is more like an anomalous diffusion Mateos and Alatrisme[20].

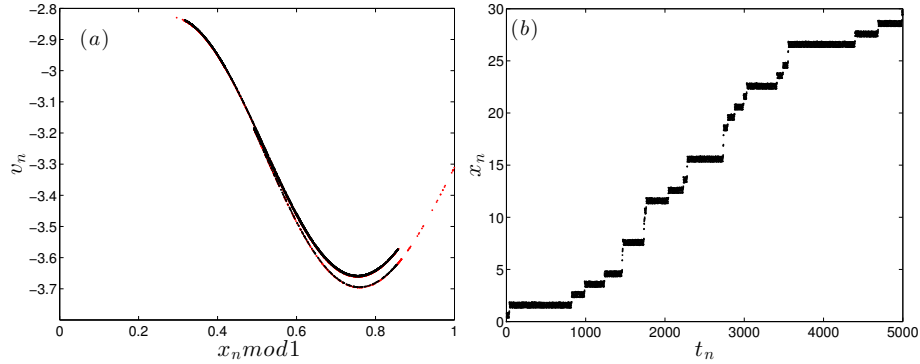


Fig. 4. (a) Poincaré section ($x_n = x(n) \text{ mod } 1, v_n = v(n)$) where $n \in \mathbb{N}$ near the onset of transport at (black dots) $\gamma = 14.70$ and (red dots) $\gamma = 14.69$, other parameters are: $u_m = 9, a = 0.65, d = 0.1, g = -0.1$. The strange attractor in black remains in the interval $[0, 1]$ while the red strange attractor is no longer bounded. Its representation modulo 1 displays a sudden expansion characteristic of the widening crisis. (b) Discrete dynamics $x_n = x(t_n)$ at discrete times $t_n = n$ of the red strange attractor of the panel (a) at $\gamma = 14.69$. An intermittent drift to positive x appears.

For the asymmetric case, similar transitions from 1-periodic orbit to the onset of the transport are observed. Nevertheless, the pitchfork bifurcations of the 1-periodic orbits vanish and instead there is two 1-periodic branches formed,

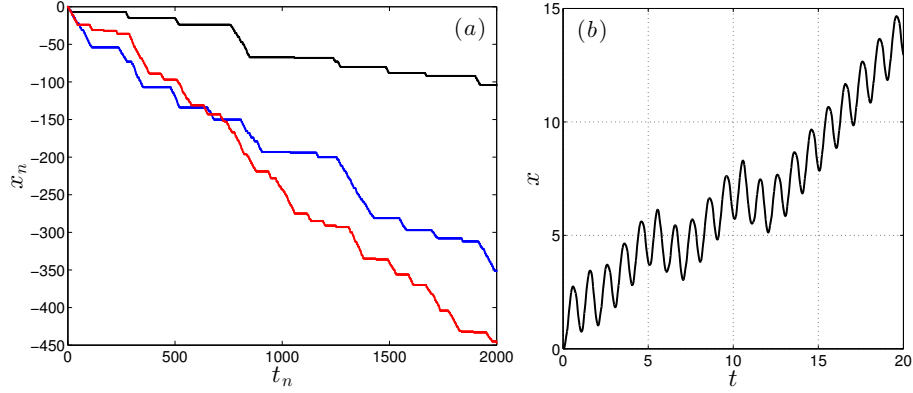


Fig. 5. (a) Discrete dynamics x_n at entire times t_n in the co-moving frame $c = +1$ near the onset of synchronization at (red) $\gamma = 13.4170$, (blue) $\gamma = 13.4165$ and (black) $\gamma = 13.4164 > \gamma_c^s$. Other parameters are $u_m = 9, a = 0.65, d = 0.1, g = -0.1$. The plateaux correspond to a near synchronized transport with $c = +1$. (b) Dynamics $x(t)$ for $\gamma = 13.416 < \gamma_c^s$: After a chaotic transition, the dynamics is the synchronized transport with $c = +1$.

firstly, by the coalescence of the s_0, s_a^+ and s_m and, secondly, by the coalescence of s_0, s_a^- and s_m . An example for $d = 0.1$ and $g = -0.1$ (other parameters being the same as for the symmetric case) is displayed in the bifurcation diagram 3b. From each branch, a period-doubling occurs. Both 2-periodic branches present two folds. A period-doubling cascade arises as for the symmetric case. We focus on the period-doubling cascade which starts at the largest drag coefficient $\gamma \simeq 16.48$. Indeed a drag coefficient smaller than 10 is quite unrealistic for small particles. The period-doubling cascade leads to an asymmetric strange attractor at $\gamma \simeq 15.2$. At $\gamma_c^t \simeq 14.698$, we observe a widening crisis connecting the contiguous attractors (Fig. 4a). But this time, because of the asymmetry of the system, there is a non-zero mean drift particle (see Fig. 4b). As expected, the dynamics after the crisis is intermittent: the dynamics spends a long time near the "ghost" bounded strange attractor and "jumps" to the other "ghost" attractor shifted by one period length. Note that, it is quite unexpected that we obtain a transport opposite to the bias. Now, we study the transport solutions.

4 Transport solutions

By decreasing further the drag coefficient, the drift velocity increases. In fact, the mean duration of the bounded-like dynamics is shorter. For γ approaching the critical value $\gamma_c^s \simeq 13.41639$, the drift velocity is almost equal to one. The epochs of bounded-like dynamics are very short comparing to the transport events. The discrete particle position $x_n = x(t_n)$ at entire times $t_n = n$ and in the comoving frame with the speed +1 is displayed in the Fig. 5a. Thus, the long plateaux correspond to the dynamics with drift velocity about one. When γ tends to γ_c^s the longer of the plateaux diverges and then the velocity tends to one. For $\gamma > \gamma_c^s$ the dynamics is periodic in the comoving frame. In other

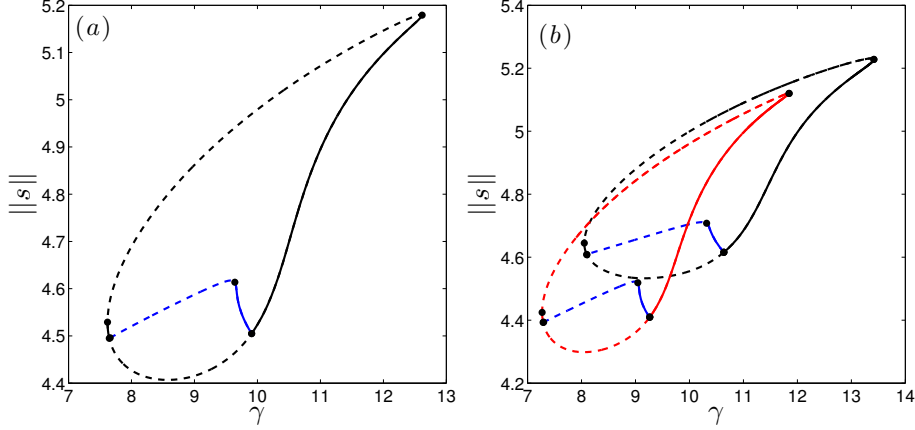


Fig. 6. (a) Bifurcation diagram of the synchronized transport solution with $c = \pm 1$ for the symmetric case. The solution emerges at saddle-node bifurcations. Dashed [plain] line indicate unstable [stable] solution branch. The stable branch becomes unstable via period-doubling (the blue branch corresponds to 2-periodic orbit), which is again unstable by period-doubling. Other parameters are $u_m = 9, a = 0.65$. (b) Bifurcation diagrams of the synchronized transport solution with (red) $c = -1$ and (black) $c = +1$ for the asymmetric case: $d = 0.1, g = -0.1$, the other parameters being the same as in panel (a). A similar bifurcation diagram as for the symmetric case occurs for both branches $c = +1$ and $c = -1$. However, their domains of existence are slightly shifted.

words, the particle advances of one spatial length after one period (Fig. 5b). It is the so-called synchronized transport. In point of view of synchronization, it is a synchronization of oscillators with forcing at moderate amplitude Vincent *et al.*[29]. Then the transition is a saddle-node. Moreover, the chaotic transient observed in Figure 5b suggests the presence of a chaotic repeller as it occurs in this case, see e.g. Pitkovsky *et al.*[24].

We study the regular transport emerging from the synchronization. Since the transport $x_t(t)$ is periodic in the comoving frame, we introduce the periodic function x_p such as

$$x_t(t) = x_p(t) + ct \quad (7)$$

where $c = \pm 1$ depending on the direction of the transport. Then if x_t is solution of Eq. 2 then it is solution of the equation:

$$\ddot{x}_p = \gamma [u_0(x_p + t)) \sin(2\pi t) - \dot{x}_p - c] + g, \quad (8)$$

It is a similar equation as Eq. (2) with an added bias $-\gamma c$. We found a transport with $c = +1$ and also the opposite transport $c = -1$ (Fig. 6b). The coexistence of opposite transport solutions is a consequence of the existence of synchronized transport in the symmetry case. Indeed, for the symmetric case, a similar scenario leads to the synchronized transport (Fig. 6a). In this case, according to the equivariance of the problem, if the solution $c = +1$ is found, then a solution $c = -1$ exists, deduced from the central symmetry (Speer *et al.*[26]). Because these solutions are no more symmetric, generically, these solutions

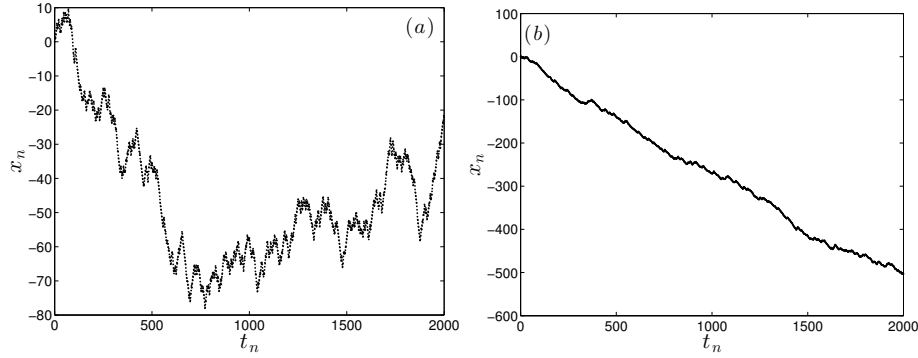


Fig. 7. Discrete time evolutions x_n at entire times t_n for $\gamma = 8.5, u_m = 9, a = 0.65$ and (a) for the symmetric case and (b) the asymmetric case: $d = 0.1, g = -0.1$. The dynamics display a competition between opposite transports. However in the asymmetric case, a net drift to x negative appears.

remain for a small enough perturbation due to the asymmetry d or/and the bias g .

All the bifurcation diagrams of synchronized transport with $c = \pm 1$ have the same structure (Fig. 6). The solution emerges from a saddle-node leading to the birth of a pair of saddle branches. The unstable branch remains unstable over its existence domain. The stable branch becomes unstable via a period doubling bifurcation. As for the bounded periodic solution, a period-doubling cascade occurs leading to a chaotic dynamics. Note however as long as an widening crisis does not occur, the drift velocity remains locked to $c = \pm 1$. After the widening crisis, the strange attractor is no longer bounded in the comoving frame. The resulting dynamics is no longer locked and it is chaotic. Examples for the symmetric and asymmetric cases are displayed in Fig. 7. For the symmetric case, there is a competition between opposite transport solutions which are unstable. The trajectory is unbounded but the mean position remains zero. It is an anomalous diffusion like. For the asymmetric case, the dynamics is similar but the resulting drift is non-zero. For the specific example in Figure 7b, we obtain a net transport direction to the negative direction.

In the asymmetric case, despite the negative bias, there is range where only the upward transport exists ($\gamma \in [11.8457, 13.41639]$). The 'trick' to obtain this unnatural dynamics was, firstly, to introduce the small flow asymmetry d which shifts the existence domains of the transport solutions $c = +1$ and $c = -1$ of the symmetric case (Fig. 6a). Then, this region persists for a small enough negative bias g . Note, without the flow asymmetry d , this region does not exist. In this region, we have a particle motion opposed to the bias like the ANM. To find a upwards dynamics due to the noise, we have to study its influence.

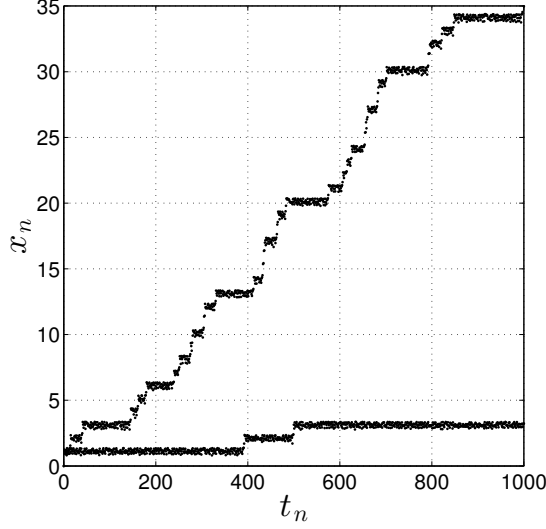


Fig. 8. Discrete stochastic particle dynamics at discrete times n governed by the Eq. (9) with the fluctuation amplitude $\epsilon = 0.1$ for two different values γ near γ_c^t : $\gamma = 14.7$ and $\gamma = 15$ (long plateaux). Other parameters are fixed to $u_m = 9, a = 0.65, d = 0.1, g = -0.1$.

5 Absolute negative mobility

We consider an additional random force, then the ODE system (2) becomes

$$\ddot{x}(t) = \gamma(u_0(x(t)) \sin(2\pi t) - \dot{x}(t)) + g + \epsilon \xi(t) \quad (9)$$

where ϵ is the amplitude of the fluctuating force, and ξ is a Gaussian stochastic process such as $\langle \xi(t) \rangle = 0$ and $\langle \xi(t)\xi(t') \rangle = \delta(t - t')$ where δ is the Dirac delta expressing that the noise is purely Markovian. In contrast to Machura *et al.*[16], the bifurcation diagrams 3 and 6 show that stable bounded periodic solutions do not coexist with unstable transport. Then, it is not possible to obtain the same kind of ANM as in Machura *et al.*[16] where the solution may escape from the stable periodic solution allowing trajectories in the neighborhood of the transport solution leading to the drift emergence. We propose to study the influence of the noise near the onset of unbounded dynamics at the widening crisis. Indeed, before the crisis and in its vicinity, contiguous strange attractors are close together then a small noise may allow to jump from a strange attractor to another one. The simulation near the strange attractor corroborates this scenario (Fig. 8). We observe a dynamics similar to the one which occurs after the crisis. Long epochs of bounded dynamics are interrupted by a jump to the upward pore. We do not observe jump to the downward direction. This is due to the asymmetry of the strange attractor. Note that the simulation in the symmetric case does not display a preferential direction. Away from the crisis by taking larger value of γ , the duration of the bounded dynamics events are statically longer. Indeed it is quite difficult

to distinguish this noisy dynamics from the deterministic dynamics. The noise triggers the crisis transition leading to the same kind of dynamics. Since the transport is opposed to the bias and it does not exist without noise, we have found an example of Absolute Negative Mobility in this framework.

In contrast, once the deterministic crisis occurred, the noise does not notably modified the dynamics and the drift velocity. It seems to have a negligible influence on the onset of the synchronized dynamics too. Moreover, the small noise does not allow to escape from the attraction basin of the periodic transport solution so that it does not destroy the synchronized transport.

6 Conclusion

In this paper we have examined a nonlinear ODE and its perturbation by a small gaussian noise as a model for inertia particle transport via a micro-pump device. The equation is similar to ratchet problem where the ratchet flow $u_0(x)$ variations play the role of the periodical potential in the ratchet literature.

The deterministic analysis showed that synchronized transport solutions exist for inertia particles with drag coefficient about 10. Their existence is not related to asymmetry. Indeed for the symmetric case, the symmetric solution s_0 or s_m becomes unstable via a pitchfork bifurcation. This latter becomes unstable via period-doubling cascade leading to a bounded strange attractor. This strange attractor is destroyed via a widening crisis allowing the emergence of an unbounded dynamics. Finally, via a synchronization transition the periodic transport appears. In the symmetric case, the transports with $c = +1$ and $c = -1$ emerge at the same onset. A similar scenario occurs in the asymmetric case, but the onset of downward and upward transport no longer coincide. When the asymmetry is small, both transport directions exist but their existence domains are shifted. Thus there is a range of the drag coefficient where only the upward transport exists even if the bias is negative.

A weak noise does not modify the synchronized dynamics. However it may trigger the onset of the unbounded dynamics created via an widening crisis. We show that for subcritical parameters, a net drift may appear due to the noise. Indeed, it allows jumps between consecutive bounded strange attractors. We obtain an Absolute Negative Mobility near the onset of the upward transport. This mechanism differs from Machura *et al.*[16] and occurs in a very small range. That shows that the study of the deterministic case and the continuation method is powerful to understand and to find such dynamics. The found ANM is generic of slightly biased ratchet problem. In fact, the scenario involves generic non-linear phenomena: symmetric breaking and crisis in a spatial periodic problem. The existence of an upwards-transport opposed to the bias can be understood as a perturbation of the symmetric case where up and down dynamics coexist. Then for a small perturbation both should exist. Finally, it is quite known that the noise allows to escape from an attractor as it occurs in our case. So, the ANM scenario presented in this paper has a quite universal aspect for ratchet problem.

References

1. Alatrliste, F. R. and Mateos, J. L. (2006). Phase synchronization in tilted deterministic ratchets. *Physica A: Statistical Mechanics and its Applications*, 372(2):263 – 271.
2. Alexander, J. C. and Doedel, E. Jand Othmer, H. G. (1990). On the resonance structure in a forced excitable system. *SIAM J. Appl. Math.*, 50(5):1373171418.
3. Barbi, M. and Salerno, M. (2000). Phase locking effect and current reversals in deterministic underdamped ratchets. *Phys. Rev. E*, 62:1988–1994.
4. Beltrame, P., Makhoul, M., and Joelson, M. Deterministic particle transport in a ratchet flow submitted
5. Beltrame, P., Knobloch, E., Hänggi, P., and Thiele, U. (2011). Rayleigh and depinning instabilities of forced liquid ridges on heterogeneous substrates. *Phys. Rev. E*, 83(1):016305.
6. Cubero, D., Lebedev, V., and Renzoni, F. (2010). Current reversals in a rocking ratchet: Dynamical versus symmetry-breaking mechanisms. *Phys. Rev. E*, 82:041116.
7. Dijkstra, H. A., Wubs, F. W., Cliffe, A. K., Doedel, E., Dragomirescu, I. F., Eckhardt, B., Gelfgat, A. Y., Hazel, A. L., Lucarini, V., Salinger, A. G., Phipps, E. T., Sanchez-Umbria, J., Schuttelaars, H., Tuckerman, L. S., and Thiele, U. (2014). Numerical bifurcation methods and their application to fluid dynamics: Analysis beyond simulation. *Commun. Comput. Phys.*, 15:1–45.
8. Doedel, E., Paffenroth, R., Champneys, A., Fairgrieve, T., Kuznetsov, Y., Sandstede, B., and Wang, X. (2001). Auto 2000: Continuation and bifurcation software for ordinary differential equations (with homcont). Technical report, Caltech.
9. Du, L. and Mei, D. (2012). Absolute negative mobility in a vibrational motor. *Phys. Rev. E*, 85:011148.
10. Feigenbaum, M. J. (1979). The universal metric properties of nonlinear transformations. *J. Statist. Phys.*, 21:669–706.
11. Grebogi, C., Ott, E., Romeiras, F., and Yorke, J. A. (1987). Critical exponents for crisis-induced intermittency *Phys. Rev. A*, 36(11):5365–5380.
12. Hänggi, P. and Marchesoni, F. (2009). Artificial brownian motors: Controlling transport on the nanoscale. *Rev. Mod. Phys.*, 81:387–442.
13. Hänggi, P., Marchesoni, F., and Nori, F. (2005). Brownian motors. In *Ann. Phys.*, volume 14, pages 51–70. Wiley-VCH Verlag.
14. Kettner, C., Reimann, P., Hänggi, P., and Müller, F. (2000). Drift ratchet. *Phys. Rev. E*, 61(1):312–323.
15. Lee, K. (2012). Overdamped transport of particles in a periodic ratchet potential. *Journal of the Korean Physical Society*, 60(11):1845–1850.
16. Machura, L., Kostur, M., Talkner, P., Luczka, J., and Hanggi, P. (2007). Absolute negative mobility induced by thermal equilibrium fluctuations. *Physical Review Letters*, 98(4):040601.
17. Makhoul, M., Beltrame, P., and Joelson, M. (2015b). Particle drag force in a periodic channel: wall effects. In *Topical Problems of Fluid Mechanics : Proceedings, Prague*, pages 141–148.
18. Mateos, J. L. (2000). Chaotic transport and current reversal in deterministic ratchets. *Phys. Rev. Lett.*, 84:258–261.
19. Mateos, J. L. (2002). Current reversals in deterministic ratchets: points and dimers. *Physica D: Nonlinear Phenomena*, 16817169(0):205 – 219. {VII} Latin American Workshop on Nonlinear Phenomena.
20. Mateos, J. L. and Alatrliste, F. R. (2008). Phase synchronization in tilted inertial ratchets as chaotic rotators. *Chaos*, 18:043125.

21. Mathwig, K., Müller, F., and Gösele, U. (2011). Particle transport in asymmetrically modulated pores. *New Journal of Physics*, 13(3):033038.
22. Matthias, S. and Müller, F. (2003). Asymmetric pores in a silicon membrane acting as massively parallel brownian ratchets. *Nature*, 424:53–57.
23. McNeil, B. W. J. and Thompson, N. R. (2010). X-ray free-electron lasers. *Nat Photon*, 4(12):814–821.
24. Pitkovsky, A., Rosenblum, M., and Kurths, J. (2001). *Synchronization. A Universal Concept in Nonlinear Sciences*. Cambridge University Press.
25. Pototsky, A., Archer, A. J., Savel’ev, S. E., Thiele, U., and Marchesoni, F. (2011). Ratcheting of driven attracting colloidal particles: Temporal density oscillations and current multiplicity. *Phys. Rev. E*, 83:061401.
26. Speer, D., Eichhorn, R., and Reimann, P. (2007). Transient chaos induces anomalous transport properties of an underdamped brownian particle. *Phys. Rev. E*, 76:051110.
27. Spiechowicz, J., Hänggi, P., and Luczka, J. (2013). Absolute negative mobility of inertial Brownian particles induced by noise *IEEE 22nd International Conference on Noise and Fluctuations, 24-28 June 2013, Montpellier, France*, 370:446–447.
28. Swift, J. W. and Wiesenfeld, K. (1984). Suppression of period doubling in symmetric systems. *Phys. Rev. Lett.*, 52:705–708.
29. Vincent, U. E., Njah, A. N., Akinlade, O., and Solarin, A. R. T. (2004). Phase synchronization in unidirectionally coupled chaotic ratchets. *Chaos*, 14:1018–1025.
30. Wickenbrock, A., Cubero, D., Wahab, N. A. A., Phoonthong, P., and Renzoni, F. (2011). Current reversals in a rocking ratchet: The frequency domain. *Phys. Rev. E*, 84:021127.

Predictability of a system with transitional chaos

Marek Berezowski

Silesian Univesristy of Technology, Faculty of Applied Mathematics, Gliwice, Poland
(E-mail: marek.berezowski@polsl.pl)

Abstract. The paper is focused on the discussion of the phenomenon of transitional chaos in dynamic autonomous and non-autonomous systems. This phenomenon involves the disappearance of chaotic oscillations in specific time periods and the system becoming predictable. Variable dynamics of the system may be used to control the process. The discussed example concerns a model of a chemical reactor.

Keywords: Chaos, Chemical Reactor, Oscillations, Time series, Lyapunov time.

1 Introduction

Unpredictability is characteristic for a chaos. It means, that even the smallest change in initial conditions causes that we are unable to predict what will happen in the future. The greater change, the shorter the Lyapunov time (predictability). However, there are completely opposite cases, that is: we are unable to predict what happen in a moment, but we can say what happen in farther future with 100% accuracy.

It is probable that this feature is embedded in the Universe and nature. Due to a chaotic nature of the Universe, we are not even capable of predicting the weather prevailing on the Earth, or the movement of the galaxies, yet we forecast that in the far future the Universe will shirk again back to the unique point and shall be predictable. It is similar with nature. Until an entity lives, it is difficult to predicts its behavior, but when it dies, its condition is explicitly determined within the framework of time. Thus, we may say what will happen to an entity/ individual in the far future, yet, we may not foresee what will happen to them in a moment of time. It occurs in systems with variable dynamics. There may be autonomous or non-autonomous systems. Under certain conditions the phenomenon of variable dynamics may be used to predict chaotic changes and to control a given process.



2 Autonomous system

An example of the autonomous system can be two-dimensional discrete model:

$$\begin{aligned} x_{k+1} &= rx_k \left(1 - x_k - \frac{0.001}{y_k} \right) \\ y_{k+1} &= \frac{r}{2.1} (1 - x_k^2) \end{aligned} \quad (1)$$

See Fig. 1.

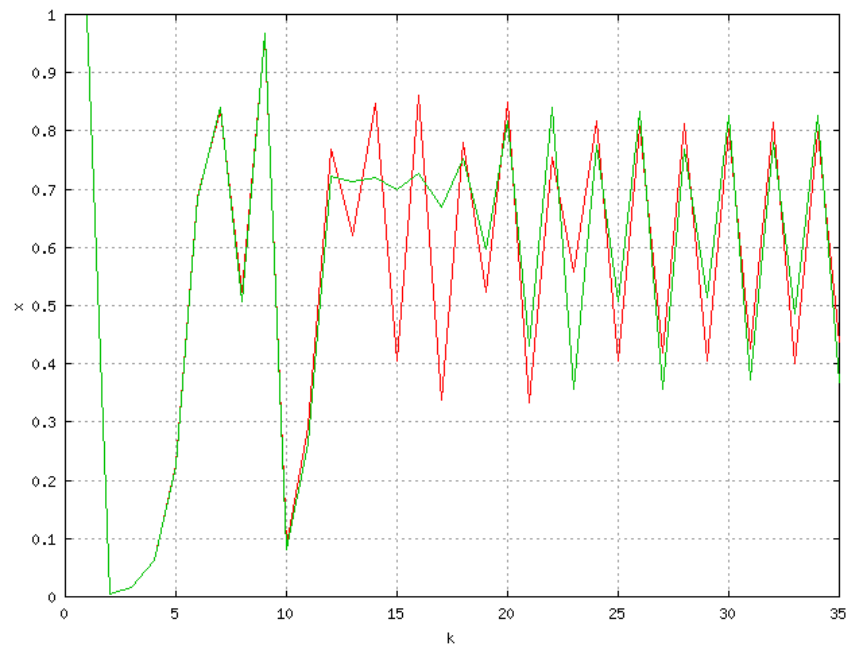


Fig. 1. Two time series of the autonomous system (1). Continuous line – first plot, dashed line – second plot

Two trajectories start at slightly different initial conditions, and, for $k < 12$ they are practically convergent. For $k > 12$; however, the trajectories become distant from each other. This is a typical feature of chaos. Yet, for $k > 26$ both trajectories are again approaching each other and from that moment the system generates stable (predictable) four-period oscillations.

A similar phenomenon may occur in different types of industrial systems and equipment. A good example of this is a chemical reactor in which the so called catalyst deactivation takes place. Due to such deactivation the reactor slowly halts, and after some time, stops working at all. If such process is

considered in a mathematical model of the reactor, and described by means of additional differential equations, we are dealing with an autonomous model. If, however, the deactivation process is explicitly dependent on time, we are dealing with a non-autonomous model.

3 Non- autonomous system

An example of a non-autonomous model is a chemical reactor with mass recycle, in which the following reaction kinetics variable in time was assumed:

$$\begin{aligned}\frac{\partial a}{\partial \tau} + \frac{\partial \alpha}{\partial \xi} &= (1-f)\phi(\alpha, \Theta) \\ \frac{\partial \Theta}{\partial \tau} + \frac{\partial \Theta}{\partial \xi} &= (1-f)\phi(\alpha, \Theta) + (1-f)\delta(\Theta_H - \Theta) \\ \alpha(\tau, 0) &= f\alpha(\tau, 1); \Theta(\tau, 0) = f\Theta(\tau, 1) \\ \phi(\alpha, \Theta) &= Da(1-\alpha)^n e^{\frac{\gamma\Theta}{1+\beta\Theta}} (e^{-\omega_1 k} - e^{-\omega_2 k})\end{aligned}\quad (2)$$

where: $f=0.5$, $\delta=3$, $\Theta_H=-0.025$, $Da=0.15$, $n=1.5$, $\gamma=15$, $\beta=2$, $\omega_1=0.00025$, $\omega_2=0.0075$ and k is a discrete time. See Fig. 2.

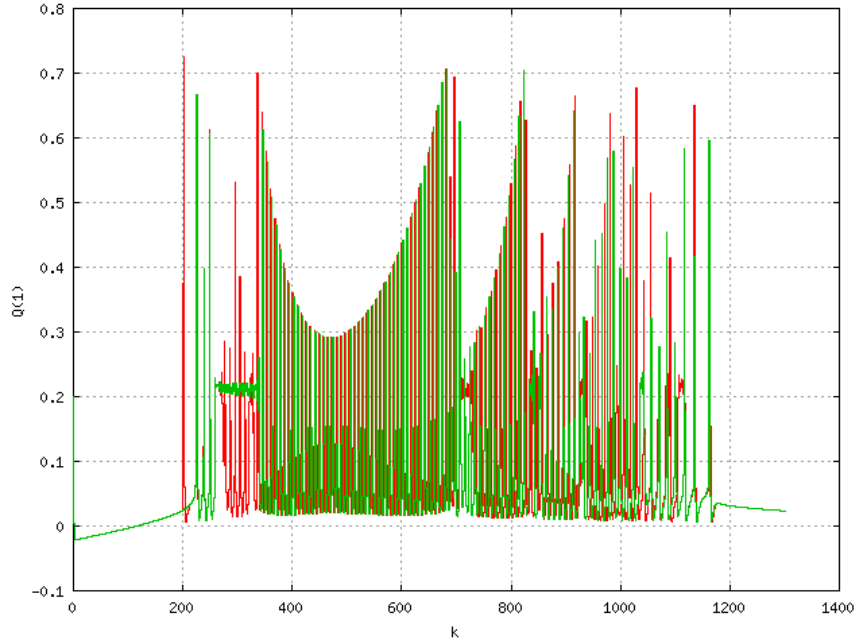


Fig. 2. Two time series of the chemical reactor model (2). Perturbation for $k=200$. Continuous line – first plot, dashed line – second plot

Likewise, two trajectories start at only slightly different initial conditions, and, for $k < 250$ they are practically convergent. But, for $k > 250$ they are becoming divergent, which is a typical feature of chaos. For the range of $340 < k < 680$ the process becomes completely predictable, see Fig. 3.

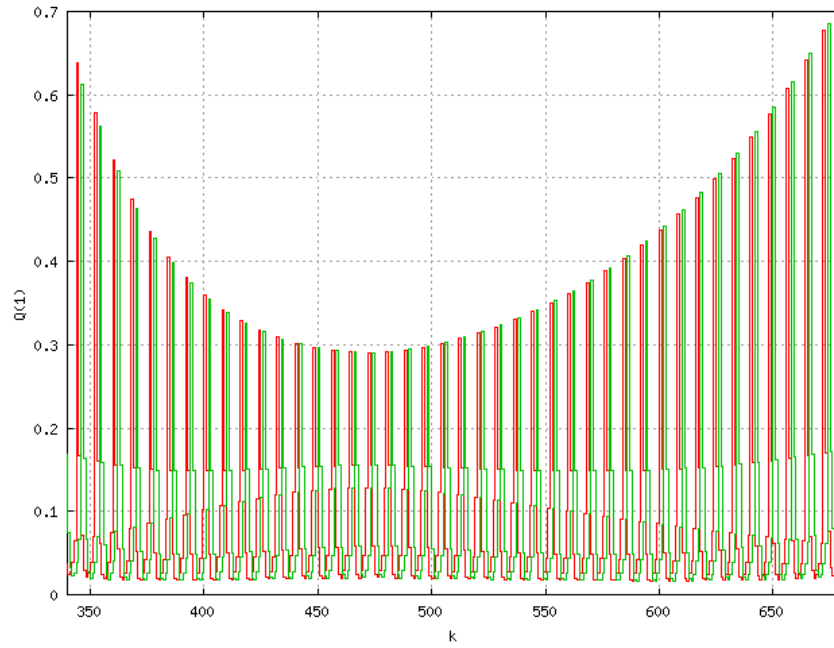


Fig. 3. Part of Fig. 2.

For $680 < k < 1180$ chaos reappears and the resultant unpredictability (chaotic crisis). For $k > 1180$ the system enters the steady state and again becomes predictable. In Fig.4 Poincaré section is shown for the function in Fig. 2. This is Henon characteristic attractor, designated for a reactor with recycle-see [1-12].

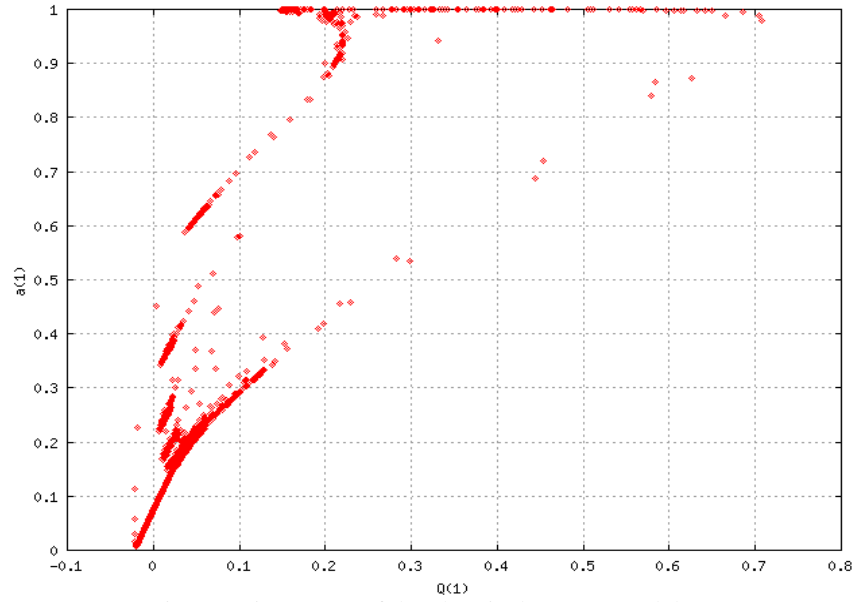


Fig. 4. Poincaré set of the chemical reactor model (2)

It is noteworthy that for perturbation in time $k < 200$ does not evoke changes in the further course of the process. See Fig. 5.

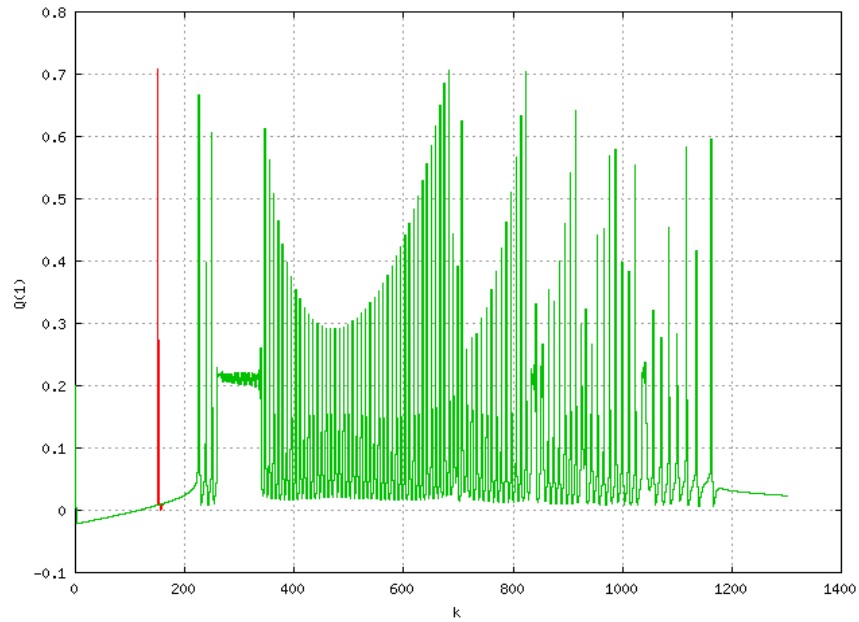


Fig. 5. Two time series of the chemical reactor model (2). Perturbation for $k=150$. Continuous line – first plot, dashed line – second plot

The phenomenon of variable dynamics may be used to predict chaos and, in consequence, enable process control. Let us assume the following kinetics form of the reaction:

$$\phi(\alpha, \Theta) = Da(1 - \alpha)^n e^{\gamma \frac{\beta \Theta}{1 + \beta \Theta}} e^{-\frac{\omega}{k}} \quad (3)$$

If, under normal process conditions, i.e. for $\omega = 0$, the reactor works in a chaotic manner, then, assuming $\omega \neq 0$, the value of function ϕ is close to zero for small values of time k . This means that during the first time interval, the reactor works in a predictable manner. During the start-up the values of the reactor state variables (temperature and concentration) are the same for both trajectories, irrespective of the difference in their initial conditions. As shown in Fig. 6, for $\omega = 20$ even a significant perturbation in time $k=10$ does not evoke changes in the further course of the process.

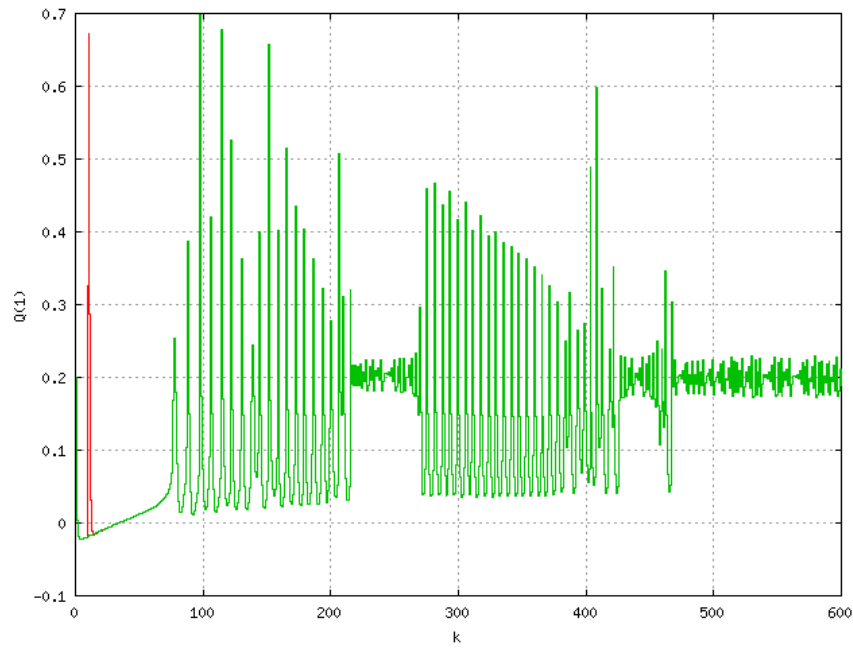


Fig. 6. Two time series of the chemical reactor model (3). Perturbation for $k=10$. Continuous line – first plot, dashed line – second plot

This means that such chaotic process does not react to changes in its initial conditions, thus, it is predictable.

The occurrence of a disturbance in time $k > 10$ does not lead to changes in the beginning for a significantly long time period. However, the changes appear in longer time perspective, as shown in Fig. 7.

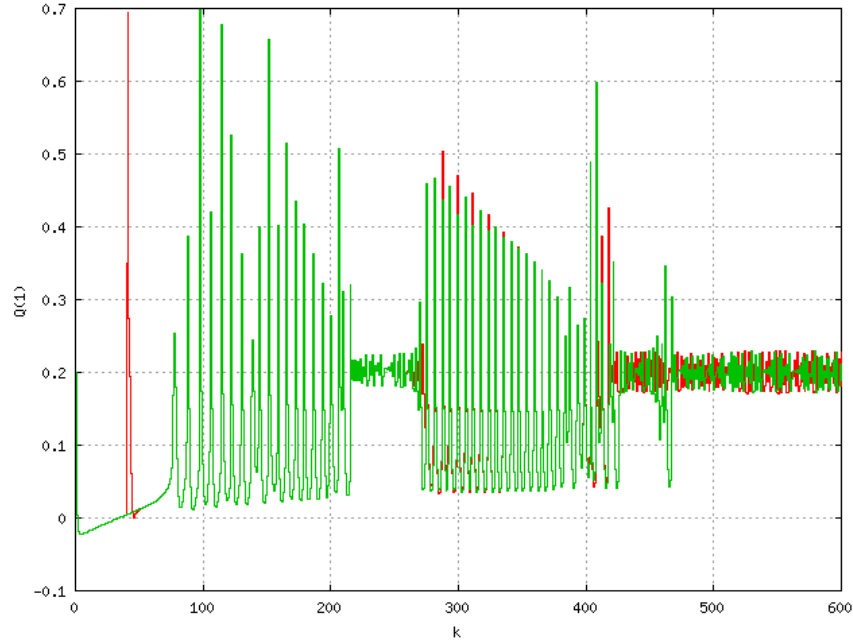


Fig. 7. Two time series of the chemical reactor model (3). Perturbation for $k=40$.
Continuous line – first plot, dashed line – second plot

Accordingly, the excitation of non-chaotic operation of the reactor at start-up may guarantee the predictability of the process in its further course. This may be useful in circumstances when the reactor is required to work chaotically, yet at the same time, under control.

Conclusions

The scope of the paper is the analysis of the phenomenon of transitory chaos in dynamic autonomous and non-autonomous systems. In the autonomous system chaos occur in a transitory state and then disappears in the steady state. Accordingly, the state of the system is unpredictable at the beginning of the observations, but predictable in the longer time period. Likewise, in a non-autonomous model explicitly dependent on time. Such case was considered on the example of a model of a chemical reactor. The phenomenon of variable dynamics may be used to predict chaotic behaviour of systems, which, in turn, enables their control.

The system (2) remembers the initial conditions for $k < 200$. The system (3) remembers the initial conditions for $k < 10$. We can say that these are special times of Lapunov.

References

1. P. Altimari and C.S Bildea C.S. Coupling Exothermic and Endothermic Reactions in Plug-Flow Reactor–Separation–Recycle Systems, *Industrial and Engineering Chemistry Research*, 47, 6685{6697, 2008.
2. C. Antoniadis and P.D. Christofides P.D. Studies on Nonlinear Dynamics and Control of a Tubular Reactor with Recycle, *Nonlinear Analysis - Theory Methods and Applications*, 47, 5933{5944, 2001.
3. M. Berezowski. Spatio-temporal chaos in tubular chemical reactors with the recycle of mass, *Chaos, Solitons & Fractals*, 11, 1197{1204, 2000.
4. M. Berezowski. Effect of delay time on the generation of chaos in continuous systems. One-dimensional model.. Two-dimensional model - tubular chemical reactor with recycle, *Chaos, Solitons & Fractals*, 12, 83{89, 2001.
5. M. Berezowski. Fractal solutions of recirculation tubular chemical reactors. *Chaos, Solitons & Fractals*, 16, 1{12, 2003.
6. M. Berezowski and K. Bizon. Fractal structure of iterative time profiles of a tubular chemical reactor with recycle. *Chaos, Solitons & Fractals*, 28, 1046{1054, 2006.
7. M. Berezowski. Crisis phenomenon in a chemical reactor with recycle, *Chemical Engineering Science*, 101, 451{453, 2013.
8. M. Berezowski and D. Dubaj. Chaotic oscillations of coupled chemical reactors. *Chaos, Solitons & Fractals*, 28: DOI: 10.1016/j.chaos.2015.07.001, 2015 (in print).
9. E.W. Jacobsen and M. Berezowski. Chaotic dynamics in homogeneous tubular reactors with recycle, *Chemical Engineering Science*, 53, 4023{4029, 1998.
10. D. Luss D. and N.R. Amundson. Stability of loop reactors, *A.I.Ch.E. J.*, 13, 279{290, 1966.
11. M.J. Reilly and R.A. Schmitz. Dynamics of a tubular reactor with recycle. Part I. *A.I.Ch.E. J.*, 12, 153{161, 1966.
12. M.J. Reilly and R.A. Schmitz. Dynamics of a tubular reactor with recycle. Part II. *A.I.Ch.E. J.*, 13, 519{527, 1967.

Relative dispersion and turbulence in the Southwestern Atlantic Ocean from drifters data

Stefano Berti¹ and Francisco Alves dos Santos²

¹ Laboratoire de Mécanique de Lille, CNRS/FRE 3723, Université de Lille, F-59000 Lille, France (E-mail: stefano.berti@polytech-lille.fr)

² PROOCEANO Serviço Oceanográfico, Rio de Janeiro, Brazil

Abstract. Lagrangian data can provide relevant information on the advection and diffusion properties of geophysical flows at different scales of motion. In this study, the dispersion properties of an ensemble of trajectories transported by a surface ocean flow are analyzed. The data come from a set of Lagrangian drifters released in the South Brazilian Bight, during several oceanographic campaigns. Adopting a dynamical systems approach, the attention is primarily focused on scale-dependent indicators, like the finite-scale Lyapunov exponent. The relevance of mechanisms like two-dimensional turbulence for the dispersion process is addressed. Some deviations from the classical turbulent dispersion scenario in two-dimensions are found, likely to be ascribed to the nonstationary and nonhomogeneous characteristics of the flow. Relatively small-scale features (of order 1-10 km) are also considered to play a role in determining the properties of relative dispersion as well as the shape of the kinetic energy spectrum.

Keywords: Turbulent transport, Lagrangian dispersion, Geophysical flows, Oceanic turbulence.

1 Introduction

Experimental campaigns involving Lagrangian drifters provide useful information to test model and theories of geophysical fluid dynamics, as well as to characterize the advection and diffusion properties of flows in applications. In an oceanographic context, for instance, predicting the spreading of a pollutant or the distribution of a biological population (e.g., phytoplankton or fish larvae) transported by surface currents represent both a challenging scientific task and a matter of general interest.

In the past years, an amount of Lagrangian data about the South Atlantic Ocean (SAO) was collected thanks to the First GARP Global Experiment drifters, released following the major shipping lines, and to the Southern Ocean Studies drifters, deployed in the Brazil-Malvinas Confluence. These data allowed estimates of eddy kinetic energy, integral time scales and diffusivities [1,2]. Despite the relatively uniform coverage, the boundary currents resulted poorly populated by buoys. Furthermore, the majority of previous

8th CHAOS Conference Proceedings, 26-29 May 2015, Henri Poincaré Institute, Paris France



studies about drifters in the South Atlantic have concerned one-particle statistics only. While single-particle statistics give information on the advective transport associated to the largest and most energetic scales of motion, two (or more) particle statistics are needed to access information about the dominant physical mechanism acting at a certain scale of motion (chaotic advection, turbulence, diffusion). In a previous study [3], we considered both one and two-particle statistics to investigate the advective and diffusive properties of the surface currents explored by an ensemble of drifters released in proximity of the coast of Brazil during a project called MONDO (Monitoring by Ocean Drifters), for the environmental assessment on an oil drilling operation. The analysis of trajectory pair dispersion revealed some deviations, at scales smaller than approximately 10 km, from the behavior expected within a classical two-dimensional (2D) turbulence scenario. Interestingly, such deviations suggest that motions in this range of scales would be more energetic than predicted by 2D turbulence. However, due to limited statistics, the results were not conclusive, i.e. no clear scaling behavior of appropriate statistical indicators was detected below 10 km.

In this study we revisit the analysis of trajectory pair dispersion in the Southwestern Atlantic Ocean using a larger data set, corresponding to drifter trajectories coming from environmental assessment projects of oil drilling operations (including the first MONDO project) and Projeto AZUL [4], a pilot operational oceanography program in the region. The main goal of the present work is to attempt making a step forward in the understanding of relative dispersion at scales smaller than 10 km, and discuss the consistency of the data analysis with classical turbulence theory predictions. The paper is organized as follows. In Section 2 we recall the classical picture of turbulent dispersion and we introduce the statistical indicators of Lagrangian dispersion that we will consider. In Section 3 we provide a description of the data set. In Section 4 we report the results of our data analysis, and in Sec. 5 we compare it with that issued from numerical simulations of the Lagrangian dispersion process. Finally, in Section 6 we provide some concluding remarks.

2 Turbulence and relative dispersion

In the quasi-geostrophic (QG) approximation, valid for relative vorticities much smaller than the ambient vorticity due to the Earth's rotation, theoretical arguments would predict that, from the scale of the forcing at which eddies are efficiently generated by instability, e.g. the Rossby radius of deformation δ_R , both a down-scale enstrophy cascade and an up-scale energy cascade take place. The corresponding energy spectra are respectively given by $E(k) \sim k^{-3}$ (for $k > k_R$) and $E(k) \sim k^{-5/3}$ (for $k < k_R$) [5,6], where k is the horizontal wavenumber and $k_R = 2\pi/\delta_R$. In the ocean, possible deviations from this ideal double-cascade scenario may come, reasonably, from the nonhomogeneous and nonstationary characteristics of the velocity field, e.g. in the case of boundary currents, as well as from ageostrophic effects. At this regard, one presently debated issue is the role of submesoscale structures [7], velocity field features

of size $\sim (1-10)$ km, in determining the shape of the energy spectrum at intermediate scales between the Rossby deformation radius, in the ocean typically $\sim (10-50)$ km, and the dissipative scales (much smaller than 1 km). It is worth observing, here, that recent high-resolution 3D simulations of upper-ocean turbulence [8,9] have shown that the direct cascade energy spectrum flattens from k^{-3} to k^{-2} at submesoscales.

Let us now see how different transport mechanisms, like the turbulent phenomenology described above, manifest in a Lagrangian framework, particularly from a relative dispersion perspective. Relative dispersion is defined as the second order moment of the distance $R(t) = \|\mathbf{r}^{(1)}(t) - \mathbf{r}^{(2)}(t)\|$, at time t , between two trajectories:

$$\langle R^2(t) \rangle = \langle \|\mathbf{r}^{(1)}(t) - \mathbf{r}^{(2)}(t)\|^2 \rangle, \quad (1)$$

where the average is over all the available trajectory pairs $(\mathbf{r}^{(1)}, \mathbf{r}^{(2)})$. At scales smaller than the forcing scale, $\delta < \delta_R$, the presence of a direct enstrophy cascade implies that the velocity field varies smoothly in space. This means that, for nonlinear fields, the particle pair separation typically evolves following an exponential law:

$$\langle R^2(t) \rangle \sim e^{2\lambda_L t}, \quad (2)$$

where λ_L is the (Lagrangian) maximum Lyapunov exponent [10]; a value $\lambda_L > 0$ means Lagrangian chaos. The chaotic regime holds as long as the trajectory separation remains sufficiently smaller than the characteristic scale δ_R . Under these conditions, relative dispersion is often referred to as a nonlocal process because it is mainly driven by the deformation field at scales much larger than the particle separation. When $\delta > \delta_R$, on the other hand, the presence of an inverse energy cascade with spectrum $E(k) \sim k^{-5/3}$ implies a rough velocity field; in this case one expects

$$\langle R^2(t) \rangle \sim t^3, \quad (3)$$

that is Richardson superdiffusion [11]. This dispersion regime is said to be local, because the growth of the distance between two particles is now controlled by local velocity differences, i.e. mean gradients on a finite scale of the order of the particle separation. In the limit of very large particle separations, namely larger than any scale of motion, the two trajectories are sufficiently distant from each other to be considered uncorrelated and the mean square relative displacement behaves like:

$$\langle R^2(t) \rangle \simeq 4K_E t, \quad \text{for } t \rightarrow \infty \quad (4)$$

where K_E is the asymptotic eddy-diffusion coefficient [11]. At any time t , the diffusivity $K(t)$ can be defined as:

$$K(t) = \frac{1}{4} \left\langle \frac{dR^2}{dt}(t) \right\rangle = \frac{1}{2} \left\langle R(t) \frac{dR}{dt}(t) \right\rangle \quad (5)$$

with $K(t) \rightarrow K_E$ for $t \rightarrow \infty$.

Relative dispersion is a fixed-time indicator. This involves averaging, at a given time, particle separations that can be very different, which can be problematic for multiscale turbulent flows, especially in a local dispersion regime.

Another approach, allowing to disentangle contributions to the dispersion process from different scales, is to resort to indicators that are, instead, computed as fixed-scale averages. The finite-scale Lyapunov exponent (FSLE) has been formerly introduced as the generalization of the maximum Lyapunov exponent (MLE) λ for non-infinitesimal perturbations [12]. If δ is the size of the perturbation on a trajectory in the phase space of a system, and $\langle\tau(\delta)\rangle$ is the phase space averaged time that δ takes to be amplified by a factor $\rho > 1$, then the FSLE is defined as

$$\lambda(\delta) = \frac{1}{\langle\tau(\delta)\rangle} \ln \rho. \quad (6)$$

The quantity $\tau(\delta)$ is the exit time of the perturbation size from the scale δ , and it is defined as the first arrival time to the scale $\rho \cdot \delta$, with $\rho \sim O(1)$. The evolution equations of Lagrangian trajectories form a dynamical system whose phase space is the physical space spanned by the trajectories. In this context, the analysis of relative dispersion can be treated as a problem of finite-size perturbation evolution, with scale-dependent growth rate measured by the FSLE. By a dimensional argument, if relative dispersion follows a $\langle R^2(t) \rangle \sim t^{2/\beta}$ scaling law, then the FSLE is expected to scale as $\lambda(\delta) \sim \delta^{-\beta}$. For example, in case of standard diffusion we expect $\beta = 2$; for Richardson superdiffusion, $\beta = 2/3$; in ballistic or shear dispersion we have $\beta = 1$. Chaotic advection means exponential separation between trajectories, which amounts to a scale-independent FSLE $\lambda(\delta) = \text{constant}$, i.e. $\beta \rightarrow 0$. In the limit of infinitesimal separation, the FSLE is nothing but the MLE, i.e. $\lambda(\delta) \simeq \lambda_L$.

An indicator related to the FSLE is the mean square velocity difference between two trajectories as function of their separation. Indicating with $\mathbf{r}^{(1)}$, $\mathbf{r}^{(2)}$, $\mathbf{v}^{(1)}$, $\mathbf{v}^{(2)}$ the positions and the Lagrangian velocities of two particles 1 and 2 at a given time, we define the finite-scale relative velocity (FSRV) at scale δ ,

$$\langle[\Delta V(\delta)]^2\rangle = \langle[\mathbf{v}^{(1)} - \mathbf{v}^{(2)}]^2\rangle \quad (7)$$

where the average is over all trajectory pairs fulfilling the condition $R(t) = \|\mathbf{r}^{(1)}(t) - \mathbf{r}^{(2)}(t)\| = \delta$ at some time t . From the FSRV a scale-dependent diffusivity can be formed as $K(\delta) = (1/2)\delta\langle[\Delta V(\delta)]^2\rangle^{1/2}$ and compared to the classical time-dependent diffusivity $K(t)$ defined in (5).

3 Drifter data set

The data used in this study come from a set of 175 satellite-tracked ocean drifters deployed at Campos and Santos Basins - Southeastern Brazil - for environmental assessments of oil and gas activities (MONDO projects), and from Projeto AZUL [4], a pilot operational oceanography project for the region. The period of analysis ranges from September 2007 to September 2014. Deployments carried out during MONDO projects occurred from 2007 to 2012 (with the exception of 2008), while deployments from Projeto AZUL started in 2013. Part of the drifters were deployed in clusters of 3 to 5 units, with initial pair separations smaller than 1 km, in order to study dispersion properties (as

performed in [3]). Other deployments were targeted at dynamic features of the region like eddies and meanders and consisted in releasing either a single buoy at a time or groups with greater initial pair separations. All drifters are of SVP (Surface Velocity Program) type [13], with an underwater drogue attached to a surface buoy, an arrangement designed to minimize wind slippage and to represent the average current of the top 20-m layer of the ocean. Each drifter is equipped with a GPS device and iridium communication, allowing for a 7 m accuracy of the position and a fixed 3 h acquiring rate. Data were quality controlled as proposed by the Global Drifter Program [14] to remove spurious values and to assure that trajectories pertain to the period when the drifter was in the water and with the drogue attached. Resulting trajectory durations vary from 30 to 671 days, with a mean of 180 days and a standard deviation of 132 days. In order to remove high-frequency components, a Blackman low-pass filter of 25 h was applied to the data. Despite the heterogeneity of the deployment strategies and frequency, the 175 trajectories analyzed provide a rather good sampling of the southwestern corner of the South Atlantic gyre and suffice for two-particle statistics studies. Trajectories and deployment locations are presented in Fig. 1.

The domain explored by the drifters mainly corresponds to that of the southward flowing Brazil Current and to the area where this meets the northward flowing Malvinas Current, forming the Brazil-Malvinas Confluence, a highly energetic zone playing an important role in weather and climate of South America. More details about the local oceanography can be found in [3] and references therein. Here we only recall that this is an area of intense mesoscale activity with eddies detaching from both sides of the flow and that the first internal Rossby radius of deformation has a meridional variation in the range (20 – 40) km, in the region.

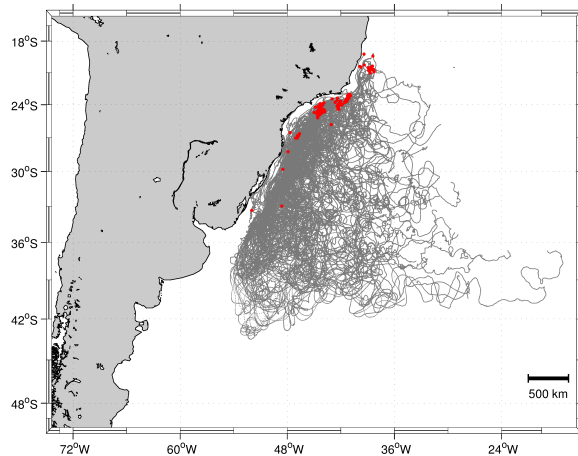


Fig. 1. Overall view of drifter trajectories. The larger red dots indicate the Lagrangian origins of trajectories.

4 Analysis of two-particle statistics

In this section we present the results of the data analysis on two-particle statistics. Distances between two points on the ocean surface are calculated as great circle arcs, according to the spherical geometry standard approximation. The available statistics is limited by finite lifetime of trajectories and irregular deployments of drifters in time. Hence, in order to increase the statistics, besides the original pairs we also consider chance pairs, that is pairs that happen to be sufficiently close to each other at an arbitrary instant of time after their release [15].

Relative dispersion is reported in the left panel of Fig. 2 for three different initial separations. The numbers of pairs counted in the statistics depends on the initial threshold: 64 for $R(0) \leq 2$ km, 77 for $R(0) \leq 5$ km and 91 for $R(0) \leq 10$ km. The dependence of $\langle R^2(t) \rangle$ on $R(0)$ is well evident. The early regime is shown in the right panel and it does not display any clear exponential growth of $\langle R^2(t) \rangle$. In the opposite limit of very large times, corresponding to separations $\delta \geq (250 - 300)$ km, some tendency towards a linear scaling, indicating diffusive behavior, is found. In the intermediate range between these two, the scaling of relative dispersion is not far from t^3 , as for Richardson superdiffusion, but the growth is somehow smaller.

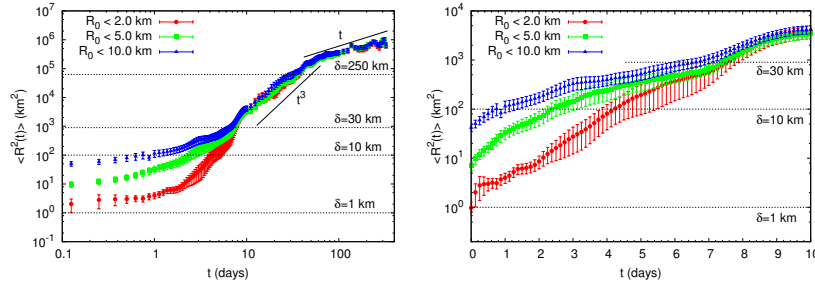


Fig. 2. Drifter relative dispersion $\langle R^2(t) \rangle$ (left panel) and its early regime (right panel) for initial separations as in the legend. The time sampling is $\Delta t = 1/8$ day. Error bars are the standard deviations.

Relative diffusivity in the zonal and meridional directions, for $R(0) \leq 2$ km, is plotted in Fig. 3. In the intermediate time range between 10 and 100 days the behavior of $K(t)$ approaches a t^2 law, as expected in the Richardson dispersion regime. The diffusivity in the meridional direction is found to be larger, reflecting the anisotropy of the flow.

We now present the results obtained with fixed-scale indicators. These have been evaluated for the same initial thresholds, $R(0) \leq 2, 5, 10$ km. The density of scales is fixed by setting $\rho = 1.3$ or $\rho = \sqrt{2}$, representing a good compromise between the finest possible scale resolution and the largest possible number of pairs per threshold to ensure convergence of the statistics. The results do not strongly depend on the precise value of the amplification factor. The maximum

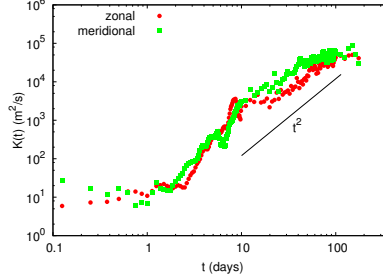


Fig. 3. Drifter relative diffusivity $K(t)$ for zonal and meridional components, for initial separations $R(0) \leq 2$ km. The t^2 scaling corresponds to the Richardson regime. The time sampling is $\Delta t = 1/8$ day.

number of pairs considered varies with the initial threshold: 64 for $R(0) \leq 2$ km, 77 for $R(0) \leq 5$ km, 90 for $R(0) \leq 10$ km.

The FSLE is plotted in Fig. 4; the comparison of left and right panels ($\rho = 1.3$ and $\rho = \sqrt{2}$, respectively) clearly shows the robustness of results with respect to the value of ρ . In the mesoscale range $\delta > \delta_R$ above the deformation radius, here reasonably estimated as $\delta_R \simeq 30$ km, the FSLE exhibits a power law scaling $\delta^{-2/3}$ compatible with Richardson superdiffusion and local dispersion. At scales of the order of the deformation radius $\delta \approx \delta_R$, the FSLE is close to a constant value $\lambda(\delta) \simeq 0.15 \text{ day}^{-1}$, suggesting exponential separation and a less local dispersion process. These results are in good agreement with those previously found, in the same scale ranges, using data from the first MONDO project [3]. In principle, they could support a classical double-cascade scenario with $k^{-5/3}$ and k^{-3} kinetic energy spectra in the inverse energy cascade and in the direct enstrophy cascade, respectively. However, in the submesoscale range $\delta \simeq (1 - 10)$ km well below δ_R we find a behavior close to $\lambda(\delta) \sim \delta^{-1/2}$, implying enhanced scale-dependent dispersion rates. We observe, furthermore, that such a power-law scaling of the FSLE would correspond to a rather flat kinetic energy spectrum in k^{-2} . At the smallest sampled scales ($\delta < 1$ km) the FSLE tends to level off, which is more clearly seen for $\rho = 1.3$ (left panel of Fig. 4). However, we remark that on these scales the resulting values are likely affected by poorer statistics and filtering issues (the time scale $1/\lambda(\delta) \approx 1$ day is of the order of the filtering time window of 25 h).

The computation of the mean square finite size relative velocity is reported in Fig. 5 (left panel). The Lagrangian velocity components are obtained from the drifter trajectories by a standard finite differencing method. The FSRV is consistent with Richardson dispersion for scales larger than the Rossby radius, where it scales as $\delta^{2/3}$. In a rather narrow intermediate range ($\delta \approx \delta_R$) it gets closer to a δ^2 behavior, suggesting exponential separation. In the submesoscale range (1–10) km, on the other hand, it appears to scale as δ , which is consistent with a k^{-2} kinetic energy spectrum and the FSLE behavior found in the same scale range. These results support a classical double-cascade phenomenology only at scales comparable to the Rossby radius or larger, while they suggest more energetic submesoscales well below δ_R . From the FSRV an “equivalent

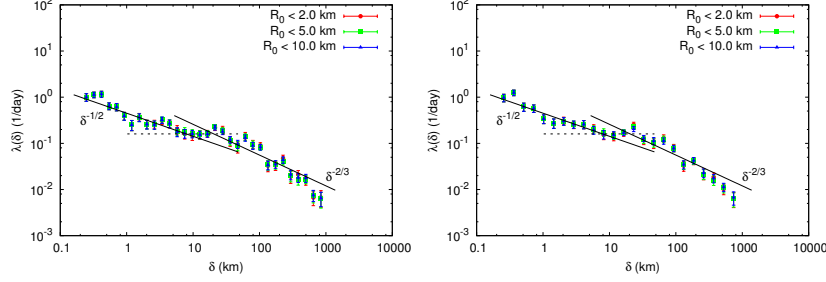


Fig. 4. FSLE for different values of $R(0)$, as in the legend, and amplification factor $\rho = 1.3$ (left panel) and $\rho = \sqrt{2}$ (right panel). The $\delta^{-2/3}$ and $\delta^{-1/2}$ scalings respectively correspond to Richardson law and a k^{-2} spectrum. The horizontal dashed line corresponds to $\lambda(\delta) \simeq 0.15 \text{ day}^{-1}$. Error bars are the standard deviations of the mean values.

Lagrangian spectrum” $E_L(k) = \langle [\Delta V(k)]^2 \rangle / k$ can be dimensionally defined replacing δ with $2\pi/k$. This quantity returns the same picture, in k space, as that found with the FSRV (Fig. 5, right panel).

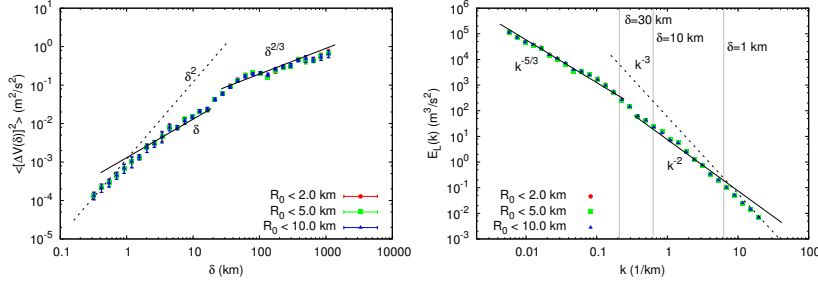


Fig. 5. Left: FSRV computed together with the FSLE. The scalings δ^2 , δ and $\delta^{2/3}$ correspond to k^{-3} , k^{-2} and $k^{-5/3}$ energy spectra, respectively. Error bars are the standard deviations of the mean values; here $\rho = 1.3$. Right: Equivalent Lagrangian spectrum defined from the FSRV. The Rossby radius $\delta_R \simeq 30 \text{ km}$ corresponds to wavenumber $k \simeq 0.2$.

Finally, in Figure 6 we compare the diffusivity computed as a fixed-time average, Eq. (5), with that computed as a fixed-scale average from the FSRV. Both quantities are plotted as function of the separation between two drifters: $K(\delta) = (1/2)\delta\langle[\Delta V(\delta)]\rangle^{1/2}$ with δ as the independent variable, and $K(t)$ versus $\delta = \langle R^2(t) \rangle^{1/2}$ where the independent variable is the time t . The $\delta^{4/3}$ regime in the mesoscales range and the δ^2 one in the narrow intermediate range $\delta \approx \delta_R$ (here less evident than with other indicators) are respectively consistent with Richardson superdiffusion and nonlocal dispersion. Hence, they may support the presence of an inverse cascade with $E(k) \sim k^{-5/3}$ (at scales $\delta > \delta_R$) and a direct cascade with $E(k) \sim k^{-3}$ (at scales $\delta \approx \delta_R$), as predicted by QG turbulence theory. Nevertheless, the $\delta^{3/2}$ scaling, corresponding to a k^{-2} spectrum, found for $\delta \simeq (1 - 10) \text{ km}$ confirms that dispersion is local in this

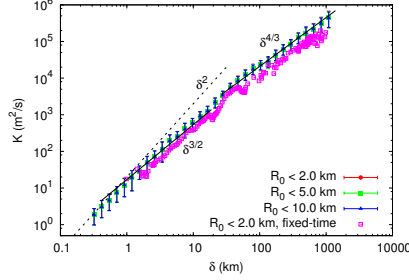


Fig. 6. Diffusivity as a function of the separation: fixed-time average $K(t)$ vs $\delta = \langle R^2(t) \rangle^{1/2}$ and fixed-scale average $K(\delta)$ vs δ . The $\delta^{4/3}$, $\delta^{3/2}$ and δ^2 correspond to $k^{-5/3}$, k^{-2} and k^{-3} spectra, respectively.

scale range and that submesoscales are more energetic than expected in a direct enstrophy cascade.

5 Numerical results

We now compare the results of the drifter data analysis with those issued from numerical simulations of the Lagrangian dispersion process in the same geographical area in the period 20/9/2007-21/10/2008 (corresponding to MONDO project). More details about the numerics can be found in [3]. Here we simply recall that $O(10^2)$ virtual trajectories are considered and that the spatial resolution of the model (HYCOM, see e.g. [16]) generating the advecting surface flow is approximately 7 km.

Two numerical experiments, that we indicate with E1 and E2, were conducted. In the first one (E1) the drifters are uniformly deployed in an area of about (10×10) km² centered around a position corresponding to the mean initial location of MONDO drifters. The average initial distance between synthetic particle pairs is $\langle R(0) \rangle \simeq 5$ km. The lifetime of trajectories is between 150 days and 200 days. In the second experiment (E2) the initial distribution of the drifters is characterized by larger separations, namely comparable to the spacing of the numerical grid (~ 10 km); the average initial distance between particle pairs is $\langle R(0) \rangle \simeq 40$ km and the duration of trajectories is (250 – 400) days.

For the comparison between the results obtained from real and model trajectories, here we focus on the FSLE and the FSRV, Fig. 7, but a similar picture is returned by other indicators too. To increase the statistics we now select trajectories with a larger initial separation: $R(0) < 50$ km (similar results are found for smaller values of $R(0)$, though they are more noisy). Moreover we set the amplification factor to $\rho = \sqrt{2}$. The behaviors of both FSLE and FSRV support a double-cascade scenario on scales comparable to those found with actual drifters. The plateau value of FSLE at scales $O(\delta_R)$ is very close to the one found in the real experiments, $\lambda(\delta) \simeq 0.15$ day⁻¹. At larger scales, for both numerical experiments E1 and E2 the behavior of FSLE is compatible with $\lambda(\delta) \sim \delta^{-2/3}$, supporting Richardson dispersion and an inverse energy

cascade process. Experiment E2, which is characterized by longer trajectories, shows a clearer scaling, thanks to a larger number of pairs reaching this range of large scales. Mean square velocity differences in the same range of scales display a reasonably clear $\delta^{2/3}$ scaling, also supporting an inverse energy cascade, with values close to those found with actual drifters. At separations smaller than the Rossby deformation radius, both indicators point to the presence of a direct enstrophy cascade: the FSLE is constant and the FSRV behaves as $\langle [\Delta V(\delta)]^2 \rangle \sim \delta^2$. This only partially agrees with the results found for real drifters, namely only in the scale range $10 \text{ km} < \delta < 30 \text{ km}$. At subgrid scales, velocity field features are not resolved and relative dispersion is necessarily a nonlocal exponential process driven by structures of size of the order of (at least) the Rossby radius. Correspondingly, the FSLE computed on model trajectories does not display the enhanced dispersion regime (with $\lambda(\delta) \sim \delta^{-1/2}$) at scales smaller than 10 km.

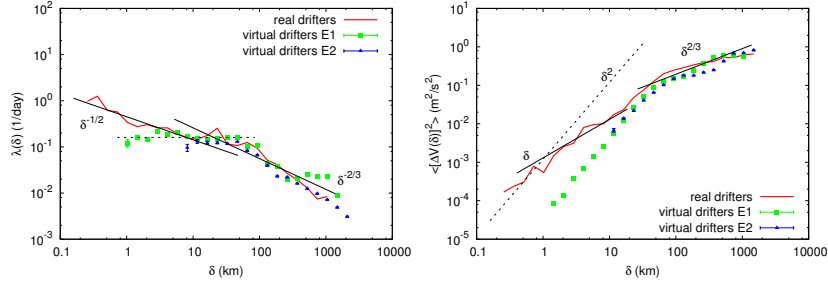


Fig. 7. FSLE (left panel) and FSRV (right panel) for $R(0) \leq 50 \text{ km}$ and $\rho = \sqrt{2}$ for real and virtual drifters from numerical experiments E1 and E2. For virtual drifters errors are on the order of point size. The large-scale saturation of the FSLE (E1) depends on the value of the trajectory integration time.

6 Conclusions

In this study we considered a set of surface drifter trajectories to analyse relative dispersion in the Southwestern Atlantic Ocean, by means of both fixed-time and fixed-scale statistical indicators. Fixed-time indicators, like the mean square displacement and the relative diffusivities as functions of the time lag from the release, point to a long-time regime compatible with Richardson superdiffusion, at least to some extent. As for the early regime of dispersion, no clear evidence of exponential separation is detected.

Scale-dependent indicators (FSLE, FSRV and related quantities) seem to more clearly reveal the different dispersion regimes, compatibly with the available statistics and the nonhomogeneous and nonstationary characteristics of the flow. In the mesoscale range $\delta \approx (30 - 300) \text{ km}$, both the FSLE and the FSRV display scaling behaviors compatible with Richardson superdiffusion and a 2D inverse energy cascade scenario. In a rather narrow range of scales close

to the Rossby radius of deformation $\delta_R \simeq 30$ km, a more nonlocal dispersion regime is found, indicative of exponential separation and, possibly, compatible with a 2D direct enstrophy cascade. However, at scales considerably smaller than δ_R , particularly for $\delta \approx (1 - 10)$ km, enhanced relative dispersion is observed, corresponding to the scaling $\lambda(\delta) \sim \delta^{-1/2}$ of the FSLE. Such a local dispersion regime suggests energetic submesoscale motions compatible with a kinetic energy spectrum $E(k) \sim k^{-2}$, as found in high-resolution numerical simulations of upper-layer ocean turbulence [8,9]. It is interesting to observe that evidences of increased dispersion rates and energetic submesoscales have been recently reported also in other studies based on Lagrangian drifter data, in different regions of the world oceans [17–19].

The data analysis was compared with the results of numerical simulations of the Lagrangian dynamics performed with a general circulation model. The comparison shows that the characteristics of the relative dispersion process found with real drifters are consistent with those obtained with virtual ones for scales $\delta \gtrsim \delta_R \simeq 30$ km. The model, however, fails to reproduce a local dispersion regime in the submesoscale range $(1 - 10)$ km, of course due to its finite spatial resolution (which is of the order of 10 km) and does not allow to address the dynamical role played by very small scale flow features.

We would like to conclude mentioning that further investigation on submesoscale processes would be extremely useful to clarify the origin of the observed deviations from classical QG turbulence. In particular, we believe that taking into account seasonality effects could allow to get more insight on relative dispersion at submesoscales in the region. This is left for future work.

References

1. H.A. Figueroa, D.B. Olson. Lagrangian statistics in the South Atlantic as derived from SOS and FGGE drifters. *J. Mar. Res.* **47**, 525–546 (1989).
2. H. Schäfer, W. Krauss. Eddy statistics in the South Atlantic as derived from drifters drogued at 100 m. *J. Mar. Res.* **53**, 403–431 (1995).
3. S. Berti, F. dos Santos, G. Lacorata, A. Vulpiani. Lagrangian drifter dispersion in the southwestern Atlantic Ocean. *J. Phys. Oceanogr.* **41**, 1659–1672 (2011).
4. F. dos Santos et al. Projeto Azul: operational oceanography in an active oil and gas area southeastern Brazil in *Coastal Ocean Observing System*, Elsevier (2015).
5. R.H. Kraichnan. Inertial ranges in two-dimensional turbulence. *Phys. Fluids* **10**, 1417–1423 (1967).
6. J.G. Charney. Geostrophic turbulence. *J. Atmos. Sci.* **28**, 1087–1094 (1971).
7. J.C. McWilliams. Submesoscale, coherent vortices in the ocean. *Rev. Geophys.* **23**, 165–182 (1985).
8. X. Capet, J.C. McWilliams, M.J. Molemaker, A.F. Shchepetkin. Mesoscale to submesoscale transition in the California current system. Part I: flow structure, eddy flux, and observational tests. *J. Phys. Oceanogr.* **38**, 29–43 (2008).
9. P. Klein, B.L. Hua, G. Lapeyre, X. Capet, S. Le Gentil, H. Sasaki. Upper ocean turbulence from high-resolution 3D simulations. *J. Phys. Oceanogr.* **38**, 1748–1763 (2008).
10. G. Boffetta, A. Celani, M. Cencini, G. Lacorata, A. Vulpiani. Non-asymptotic properties of transport and mixing. *Chaos* **10**, 50–60 (2000).

11. L.F. Richardson. Atmospheric diffusion shown on a distance-neighbor graph. *Proceedings of the Royal Society A* **100**, 709–737 (1926).
12. E. Aurell, G. Boffetta, A. Crisanti, G. Paladin, A. Vulpiani. Growth of non-infinitesimal perturbations in turbulence. *Phys. Rev. Lett.* **77**, 1262–1265 (1996).
13. A.L. Sybrandy, P.P. Niiler. WOCE/TOGA SVP Lagrangian drifter construction manual. Scripps Institution of Oceanography Rep. 91/6, 58 pp. (1991).
14. D.V. Hansen, P.M. Poulain. Quality control and interpolations of WOCE-TOGA drifter data. *J. Atmos. Oceanic Technol.* **13**, 900–909 (1996).
15. J.H. LaCasce. Statistics from Lagrangian observations. *Prog. Oceanogr.* **77**, 1–29 (2008).
16. R. Bleck, S. Benjamin. Regional weather prediction with a model combining terrain-following and isentropic coordinates. Part I: model description. *Mon. Wea. Rev.* **121**, 1770–1785 (1993).
17. R. Lumpkin, S. Elipot. Surface drifter pair spreading in the North Atlantic. *J. Geophys. Res.* **115**, C12017, 1–20 (2010).
18. K. Schroeder, J. Chiggiato, A.C. Haza, A. Griffa, T.M. Özgökmen, P. Zanasca, A. Molcard, M. Borghini, P.M. Poulain, R. Gerin, E. Zambianchi, P. Falco, C. Trees. Targeted Lagrangian sampling of submesoscale dispersion at a coastal frontal zone. *Geophys. Res. Lett.* **39**, 11608, (2012).
19. A.C. Poje et al. Submesoscale dispersion in the vicinity of the Deepwater Horizon spill. *Proc. Natl. Acad. Sci. U.S.A.*, 111, 12693–12698 (2014).